Contrôle des performances des antennes par les métamatériaux

Houssam Ayad

UNIVERSITÉ DE GRENOBLE

THÈSE

Pour obtenir le grade de

DOCTEUR DE L'UNIVERSITÉ DE GRENOBLE

Spécialité: **Optique et Radiofréquence**

Arrêté ministériel : 7 août 2006

Présentée par

Houssam AYAD

Thèse dirigée par **Jalal JOMAAH** et
codirigée par **Fabien NDAGIJIMANA**

préparée au sein du **Laboratoire IMEP-LHAC**
dans **l'École Doctorale EEATS**

Antenna Performance Control Using Metamaterials

Thèse soutenue publiquement le **02 juin 2012,**
devant le jury composé de :

Monsieur Gérard GHIBAUDO	Président
Monsieur Ali ALAEDDINE	Rapporteur
Monsieur Moncef KADI	Rapporteur
Monsieur Haidar ELMOKDAD	Examinateur
Monsieur Jalal JOMAAH	Directeur de thèse
Monsieur Fabien NDAGIJIMANA	Co-directeur de thèse

À ma femme…

Remerciements

Les travaux présentés dans ce manuscrit ont été effectués au sein de l'Institut de Recherche IMEP-LHAC, dirigé par Gérard GHIBAUDO. Je lui exprime ma plus profonde reconnaissance pour m'avoir accueilli dans son équipe et d'avoir accepté de présider le jury de soutenance.

Ce travail été effectué sous la direction de M. Jalal JOMAAH et M. Fabien NDAGIJIMANA, professeur à l'Université de Grenoble, auxquels je tiens à exprimer tous mes remerciements pour leur aide, leur expérience et leurs connaissances et je leur exprime ma sincère reconnaissance pour leur disponibilité et pour leurs qualités scientifiques et humaines.

J'exprime ma sincère gratitude à M. Moncef KADI, professeur à l'Université de St Etienne du Rouvray, et à M. Ali ALAEDDINE, professeur à l'Université Libanaise, qui ont accepté d'assurer la tâche de rapporteurs.

Je remercie sincèrement M. Haidar ELMOKDAD, professeur à l'Université Libanaise, d'avoir accepté d'examiner ce rapport. Je le remercie vivement d'avoir assisté à la soutenance de ces travaux.

Je tiens à remercier mes amis, surtout M. Ali KHALIL et M. Ali Awada, pour leur soutien, leur bonne humeur et les nombreuses discussions abordées.

Mes derniers remerciements vont à ma famille, surtout ma femme et mes filles, pour tout ce qu'elles m'ont donné et ce qu'elles me donnent encore.

Table of Contents

TABLE OF CONTENTS **1**

GENERAL INTRODUCTION **5**

CHAPTER 1 BASICS AND OVERVIEWS OF METAMATERIALS **9**

1.1 Introduction 9

1.2 History of Metamaterials 9

1.2.1 Artficial Materials 9

1.2.2 Parallel Plate Media 11

1.3 Chirality and Bi-anisotropic 12

1.3.1 Chiral Media Applications 12

1.3.2 Chiral Media Investigation 13

1.4 Photonic Crystals 14

1.5 Composite Medium 16

1.6 Metamaterials Properties 17

1.7 Research in Metamaterials Domain 18

1.8 New Trends Related to Metamaterials 23

1.8.1 Electromagnetic Cloak 23

1.8.2 Negative Magnetic Permeability at Optical Frequency 24

1.8.3 Electrically Small Antennas 25

1.9 Conclusion 25

1.10 References 27

CHAPTER 2 ELECTROMAGNETIC PROPERTIES IN COMPLEX MEDIA **33**

2.1 Introduction 33

2.2 Maxwell's Equations 34

2.2.1 Operator Equations 35

2.2.2 Medium Equations 37

2.2.3 Bi-anisotropic Materials 38

2.3 Dispersive Models 40

2.3.1 Metallic Structure Epsilon Effective ε_{eff}: The Drude Model 40

2.3.2 Cylinders Array Effective Permeability μ_{eff}: The Lorentz Model 43

2.4 Bi-anisotropic Effect 45

2.4.1 Investigation on the BC-SRR and EC-SRR Inclusions 45

2.4.2 Experiment and Simulation Results 48
2.4.3 Results Interpretation 50
2.5 Homogenization Theory: The Effective Medium Approach 50
2.5.1 Scattering Parameters Retrieving Method 51
2.5.2 Case Studies and Simulation Results 52
2.5.3 ABCD Parameters Retrieving Method 55
2.5.4 Averaging Method 58
2.5.5 Other Retrieval Methods 59
2.6 Metamaterials as Photonic Crystals 60
2.6.1 SRR-Wire Structure 63
2.6.2 BC-SRR Structure 67
2.6.3 Single Wire Structure 69
2.7 Conclusion 72
2.9 References 74
CHAPTER 3 INCLUSION DESIGNS AND APPLICATIONS 77
3.1 Introduction 77
3.2 Sub-wavelength Resonators 77
3.2.1 Split Ring Resonators (SRR) 77
3.2.2 Spiral Resonator (SR) 79
3.2.3 Numerical Investigation 80
3.2.4 Open Complementary SRR (OCSRR) and Open SRR (OSRR) 82
3.2.5 Multi Split Ring Resonator (MSRR) 83
3.3 Electromagnetic Behavior of the Sub-wavelength Resonators 90
3.3.1 SRR Equivalent Circuit: Baena's Analytical Model [3-4] 91
3.3.2 SRR Equivalent Circuit: Saha's and Shamonine's Analytical Approach 94
3.3.3 SRR Magnetic Polarizability 101
3.4 Bianisotropy 102
3.4.1 Role of Bianisotropy 102
3.4.2 Consequences of Bianisotropy 102
3.4.3 MSRR and SR Bianisotropic Behavior Investigation 105
3.5 Low Profile Antenna AMC-Based Surface 107
3.5.1 Artificial Magnetic Conductors (AMCs) 107
3.5.2 Characterization of MSRR-based AMC Surface Reflection 109
3.5.3 Dipole Low Profile Antenna 111
3.6 Conclusion 116
3.7 References 117

CHAPTER 4 METAMATERIAL-LOADED MULTI-BAND PCB ANTENNAS..121

4.1 Introduction 121

4.2 Radiating Elements Characteristics 121

4.3 Metamaterial Loaded Printed Dipoles 122

4.3.1 Dipole Antenna 122

4.3.2 Miniaturization Trade Off 123

4.4 The Trap-Loaded Antenna 124

4.4.1 General Antenna Design Guides 124

4.4.2 Current Distribution 126

4.4.3 Simple Rectangular Dipole Antenna 127

4.4.4 Trap-Loaded Rectangular Dipole Antenna 129

4.4.5 SRR-Loaded Rectangular Dipole Antenna 131

4.4.6 MSRR-Loaded Dipole Antenna 135

4.5 Conclusion 139

4.6 References 140

GENERAL CONCLUSION 143

APPENDICES 147

General Introduction

Just few years ago, a new branch in microwave engineering developed with the emergence of Metamaterials (MTMs). The implementation of the first artificial medium with negative effective dielectric permittivity and magnetic permeability opened the door to the experimental study of a new kind of media: left-handed media (LHM).

The possibility of the artificial implementation of such media allowed the corroboration of many of their electromagnetic properties, predicted years before by Viktor Veselago who examined the propagation of plane waves in a hypothetical substance with simultaneous negative permittivity and permeability. He found that the poynting vector of the plane wave is antiparallel to the direction of the phase velocity, which is contrary to the conventional case of plane wave propagation in natural media.

Since the year 2000, the interest stirred up by these new materials has given rise to numerous works in a wide range of scientific branches. The possibility that Metamaterials offer the production of artificial media with controllable characteristics has permitted the creation of a growing number of completely new applications. Undoubtedly, the most innovative and spectacular application of such artificial media is their use in the implementation of cloaking structures to achieve invisibility, which can be accomplished with the help of engineering of the refraction index of the different layers of the cloaking shield.

On the other hand, it has been shown that a medium constructed by periodic metallic thin wires behaves as a homogeneous material with a corresponding plasma frequency when the lattice constant of the structure and the diameter of the wire are small in comparison with the wavelength of interest. It has been also showed that an array of split ring resonator (SRR) inclusions can result in an effective negative permeability over a particular frequency region. This characteristic has permitted to use such type of inclusion as a resonance creator in several applications, multi-band antenna is an example.

The demand for dual-frequency antennas is increasing in order to deal with the large need for radiating elements for dual-band handheld devices. Due to their dual-band performance, reduced size, and low profile, dual-frequency printed dipoles could be a good solution. The simplest approach to obtain a dual-frequency printed dipole consists of using two different dipoles fed through a single port.

An interesting approach to develop dual-frequency dipole antennas is by loading an antipodal dipole with split ring resonators (SRRs). The loaded dipole resonant frequencies are very close to the self-resonant frequencies of the dipole itself and the SRRs, respectively. This allows developing dual-frequency dipoles with arbitrary frequency ratios.

All titles mentioned above are the core subjects treated in this manuscript. Based on these ideas, new structures are attacked and optimized in order to improve the electrical and dimensional performances. The manuscript is composed of four chapters that present four related issues.

The first chapter constitutes of the basics and overview of Metamaterials. Starting from history of MTMs comprising artificial materials and parallel plate media, and passing by chirality and bi-anisotropic media, then ending by photonic crystals that are designed to manage and manipulate the propagation of light through periodic dielectric or metallic structures. The chapter is ended by citing new trends that are related to MTMs domain; the electromagnetic cloak, negative magnetic permeability at optical frequencies and electrically small antennas are examples of such applications where MTMs are employed.

The electromagnetic performance of waves in complex media is the basic idea of the second chapter in this manuscript. For this issue, Maxwell's equations are first observed. Then using differential forms, these equations could take simpler forms if mathematical formalism higher than the vector algebra is used. On the other hand, general linear medium equations that are also called magnetoelectric or bianisotrpic are cited. The first section of this chapter is finished by showing the fundamentals of bianisotropic materials and homogenization theory.

The second section includes the bianisotrpic effect comprising an EM investigation about the excitation two forms of SRR; the broadside BC-SRR and the edge coupled EC-SRR. Depending on the orientation of the EC-SRR to the external fields, the structure can exhibit either a bianisotropic or non-bianisotropic behavior. This concept is validated by EM simulations; this is followed by an interpretation of the results that compares the functioning of the two SRR forms. A common approach for the extraction of the constitutive parameters of Metamaterial from transmission and reflection characteristics is demonstrated in addition to a case study that completes this section.

Another description of studying Metamaterials is photonic crystals that are characterized by band gap (dispersion) diagram; this is the subject of the last section of the second chapter. Two cases are then studied; BC-SRR and single wire structure.

After introducing a case study of SRR inclusion in chapter two, Multi SRR is presented in chapter three as another sub-wavelength resonator. The electromagnetic behavior of SRR and the equivalent circuit of MSRR are the two points of view constituting the second section of this chapter. Two approaches for calculating the resonant frequency of a SRR are then depicted in addition to numerical applications. Fixed over an artificial magnetic conductor (AMC) constituting of an array of MSRRs, the performance of a dipole low profile antenna is studied. The rectangular arrays are of 49 and 81 inclusions.

The last chapter of this manuscript is about multi-band PCB antennas when they are loaded by MTMs. This chapter starts by an exposure of radiating elements and their characteristics. A physical demonstration of such loaded antenna is presented whereas dipole antenna is given as an application example.

EM simulations of trap-loaded antenna are then shown after explaining its general design and the current distribution across its parts. The simulations initiates by a simple rectangular dipole antenna followed by a trap-loaded one. After evaluating their reflection coefficient and directivity, one can proceed to load the antenna by a SRR first and MSRR as a final load of the antenna.

Chapter 3 Basics and Overviews of Metamaterials

3.1 Introduction

A growing interest in the research results concerning the interaction of electromagnetic waves with complex materials has been observed in the past few years. A reflection of this fact is a new term "*Metamaterials*" that has emerged in the literature and become part of the research language. Metamaterials represent an emerging research area, one that maypose many challenging objectives of interest to scientists and engineers.

Metamaterials are artificially fabricated structures that have new, physically realizableresponse functions that do not occur or may not be readily available in nature. They are not "materials" in the usual sense, but rather artificially prepared arrays of inclusions or inhomogeneities embedded in a host medium.

In this introductory chapter, we will have a look on the history of Metamaterials which has been started since the 19th century. Different researches in this modern domain are also demonstrated in addition to some example of new trends that are technologically related to Metamaterials.

3.2 History of Metamaterials

3.2.1 Artficial Materials

To the best of our knowledge, the first attempt to explore the concept of "*artificial materials*" appears to trace back to the late part of the19th century. Electrical engineers were always interested in designing and controlling the electromagnetic properties of the materials. At the end of the 19th century, the first studies in this domain were reported.

In 1892 Lord Rayleigh examined how the effective properties of the medium are affected by conducting spheres and cylinders, put in a rectangular order [3-1]. This was followed by a paper published by J. Bose in 1898 showing experimentally the rotation of a plane of polarization

of man-made twisted structures (jute fibers) that are well defined today as artificial chiral structures [3-2].

In 1914, Lindman worked on "*artificial*" chiral media by embedding many randomly oriented small wire helices in a host medium [3-3]. Later, many publications were reportedthe rotation of polarization for the linearly polarized wave after propagating through a bi-isotropic medium made up of arbitrarily gathered and oriented small copper helices that are planted in cotton balls [3-4].

In 1940-50s W. Kock went further in these studies when he decided to benefit from the "*artificial media"* as a lightweight beam shaping elements in the lens antenna applications [3-5]. The term "*artificial dielectric"* which is nowadays used in the microwave literature was probably coined by him [3-6], [3-7].

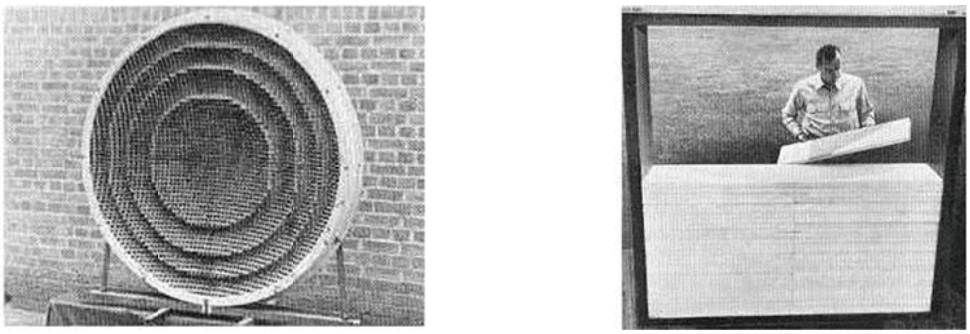

(a) **(b)**

Figure 3-1: Artificial dielectric lenses. (a) Metal-plate lens, (b) assembly of a metallic delay lens [3-8].

In the mid-40s Kock's experiments showed that radiating a group of parallel metallic plates with a low gain radiator leads to a beam pattern similar to that of a homogeneous dielectric lens having refractive index less than unity. The plate spacing was used efficiently to control the refractive index that varies between 0.4 –0.7 as an effective range which made the structure very scattering, but its operational bandwidth was limited. To avoid this limitation many prototypes for artificial dielectric lenses having refractive index greater than unity were presented, including parallel plate lenses three dimensional lattice structures formed of spheres, disks or strips, and lenses implemented by sprinkling conductive paint to form different geometries on polystyrene foam and cellophane sheets Figure 3-2[3-8].

Low density dielectric foam was usually used to hold up the metallic hindrances; which was very beneficial in reducing the weight significantly. The refractive index was variable in a certain

range throughout the lens. In addition, the surface matching was integrated into the design [3-9], [3-10].

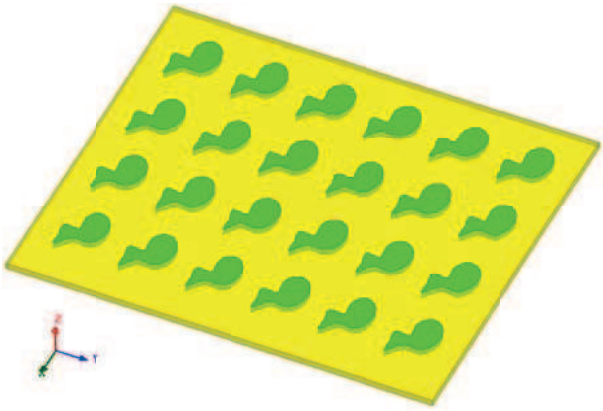

Figure 3-2: Generic sketch of a volumetric Metamaterial synthesized by embedding various inclusions in a host medium.

In 1960 J. Brown reviewed the early development steps in the domain of "*artificial dielectrics"*. The artificial dielectrics were categorized into *"delay dielectrics"* and *"phase advance"* structures compared to the unity index of refraction.During that time the most forthcoming microwave applications were considered to be the large aperture antenna lenses, dispersive prisms, polarization filters and transparent to radio waves random structures. Remarkably it was noted by Brown that the synthesis of the artificial dielectric from conducting elements is a return to the first square of the classical dielectric theory where O. Mossotti developed in 1850 his dielectric model by suggesting that a lattice of conducting spheres can represent a solid dielectric [3-11].

3.2.2 Parallel Plate Media

W. Rotman suggested in 1962 that a rodded or parallel plate media could be used to imitate the electric properties of plasma, as long as the rods spacing less than $0.2\lambda_0$ or plate spacing equivalent to λ_0[3-12]. Wide range of waveguide measurements were carried out to validate the formulas for the electric properties of the rodded media. A significant narrowing of the radiated beam was seen when the radiation from an electric aperture covered by a plasma slab was measured after implementing rodded and parallel plate media. As a consequence of these results, the rodded media form of the artificial dielectrics was used in the leaky wave antennas [3-13] and in the synthesis of surface impedance profiles [3-14] as beam shaping elements.

3.3 Chirality and Bi-anisotropic

A growing interest in a different class of artificial media was seen in the next decades, specifically in chiral and bianisotrpic structures [3-15]-[3-21]. Chirality was first defined by Lord Kelvin in 1904: *"I call any geometrical figure, or group of points, chiral, and say it has chirality, if its image in a plane mirror, ideally realized, cannot be brought to coincide with itself"* [3-22].

On the other hand, the concept of bianisotropic medium was devised by D. Cheng and J. Kong [3-23], [3-24] in 1968 when a certain level of maturity [3-16] have been reached after a suddenly started research boom on electromagnetics of moving media. It is necessary to include cross-coupling terms between the electric and magnetic field excitations and polarization responses when trying to characterize bianisotropic and chiral media by using constitutive relations.

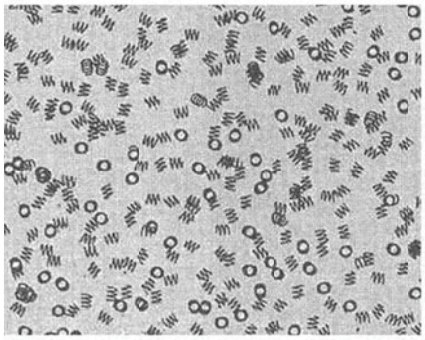

Figure 3-3: Example of Chiral structure

In Chiral media, the anti-symmetry with respect to mirror reflection (Figure 3-3), which is a distinct geometrical character of the internal structure creates macroscopic effects that are witnessed as the rotation of the polarization of the propagating field plane due to the chiral element that result in magneto-electric coupling. This phenomenon has been known since the early 19th century in classical optics as optical activity. Year 1990 witnessed the *"second wave"* of chirality research which was motivated by the potential application in microwave, millimeter wave and infrared frequencies[3-15]-[3-21].The Lindman's experiments with artificial isotropic chiral medium, made from randomly dispersed electrically small helices in a host (see Figure 3-3), were extensively repeated by many research groups leading to several patents granted at that time [3-25].

3.3.1 Chiral Media Applications

The application of the chiral materials was mainly seen in the design of antireflection coatings (radar absorbing materials); at the start of this second wave of research; in order to

reduce the radar cross-section for aerospace vehicles [3-26]. However, advanced studies showed that the introduction of the chiral obstacles results in no enhancements in the reflection characteristics when compared to the patterns obtained from non-chiral inclusions and that the chiral layers are inadequate for antireflection coatings purposes[3-27], [3-28]. It was recognized that the mechanism responsible for the enhanced absorption is the half-wave resonance of the inclusion and not their handed geometric shape [3-29].

The guided-wave structure containing chiral materials is considered as another potential area of application. It is also called chiro-waveguides with the TE and TM modes being coupled together where the coupling coefficient is proportional to the chirality parameter [3-30]. It was hypotheses that the wave guides loaded with chiral medium have a potential application in different areas such as **integrated microwave** and **optical devices** (as directional switches), **optical waveguides** and as **substrates** or **superstrates** in planar antennas in order to decrease the surface-wave power and improve radiation efficiency[3-31]. In addition, it was theoretically presented, that the chirality of the antenna substrate is demonstrated in the rotation of the radiation pattern around the axis that is at right angle to the slab by an angle depending on the chirality parameter, with beam-steering systems or simple radiating devices with complex radiation patterns being a possible area of application [3-32].

3.3.2 Chiral Media Investigation

From 1990s there have been focuses on sculptured thin films for the investigation of chiral materials, which are nanostructured material that are characterized with unidirectional varying properties. Sculptured films can be designed and realized in a manageable manner through using physical vapor deposition [3-33]. During this process, the growth direction of the produced chiral columnar morphology can be managed by varying the direction of the incident vapor flux and rotating the substrate. The chiral sculptured thin films are highly concerned since they respond in different ways to orthogonal circular polarizations. Within a certain wavelength regime, light of the same handedness as the material is strongly reflected, while the other polarization is mainly transmitted. This phenomenon initiated many applications, mainly in linear optics, starting from 1999 [3-34]. The applications include but not limited to: **circular polarization filters**, **polarization discriminators**, **optical fluid sensors** and **chiral photonic band-gap** materials. Optical interconnects and polarization routing are some of the forthcoming applications.

3.4 Photonic Crystals

Interest in *photonic crystals* started to appear in the late 80s as a new class of artificially structured materials, parallel to the chiral structures. In 1987 E. Yablonovitch and S. John published two landmark papers where Yablonovitch demonstrated how to control the spontaneous emission of materials implanted within the photonic crystal using EM bandgap, whereas S. John suggested the usage of "disordered dielectric microstructure" for the localization and control of light. The next years witnessed exponential growth of research on photonic crystals, summarized in the numerous books [3-35], [3-36]-[3-42].

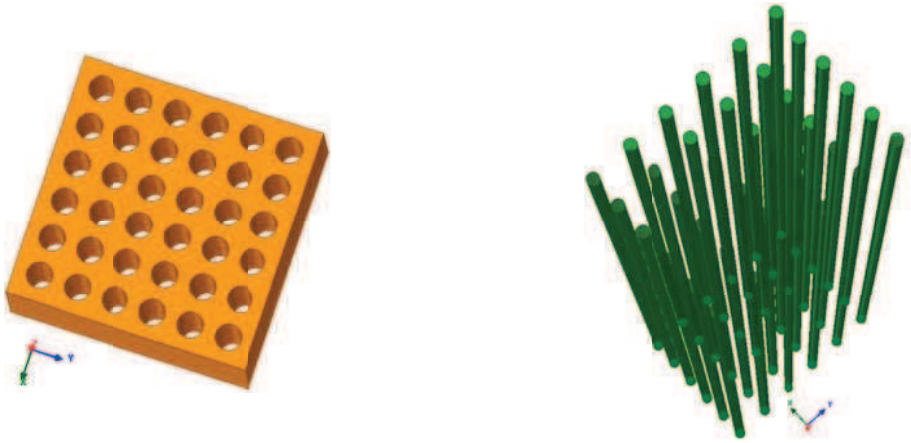

Figure 3-4: Example of photonic crystal structure.

Photonic crystals, example shown in Figure 3-4, are artificially designed to manage and manipulate the propagation of light through periodic dielectric or metallic structures having lattice constant comparable to the wavelength [3-36]. Two ways can be used to make a standard photonic crystal: arranging a lattice of air holes on a transparent background dielectric, and forming a lattice of high refractive index material implanted in a transparent medium with a lower refractive index.

The aim is to design materials that influence the properties of photons as the ordinary semiconductor crystals do on electrons. As the doping of impurities in the semiconductors lead to different applications, the insertion of defects in the usual periodic structure of a photonic crystal possessing complete photonic band-gap.

There are different types of defects, each leads to localized photonic states in the gap: permits bending of light through sharp bends with minor losses (Figure 3-5a), planar defects like a perfect mirror (Figure 3-5b), point defect acts like a micro cavity (Figure 3-5c) and line defect like a waveguide (Figure 3-5d).

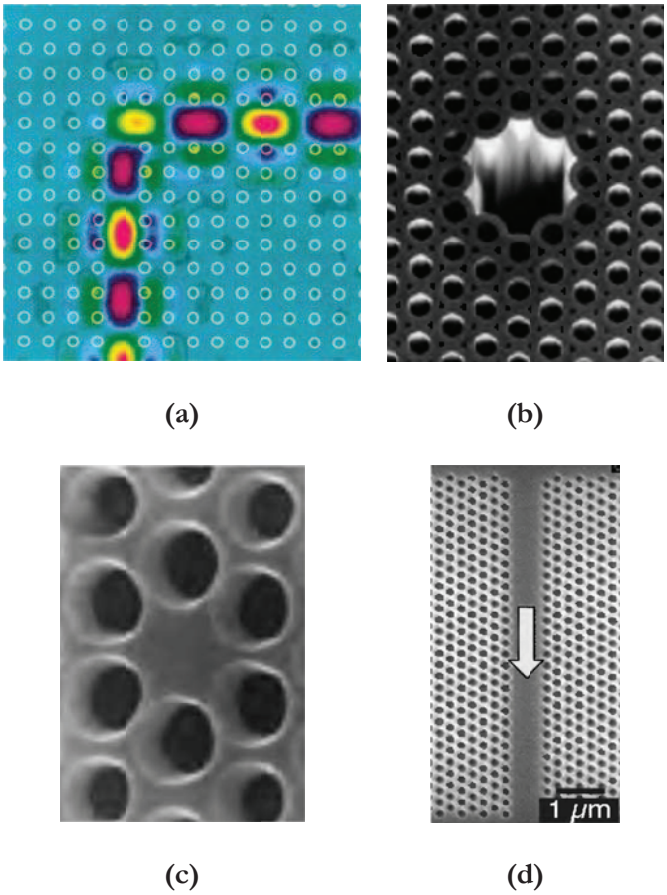

Figure 3-5: (a) Electric field of light propagating down a waveguide with a sharp bend carved out of a square lattice of dielectric rods. The white circles indicate the positions of the rods (reproduced from [3-44]). (b) The central part of a microstructure optical fiber with a hollow core. The confinement of light is achieved through a photonic bandgap reflection at the periodic structure which surrounds the central core (c) Micro cavity formed by a single missing hole. (d) Channel optical waveguide fabricated in a 2D photonic crystal (adapted from [3-35]).

Exploring the physical and optical properties of photonic crystals has opened the door to new ideas for optical devices and systems. The scaling properties of Maxwell equations allowed the analysis of photonic crystals components in the microwave system which facilitates the mode of fabrication and test.

These structures encompassed Y-junctions, directional couplers and Mach-Zehnder interferometers which are essential for almost all applications necessary in optical networks (filters, de-multiplexers, routers, and power combiners/splitters) [3-43].The photonic crystal fibers are the first application of photonic crystals to the world of optical communication Figure 3-5 (b) [3-40].

3.5 Composite Medium

In 1999 J. Pendry et al. suggested that, in a definite frequency range, a microstructure having the form of a split ring resonator (SRR) that is built of non-magnetic conducting sheets could be tuned to negative values of magnetic permeability [3-45]. At that point, the behavior of a photonic structure that is made up of 3D network of thin wires was already studied; it acts like a plasma characterized by a negative electric permittivity below the plasma frequency [3-46].

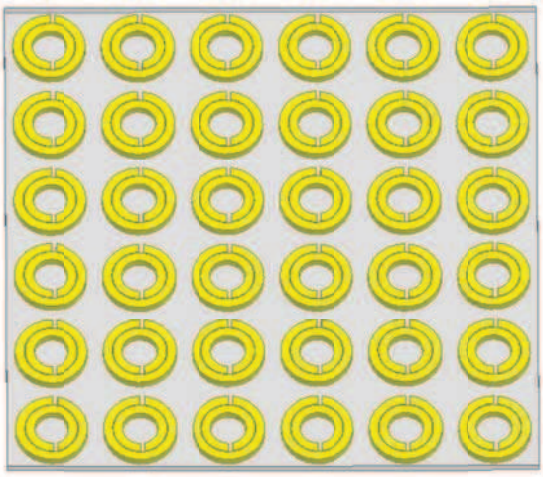

Figure 3-6: Periodic SRR and wire structure

Magnetic permeability and electric permittivity were combined by D. Smith et al. who showed that a composite medium based on periodic array of interspaced SRRs and wires (Figure 3-6) reveals frequency region with negative values of effective permeability and permittivity at the same time [3-47]. In 1968 V. Veselego was already studied wave propagation in media of negative μ and ε and came with remarkable effects in these media, such as negative refraction, reversed Doppler Effect or reversed Cerenkov Effect [3-48]. These structures had to be implemented artificially, since double negative medium does not exist in nature. The negative refraction phenomenon in a lattice of combined SRRs and wires was verified experimentally in 2001 [3-49], and the research on Metamaterials started to develop exponentially (see e.g. textbooks [3-50]-[3-55], journals special issues [3-56]–[3-60] or a new journal focused on Metamaterials [3-61]).

At that time there is no universal definition for Metamaterials (MTMs) [3-51]. In a broad definition, MTMs are artificial structures that exhibit extraordinary properties differ from their constituents and do not occur in nature. This definition is sometimes limited to include only periodic media in which the periodicity is much smaller than the wavelength of the imposed EM wave, so that these structures behave like an "Artificial molecules" or "atoms" that can affect the

EM fields in a prescribed manner. To relax the definition a bit, some researchers allow the periodicity to be in the same order of the signal wavelength, so the photonic crystals can have a place in Metamaterials. Although random structures are also accepted as Metamaterials, yet researches show preference for the periodic structures.

The subject of MTMs overrode that of bi-anisotropy and related topics like chiral and bi-isotropic media, for two reasons: their implementations can be in the form of random mixtures, and it show magnetoelectricity cross coupling effects [3-62]. At this time, periodic MTM lattices and photonic crystals are being developed parallel to each other. The main difference is in the EM properties of their unit cells: ordinary dielectrics or metals are the constituents of the photonic crystals, whereas the functional building blocks of MTMs are engineered to present customized properties. Yet, on the macroscopic level, some interesting effects of periodic MTMs are observed in the properly designed photonic crystals; hence both structures are related to each other.

3.6 Metamaterials Properties

Metamaterials are generally defined as artificial materials of effectively homogenous EM structure that reveals remarkable properties not provided by natural materials. The unit-cell size *"a"* is a characteristic property of an effectively homogeneous periodic structure where $a<<\lambda_m$ (guided wavelength). Having this condition satisfied, the propagated EM reflects only the effective macroscopic constitutive parameters; the effective relative electric permittivity ε_{eff} and magnetic permeability μ_{eff}. Both parameters depend on the nature of the unit cell, and are related to the refractive index *n* by (3-1):

$$\boldsymbol{n} = \sqrt{\pm\boldsymbol{\varepsilon}_{\boldsymbol{eff}}\boldsymbol{\mu}_{\boldsymbol{eff}}} \qquad \textbf{(3-1)}$$

ε_{eff} and μ_{eff} can take any sign, so four possible sign combinations in the pair ($\varepsilon, \mu \in R$) lead to double positive (DPS), single negative (SNG), or double negative (DNG) medium as shown in Figure 3-7. Among the four combinations, the DNG materials form a new class. In 1968, V. Vaselago predicted a number of fundamental phenomena related to DNG media.

- A DNG medium allows the propagation of EM waves with $\vec{E}$, $\vec{H}$ and $\vec{K}$building a left-handed triad ($\vec{E}\times\vec{H}$ antiparallel to $\vec{K}$), compared with a right-handed triad ($\vec{E}\times\vec{H}$ parallel to $\vec{K}$) characterizing conventional (DPS) materials.
- The phase in a DNG medium propagates backward to the source (backward wave) with the phase velocity opposite (antiparallel) to the group velocity.

- In a medium with negative permittivity and permeability, the index of refraction *n* given by (3-1) is negative [3-63].

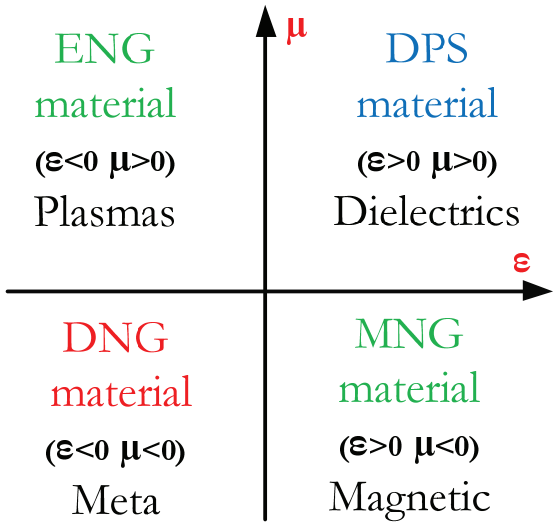

Figure 3-7: Material classification

- A wave incident upon the interface between the DPS and DNG media undergoes negative refraction corresponding to the negative refraction index (a phenomenon called vividly i.e. *"Bending the wave the wrong way"*).
- The constitutive parameters of a DNG medium have to be dispersive with the frequency dependent ε and μ satisfying the conditions:

$$\frac{d(\omega\varepsilon)}{d\omega} > 0, \qquad \frac{d(\omega\mu)}{d\omega} > 0$$

Consequently, ε and μ must be positive in some parts of the spectrum, in order to compensate for their negative values in other frequency regions.

3.7 Research in Metamaterials Domain

Vaselago early work on DNG media concluded that DNG material does not exist in nature, and no further progress in this area occurred for more than 30 years. The step forward happened in 1999 with the effort of J. Pendry et al. [3-45], which became aware of that a split ring resonator (Figure 3-8a) with dimensions much lesser than the free-space wave-length could react to microwave radiation of certain polarization as if it had the effective permeability of the form (3-2):

$$\mu_{eff} = \frac{\frac{\pi r^2}{a^2}}{1 + j\frac{2aR}{\omega r \mu_0} - \frac{3dc_0^2}{\pi\omega^2\left(\ln\left(\frac{2\omega}{d}\right)\right)r^3}} \quad (3\text{-}2)$$

Where R is the resistance of the unit length of the rings, "*w*", "*d*", "*r*", are geometrical parameters of the rings and *"a"* is the lattice constant. In Figure 3-9a, the frequency region of the negative real part of permeability can obviously be recognized for a usual resonant characteristic of $\mu_{eff}(f)$. As the light microstructure which is composed of two concentric metallic split rings replaced ferrites, it becomes possible to attain customized (including negative) permeability values in a narrow frequency band.

Directing the SRR by a time-variable external magnetic field along the x axis excites it, and a strong displacement current is produced due to the presence of the gaps "*g*" on each ring (put on opposite sides of the SRR) that oblige the electric current to flow from one ring to another through the slot "*d*" between. The device acts as a LC circuit powered by an external electromotive force, where C is the distributed capacitance between the rings, and L is the inductance of the rings [3-64].

On the other side, the first report talking about the negative electric permittivity in artificial materials was in 1960s [3-12], but this subject did not gain the interest of the scientific community until late 90s when Pendry et al. published his analysis of low frequency Plasmon's in thin-wire structures [3-46].

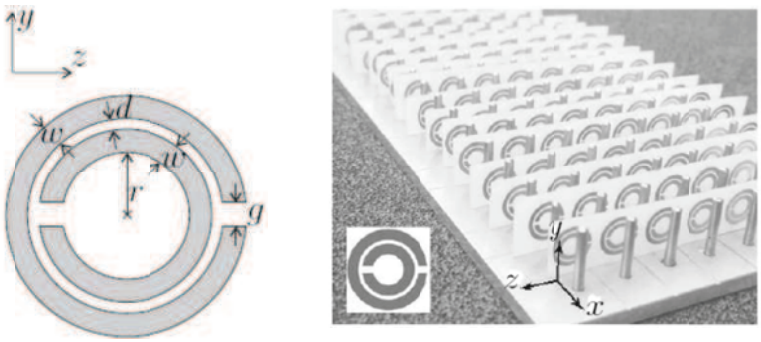

(a) **(b)**

Figure 3-8: (a) Split ring resonator consisted of two split rings. (b) First double negative Metamaterials structure constituted of split ring resonators and thin wires.

The following dielectric function describes the EM response of metals in the visible and near-ultraviolet part of the spectrum [3-65]:

$$\varepsilon_{eff} = \frac{\omega_p^2}{\omega(\omega - j\nu_c)} \qquad \omega_p^2 = \frac{n_e e^2}{\omega_o m_e} \tag{3-3}$$

where the parameter ν_c is a damping term representing dissipation, whereas the angular plasma frequency ω_p depends on the density n_e and mass m_e of the electrons "e". For an artificial material made of very thin metallic wires assembled in a periodic lattice, Pendry succeeded to improve the effective mass of electrons confined to wires by several order of magnitudes, thus shifting the plasma frequency from visible and near-ultraviolet to microwave region. The effective electric permittivity of this structure is expressed by(3-3), where the radial plasma frequency and collision frequency are expressed as [3-65]:

$$\omega_p^2 = \frac{2\pi c_o^2}{a^2 ln(\frac{a}{r})} \qquad \nu_c = \frac{\varepsilon_o a_2 \omega_p^2}{\pi r^2 k} \tag{3-4}$$

i.e. ε_{eff} depends on the geometrical parameters of the system-lattice constant "a" and wire radius "r". These results were verified experimentally in [3-46], [3-66]. Figure 3-9b presents a standard characteristic of $\varepsilon_{eff}(f)$. The first time an artificial structure specialized by double negative material parameters was suggested [3-47] by D. Smith *et al.* who combined the results published by J. Pendry *et al.* concerning negative μ_{eff} from a lattice of SRRs and negative ε_{eff} from a lattice of thin wires. Figure 3-8b shows the experimental structure made of SRRs and metal posts (approximation of wires), providing negative μ_{eff} and ε_{eff}, respectively.

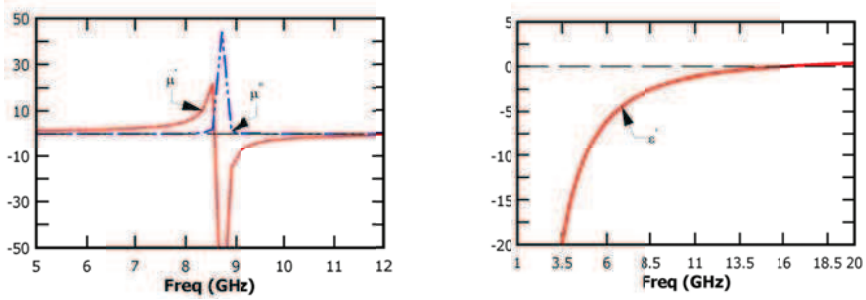

(a) **(b)**

Figure 3-9: (a) Effective magnetic permeability of a SRR. (b) Effective electric permittivity of a lattice of thin wires.

Observing the dispersion diagram of a periodic lattice of SRRs, D. Smith figured out a band gap near the resonant frequency concluding that a region of negative μ_{eff} exists (Figure 3-10a). On the other side, there is a single gap in propagation up to a cutoff frequency ω_p (given that the electric field is polarized along the axis of the wires) in a medium made of periodically sited conducting straight wires. Also, it was noticed that when wires are put between

the split rings, the negative $\varepsilon_{eff}(f)$ combined with the negative $\mu_{eff}(f)$ creating a pass band within the previously banned band, thus allowing the propagation (Figure 3-10b).

This expectation was verified experimentally [3-47] and numerically [3-67], [3-68] by the measurement and simulation of the transmission through a lattice of SRRs only and a lattice of combined SRRs and wires (Figure 3-10c). Moreover, first numerical trials to describe effective constitutive parameters showed that SRR-Wire based MTM structures are characterized by negative electric permittivity and magnetic permeability of [3-69], [3-70].

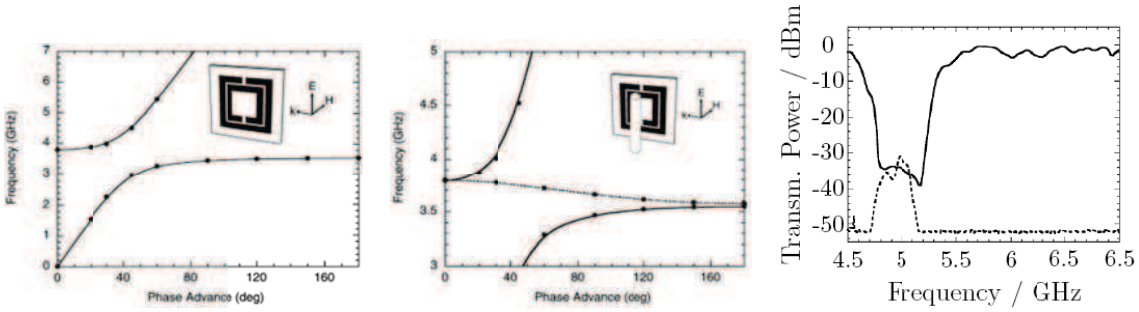

(a) **(b)** **(c)**

Figure 3-10: (a) Dispersion curve for a lattice of SRRs. (b) Expanded view of the dispersion curve. (c) Measured transmission for a lattice of SRRs only (solid line) and for SRRs and wires (dashed line) [3-68].

In 2001 R. Shelby published a paper describing experimental confirmation of a negative index of refraction which is considered a milestone in the research of double negative MTMs. Assembling square copper split ring resonators and copper wire strips printed on a circuit board gives a double negative MTM sample in the frequency region 10.2 to 10.8 GHz (Figure 3-11a).

The deflection of the beam passing through the boards -which are assembled into a two-dimensional periodic wedge-shaped sample-, was measured in order to find the refractive index. The sample and the microwave absorber were irradiated by a microwave beam after they were sited between top and bottom parallel aluminum plates (Figure 3-11b), while the incident face of the wedge was illuminated by a beam with an uniform electric field perpendicular to the metal plates and parallel to the wires. Then the beam faced the second surface of the wedge, the refraction interface, and was refracted into a direction determined by Snell's law after it propagated through the sample. The transmitted power spectrum is measured by a microwave detector as a function of the angle from the normal to the wedge interface.

Experiments were carried on a wedge-shaped DNG sample and a likewise shaped Teflon sample where the microwaves were refracted to positive angles for the Teflon sample but negatively for the MTM sample (Figure 3-11c). At 10.5 GHz, the results of the control sample made of Teflon showed a positive angle of refraction of 27° corresponding to the refractive index of +1.4 which calibrates the apparatus.

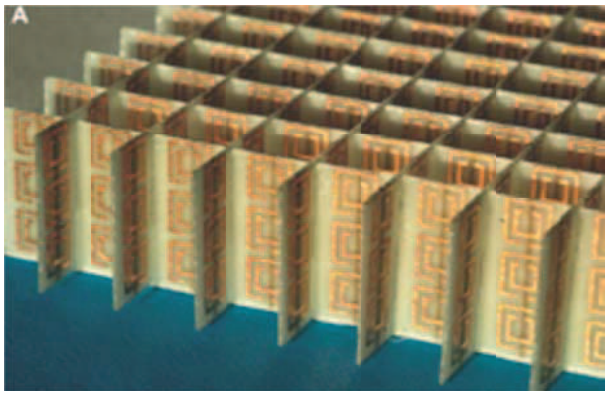

(a)

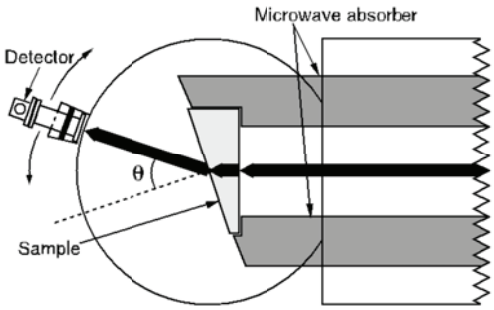

(b)

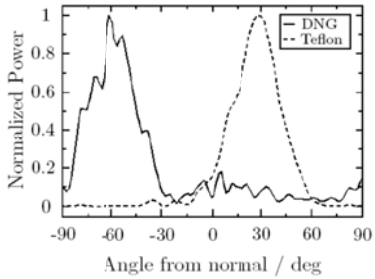

(c)

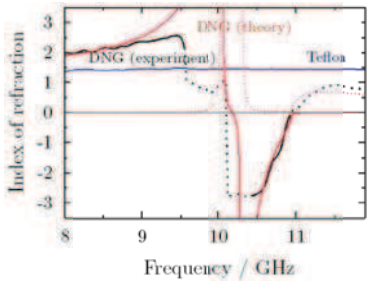

(d)

Figure 3-11: (a) DNG Metamaterial sample. The rings and wires are on opposite sides of the boards. (b) Top view of the experimental setup. (c) Transmitted power at 10.5 GHz as a function of refraction angle for both a Teflon sample and a DNG sample. (d) Index of refraction versus frequency. Adapted from [3-49]

When the SRR-Wire Metamaterial was used the beam exited at an angle of −61° which gave an effectively negative index of refraction −2.7. When the resonance was at 10.5 GHz, the wire and SRR media displayed a bandwidth of 500 MHz in approximate concurrence with the dispersion properties expected by the product of the material parameter expressions of the wire and SRR media (the theoretical and measured index of refraction in function of frequency is presented in Figure 3-11d).

After the revelation of the negative refraction phenomena many features of the experimental results have been doubted. It was argued that the group refraction is positive even

when the phase refraction is negative [3-71] when considering the incidence of a modulated plane wave on an infinite half space of a negative refractive index material. This inconsistency was made clear by explaining that the direction of group velocity is not essentially parallel to the normal of the interference pattern formed (in this case) by two waves of different frequencies [3-72] –[3-75].

Furthermore, the experimental detection of the transmitted wave was done at an intermediate distance to the sample and not in the far field which led the critics to claim that the interpretation of the transmission measurements are highly vague [3-76]. However, the negative refraction phenomenon has been proved in another set of experiments, including the measurement of the EM field profiles at the distance of $28\lambda_0$ [3-77], [3-78] and $85\lambda_0$ [3-79] from the MTM sample. Moreover, the experimental results related to the observed negative refraction [3-80], [3-81] were backed up by numerical simulations of wedge-shaped Metamaterials.

Most of the remarkable phenomena related to DNG media, e.g. reversal of Doppler Effect, reversal of Cerenkov radiation and negative Goos-Haenchen beam shift were investigated on the theoretical basis only. The interest in Metamaterials was refreshed after the confirmation of the concept of the double negative medium through the negative refraction experiment, which started on a fast growing research area.

3.8 New Trends Related to Metamaterials

However, far from the negative refraction, there are many other ideas related to Metamaterials that have attracted the scientists and engineers to this field of studies. Many of these new ideas which created the main trends in the current research on Metamaterials are briefly described in this part.

3.8.1 Electromagnetic Cloak

It has recently been suggested to design the EM structures in such a way to control the paths of EM waves within a material by varying the constitutive parameters spatially in a well prescribed manner [3-82]–[3-84].

Electromagnetic cloak, an invisibility device that guides the waves from any source around an object in order to hide it, is one of the applications of transform media (Figure **3-12**(a)). The cloak prevents the scattering of the waves and does not leave shadow in the transmitted field; in addition applying complex material properties provides the hidden volume and the cloak with the properties of the free space when viewed externally.

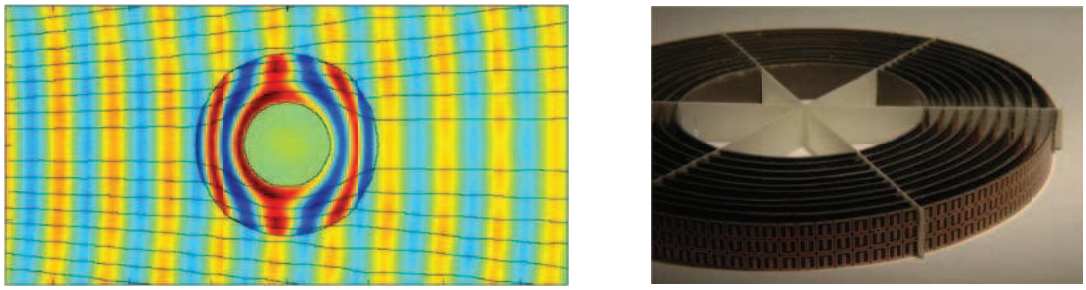

(a) **(b)**

Figure 3-12: Electric field patterns and stream lines indicating the direction of the Poynting vector for the cloak structure. The cloak lies in the region between the black circles and surrounds a copper cylinder at the inner radius. (b)Two dimensional cloaking structures built of ten layers of SRRs. Adapted from [3-84]**.**

The physical realization of the complex material properties became practicable by developing the gradient index lenses of the Metamaterials. Using 10 layers of SRRs, the EM cloak was applied in the microwave range, approximating the optimal magnetic permeability profile with offset values of μ' between 0.1 and 0.3 (see Figure **3-12**(b)). By decreasing the scattering and reducing the shadow of the concealed object, the EM properties of the cloak/object combination becomes similar to the free space, which is experimentally verified.

3.8.2 Negative Magnetic Permeability at Optical Frequency

Starting with Pendry *et al.* [3-45] who proposed the first guidelines to design an artificial magnetic material in the form of SRRs array, and continuing with Smith who applied the recipe at X-band frequencies, it is clear now that the efforts is directed in such a way to produce the negative magnetic permeability at higher frequencies. In the first trials, the dimensions of the SRRs were reduced and their resonance frequency was increased to 1 THz [3-85].

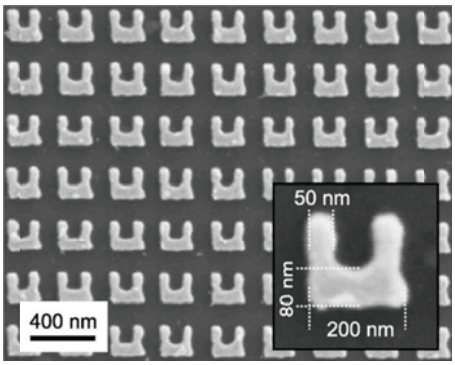

Figure 3-13: Electron micrograph of a split-ring array with a total area of 100 μm2.Adapted from [3-86].

The following modification was to replace the double C-shaped SRRs by single ones whose magnetic response was shown at 85THz (3.5μm) [3-86]. The single C-shaped SRR structures were further optimized to attain magnetic resonance wavelengths at around 900 nm. Currently, succeeding in creating Metamaterials structures with magnetic responses in the visible range, keeps no place for the classical SRR shape, and prevails over Nano-rods, ellipsoidal voids arrays in metal sheets or Nano-fishnet (bi-periodic cross gratings) structures [3-87]–[3-89].

3.8.3 Electrically Small Antennas

Engineered electromagnetic surface textures can be used to alter the properties of metal surfaces to perform a variety of functions. For example, specific textures (see Figure 3-14) can be designed to change the surface impedance for one or both polarizations, to manipulate the propagation of surface waves, or to control the reflection phase.

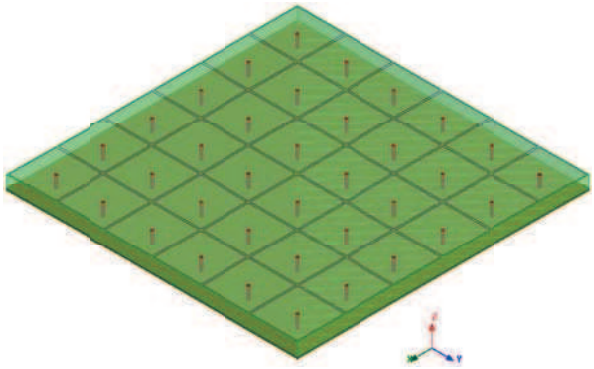

Figure 3-14: Typical Seivenpipper structure

These surfaces provide a way to design new boundary conditions for building electromagnetic structures, such as for varying the radiation patterns of small antennas. Different studies are presented to visualize the performance of small antennas in the world of Metamaterials [3-90].

3.9 Conclusion

The basic history and concepts of Metamaterials studies are paragraphed in this first chapter to ensure a beneficial prefatory to the following chapters of the manuscript. Starting from the primary attempt to discover the concept of artificial materials in the 19th century up to the great evolution in the field of Metamaterials nowadays, a historical view is introduced. The paragraph added at the end of the chapter is to support this view concerning its applications in our daily life.

The concepts of MTMs continue by demonstrating chirality and bi-anisotropic media. The Lindman's experiments with artificial isotropic chiral medium, made from randomly dispersed electrically small helices in a host were extensively repeated by many research groups leading to several patents granted. The growth of research on photonic crystals, as a new class of artificially structure materials in parallel to the chiral structures, is then presented in addition to composite medium based on periodic array of interspaced SRRs and wires.

In the paragraph that discusses research in Metamaterials domain, the remarkable properties of MTMs that are not found in other naturals materials are provided. In other words, MTMs are characterized by double negative DNG (negative permittivity and permeability) property that allows the propagation of EM with $\vec{E}$, $\vec{H}$ and $\vec{K}$ building a left-handed triad. Moreover, the phase in a DNG medium propagates backward to the source with the phase velocity opposite to the group velocity.

3.10 References

[3-1] Lord Rayleigh, "The influence of obstacles arranged in rectangular order upon the properties of a medium". Philosophical Magazine, 34(5):481–502, 1892.

[3-2] J.C. Bose, "On the rotation of plane of polarization of electric waves by a twisted structure".Proceedings of the Royal Society of London, 63:146–152, 1898.

[3-3] F. Yang and Y. Rahmat-Samii, "Reflection phase characterization of an electromagnetic band-gap (EBG) surface," 2002 IEEE Antennas and Propagation Society International Symposium Digest, San Antonio, TX, vol. 3, pp. 744–747, June 16–21, 2002.

[3-4] I.V. Lindell, A.H. Sihvola, and J. Kurkijarvi, "Karl F. Lindman: the last Hertzian, and a harbinger of electromagnetic chirality". IEEE Antennas and Propagation Magazine, 34(3):24–30, Jun 1992.

[3-5] W.E. Kock, "Metal-lens antennas". Proceedings of the I.R.E., 34(11):828–836, Nov 1946.

[3-6] R.E. Collin and F.J. Zucker, editors, "Antenna theory, Part 2", chapter 18: "Lens antennas", by J. Brown, pages 104–150. Inter-University Electronics Series, Vol. 7. McGraw-Hill, New York, 1969.

[3-7] R.E. Collin, "Field theory of guided waves", chapter 12: "Artificial dielectrics", pages 749–786. The IEEE Press Series on Electromagnetic Wave Theory. IEEE Press, New York, 2nd edition, 1991.

[3-8] S.A. Schelkunoff and H.T. Friis, "Antennas, theory and practice", chapter 19: "Lenses", pages 573–591. Applied Mathematics Series.John Wiley and Sons, New York, 1952.

[3-9] J. Brown, "Microwave lenses". Methuen's Monographs on Physical Subjects.John Wiley and Sons, London, 1953.

[3-10] H. Jasik, editor, "Antenna engineering handbook", chapter 14: "Lens-type radiators", by S.B. Cohn, pages 14(1–43). McGraw-Hill, New York, 1961.

[3-11] C.J.F. Bottcher, "Theory of electric polarisation", page 199. Elsevier, Amsterdam, 1952.

[3-12] W. Rotman, "Plasma simulation by artificial dielectrics and parallel-plate media". IEEE Transactions on Antennas and Propagation, 10(1):82–95, Jan 1962.

[3-13] I.J. Bahl and K.C. Gupta, "A leaky-wave antenna using an artificial dielectric medium".IEEE Transactions on Antennas and Propagation, 22(1):119–122, Jan 1974.

[3-14] R.J. King, D.V. Thiel, and K.S. Park, "The synthesis of surface reactance using an artificial dielectric".IEEE Transactions on Antennas and Propagation, 31(3):471– 476, May 1983.

[3-15] A. Lakhtakia and V.K. Varadan, "Time-harmonic electromagnetic fields in chiral media". Springer Verlag, New York, 1989.

[3-16] I.V. Lindell, A.H. Sihvola, S.A. Tretyakov, and A.J. Viitanen, "Electromagnetic waves in chiral and bi-isotropic media". Artech House, 1994.

[3-17] O.N. Singh and A. Lakhtakia, "Electromagnetic fields in unconventional materials and structures". Wiley Series in Microwave and Optical Engineering.JohnWiley and Sons, New York, 2000.

[3-18] N. Engheta, "Special Issue on Wave Interaction with Chiral and Complex Media". Journal of Electromagnetic Waves and Applications, JEWA, 6(5-6):533–793, 1992.

[3-19] A. Priou, "Special Issue on Bianisotropic and Bi-isotropic Media and Applications". Progress In Electromagnetics Research, PIER, 9:1–397, 1994.

[3-20] W.S. Weiglhofer, A.M. Barbosa, and A.L. Topa, "Special Issue on Bianisotropics 2000". AEU International Journal of Electronics and Communications, 55(4):209–291, 2001.

[3-21] S. Zouhdi, A. Sihvola, and M. Arsalane, "Proceedings of 9th International Conference on Electromagnetics of Complex Media (NATO Advanced Workshop on Bianisotropics 2002)", volume 89 of NATO Science Series, II. Mathematics, Physics and Chemistry, Marrakesh, Morocco, 8-11 May 2002. Kluwer Academic Publishers.

[3-22] L.D. Barron, "Molecular light scattering and optical activity", page 25. Cambridge University Press, 2nd edition, 2004.

[3-23] D.K. Cheng and J.A. Kong, "Covariant descriptions of bianisotropic media".Proceedings of the IEEE, 56(3):248–251, Mar 1968.

[3-24] J.A. Kong, "Theory of electromagnetic waves". John Wiley and Sons, New York, 1975.

[3-25] A. Lakhtakia, "Encyclopedia of RF and microwave engineering", pages 610–622. John Wiley and Sons, 2005.

[3-26] V.K. Varadan and V.V. Varadan, "Electromagnetic shielding and absorptive materials".U.S. Patent, No. 4948922, Mar 1990.

[3-27] C.R. Brewitt-Taylor, "Modeling of helix-loaded chiral radar-absorbing layers".Progress In Electromagnetics Research, PIER, 9:289–310, 1994.

[3-28] O. Reynet and O. Acher, "Theoretical and experimental limitations of chiral microwave absorbers". In S. Zouhdi, A. Sihvola, and M. Arsalane, "Advances in electromagnetics of complex media and Metamaterials", volume 89 of NATO Science Series, II. Mathematics, Physics and Chemistry, pages 461–470, Amsterdam, 2002. Kluwer Academic Publishers.

[3-29] J.H. Cloete, M. Bingle, and D.B. Davidson, "The role of chirality and resonance in synthetic microwave absorbers".AEU International Journal of Electronics and Communications, 55(4):233–239, 2001.

[3-30] P. Pelet and N. Engheta, "The theory of chirowaveguides". IEEE Transactions on Antennas and Propagation, 38(1):90–98, Jan 1990.

[3-31] F. Mariotte, P. Pelet, and N. Engheta, "A review of recent study of guided waves in chiral media". Progress In Electromagnetics Research, PIER, 9:311–350, 1994.

[3-32] P. Pelet and N. Engheta, "Theoretical study of radiation properties of a finite-length thin-wire chirostrip antenna using dyadic Green's functions and method of moments". Progress In Electromagnetics Research, PIER, 9:265–288, 1994.

[3-33] A. Lakhtakia and R. Messier, "Introduction to complex mediums for optics and electromagnetics", pages 447–478. SPIE Press, Bellingham, USA, 2003.

[3-34] M.W. McCall. „Introduction to complex mediums for optics and electromagnetics", pages 479–506. SPIE Press, Bellingham, USA, 2003.

[3-35] J.M. Lourtioz, H. Benisty, V. Berger, J.M. Gerard, D. Maystre, and A. Tschelnokov, "Photonic crystals: towards nanoscale photonic devices". Springer, 2005.

[3-36] J.D. Joannopoulos, R.D. Meade, and J.N. Winn, "Photonic crystals: molding the flow of light". Princeton University Press, 1995.

[3-37] K. Sakoda, "Optical properties of photonic crystals". Springer, 2001.

[3-38] S.G. Johnson and J.D. Joannopoulos, "Photonic crystals: the road from theory to practice". Kluwer Academic Publishers, Boston, 2002.

[3-39] K. Busch, S. Lolkes, R.B. Wehrspohn, and H. Foll, "Photonic crystals: advances in design, fabrication, and characterization". Wiley-VCH Verlag, 2004.

[3-40] F. Zolla, G. Renversez, A. Nicolet, B. Kuhlmey, S. Guenneau, and D. Felbacq, "Foundations of photonic crystal fibers". Imperial College Press, 2005.

[3-41] K. Yasumoto, "Electromagnetic theory and applications for photonic crystals". CRC Press, Taylor and Francis Group, 2006.

[3-42] J.D. Joannopoulos, S.G. Johnson, J.N. Winn, and R.D. Meade, "Photonic crystals: molding the flow of light". Princeton University Press, 2nd edition, 2008.

[3-43] A. Martinez, A. Griol, P. Sanchis, and J. Marti, "Encyclopedia of RF and microwave engineering", pages 3823–3838. JohnWiley andSons, 2005.

[3-44] J.D. Joannopoulos, P.R. Villeneuve, and S. Fan, "Photonic crystals: putting a new twist of light". Nature, 386:143–149, 13 Mar 1997.

[3-45] J.B. Pendry, A.J. Holden, D.J. Robbins, and W.J. Stewart, "Magnetism from conductors and enhanced nonlinear phenomena".IEEE Transactions on MicrowaveTheory and Techniques, 47(11):2075–2084, Nov 1999.

[3-46] J.B. Pendry, A.J. Holden, D.J. Robbins, andW.J.Stewart, "Low frequency plasmons in thin-wire structures".Journal of Physics: Condensed Matter, 10:4785–4809, 1998.

[3-47] D.R. Smith, W.J. Padilla, D.C. Vier, S.C. Nemat-Nasser, and S. Schultz, "Composite medium with simultaneously negative permeability and permittivity".PhysicalReview Letters, 84(18):4184–4187, 1 May 2000.

[3-48] V.G. Veselago, "The electrodynamics of substances with simultaneously negative values of permittivity and permeability". Soviet Physics USPEKHI, 10(4):509–514, Jan/Feb 1968.

[3-49] R.A. Shelby, D.R. Smith, and S. Schultz. „Experimental verification of a negative index of refraction". Science, 292:77–79, 6 Apr 2001.

[3-50] S.A. Tretyakov, "Analytical modeling in applied electromagnetics". Artech House, Boston, 2003.

[3-51] G.V. Eleftheriades and K.G. Balmain, "Negative-refraction Metamaterials, fundamental principles and applications". IEEE Press, 2005.

[3-52] C. Caloz and T. Itoh, "Electromagnetic Metamaterials: transmission line theory and microwave applications". John Wiley and Sons, 2006.

[3-53] N. Engheta and R.W. Ziolkowski, "Metamaterials, physics and engineering explorations". IEEE Press, 2006.

[3-54] R. Marques, F. Martin, and M. Sorolla, "Metamaterials with negative parameters, theory, design, and microwave applications". John Wiley and Sons, 2007.

[3-55] A.K. Sarychev and V.M. Shalaev, "Electrodynamics of Metamaterials". World Scientific Publishing, 2007.

[3-56] J. Pendry, "Focus Issue: Negative Refraction and Metamaterials". Optics Express, 11(7):639–760, Apr 2003.

[3-57] R.W. Ziolkowski and N. Engheta, "Metamaterials: Special Issue". IEEE Transactions on Antennas and Propagation, 51(10):2546–2750, Oct 2003.

[3-58] N. Zheludev and V. Shalaev, "Special Issue on Nanostructured Optical Metamaterials: Beyond Photonic Bandgap Effects". Journal of Optics A: Pure and AppliedOptics, 7(2):1–254, Feb 2005.

[3-59] T. Itoh and A.A. Oliner, "Special Issue on Metamaterials". IEEE Transactions on Microwave Theory and Techniques, 53(4):1418–1556, Apr 2005.

[3-60] A. Lakhtakia, "Focus on Negative Refraction". New Journal of Physics, 7, Aug 2005.

[3-61] M. Lapine, "The age of Metamaterials". Metamaterials, 1(1):1, Mar 2007.

[3-62] E. Shamonina and L. Solymar, "Metamaterials: how the subject started". Metamaterials, 1(1):12–18, 2007.

[3-63] M.W. McCall, A. Lakhtakia, and W.S. Weiglhofer, "The negative index of refraction demystified".European Journal of Physics, 23(3):353–359, May 2002.

[3-64] R. Marques, F. Mesa, J. Martel, and F. Medina, "Comparative analysis of edgeand broadside-coupled split ring resonators for Metamaterial design - theory and experiments". IEEE Transactions on Antennas and Propagation, 51(10):2572–2581, Oct 2003.

[3-65] J.B. Pendry, A.J. Holden, W.J. Stewart, and I. Youngs, "Extremely low frequency plasmons in metallic mesostructures".Physical Review Letters, 76(25):4773–4776, 17 Jun 1996.

[3-66] P. Gay-Balmaz, C. Maccio, and O.J.F. Martin, "Microwire arrays with plasmonic response at microwave frequencies". Applied Physics Letters, 81(15):2896–2898, 7 Oct 2002.

[3-67] T. Weiland, R. Schuhmann, R.B. Greegor, C.G. Parazzoli, A.M. Vetter, D.R. Smith, D.C. Vier, and S. Schultz, "Ab initio numerical simulation of left-handed Metamaterials: comparison of calculations and experiments". Journal of Applied Physics, 90(10):5419–5424, 15 Nov 2001.

[3-68] P. Markos and C.M. Soukoulis, "Transmission studies of left-handed materials". Physical Review B, 65:033401(1–4), 7 Dec 2001.

[3-69] D.R. Smith, D.C. Vier, N. Kroll, and S. Schultz, "Direct calculation of permeability and permittivity for a left-handed Metamaterial".Applied Physics Letters, 77(14):2246–2248, 2 Oct 2000.

[3-70] P. Markos and C.M. Soukoulis, "Transmission properties and effective electromagnetic parameters of double negative Metamaterials". Optics Express, 11(7):649–661, 7 Apr 2003.

[3-71] P.M. Valanju, R.M. Walser, and A.P. Valanju, "Wave refraction in negativeindex media: always positive and very inhomogeneous". Physical Review Letters, 88(18):187401(1–4), 6 May 2002.

[3-72] M. Born and E. Wolf, "Principles of optics". Pergamon Press, 1959.

[3-73] D.R. Smith, D. Schurig, and J.B. Pendry, "Negative refraction of modulated electromagnetic waves".Applied Physics Letters, 81(15):2713–2715, 7 Oct 2002.

[3-74] J. Pacheco, T.M. Grzegorczyk, B.-I. Wu, Y. Zhang, and J.A. Kong, "Power propagation in homogeneous isotropic frequency-dispersive left-handed media".Physical Review Letters, 89(25):257401(1–4), 16 Dec 2002.

[3-75] J.B. Pendry and D.R. Smith, "Comment on Wave Refraction in Negative-Index Media: Always Positive and Very Inhomogeneous". Physical Review Letters, 90(2):029703(1), 17 Jan 2003.

[3-76] N. Garcia and M. Nieto-Vesperinas, "Is there an experimental verification of a negative index of refraction yet?".Optics Letters, 27(11):885–887, Jun 2002.

[3-77] C.G. Parazzoli, R.B. Greegor, K. Li, B.E.C. Koltenbah, and M. Tanielian, "Experimental verification and simulation of negative index of refraction using Snell's law".Physical Review Letters, 90(10):107401(1–4), 14 Mar 2003.

[3-78] A.A. Houck, J.B. Brock, and I.L. Chuang, "Experimental observations of left-handed material that obeys Snell's law".Physical Review Letters, 90(13):137401(1–4), 4 Apr 2003.

[3-79] J.S. Derov, B.W. Turchinetz, E.E. Crisman, A.J. Drehman, S.R. Best, and R.M. Wing, "Free space measurements of negative refraction with varying angles of incidence". IEEE Microwave and Wireless Components Letters, 15(9):567–569, Sept 2005.

[3-80] C.D. Moss, T.M. Grzegorczyk, Y. Zhang, and J.A. Kong, "Numerical studies of left handed Metamaterials".Progress In Electromagnetics Research, PIER, 35:315–334, 2002.

[3-81] Z.G. Dong, S.N. Zhu, H. Liu, J. Zhu, and W. Cao, "Numerical simulations of negative-index refraction in wedge-shaped Metamaterials".Physical Review E, 72:016607(1–4), 12 Jul 2005.

[3-82] J.B. Pendry, D. Schurig, and D.R. Smith, "Controlling electromagnetic fields".Science, 312:1780–1782, 23 Jun 2006.

[3-83] U. Leonhardt, "Optical conformal mapping". Science, 312:1777–1780, Jun 2006.

[3-84] D. Schurig, J.J. Mock, B.J. Justice, S.A. Cummer, J.B. Pendry, A.F. Starr, and D.R. Smith, "Metamaterial electromagnetic cloak at microwave frequencies". Science, 314:977–980, 10 Nov 2006.

[3-85] T.J. Yen, W.J. Padilla, N. Fang, D.C. Vier, D.R. Smith, J.B. Pendry, D.N. Basov, and X. Zhang, "Terahertz magnetic response from artificial materials". Science, 303:1494–1496, 5 Mar 2004.

[3-86] S. Linden, C. Enkrich, M. Wegener, J. Zhou, T. Koschny, and C.M. Soukoulis, "Magnetic response of Metamaterials at 100 Terahertz". Science, 306:1351–1353, 19 Nov 2004.

[3-87] S. Linden, C. Enkrich, G. Dolling, M.W. Klein, J. Zhou, T. Koschny, C.M. Soukoulis, S. Burger, F. Schmidt, and M. Wegener, "Photonic Metamaterials: magnetism at optical frequencies". IEEE Journal of Selected Topics in Quantum Electronics, 12(6):1097–1105, Nov/Dec 2006.

[3-88] T.A. Klar, A.V. Kildishev, V.P. Drachev, and V.M. Shalaev, "Negative-index Metamaterials: going optical". IEEE Journal of Selected Topics in Quantum Electronics, 12(6):1106–1115, Nov/Dec 2006.

[3-89] V.M. Shalaev, "Optical negative-index Metamaterials". Nature Photonics, 1:41–48, Jan 2007.

[3-90] S. Clavijo, R. E. Diaz, and W. E. McKinzie III, "Design methodology for Sievenpiper high-impedance surfaces: An artificial magnetic conductor for positive gain electrically small antennas," *IEEE Trans. Antennas Propag.*, vol. 51, no. 10, pp. 2678–2690, Oct. 2003.

Chapter 2 Electromagnetic Properties in Complex Media

2.1 Introduction

The central concept that is discussed across this second chapter of the manuscript is the electromagnetic performance of waves in complex media. Classical Maxwell's equations are first observed before using differential forms of equations that could take simpler forms if mathematical formalism higher than the vector algebra. On the other hand, general linear medium equations that are also called magneto-electric or bi-anisotropic are cited. The first section of this chapter is finished by showing the fundamentals of bi-anisotropic materials and homogenization theory.

The bi-anisotropic effect, comprising an EM investigation about the excitation of two forms of SRR; the broadside BC-SRR and the edge coupled EC-SRR, is the subject of the second section. Depending on the orientation of the EC-SRR to the external fields, the structure can exhibit either a bi-anisotropic or non-bi-anisotropic behavior. The concept is validated by EM simulations; this is followed by an interpretation of the results that compares the functioning of the two SRR forms. A common approach for the extraction of the constitutive parameters of Metamaterials from transmission and reflection characteristics is demonstrated in addition to a case study that completes this section.

The photonic crystals, another description of studying Metamaterials, are characterized by their band gap diagram and studied in the last section of this chapter. As an application example, the dispersion diagram obtained for the broadside-coupled split ring resonator is shown. Moreover, the dispersion diagram of a Wire unit cell is also depicted.

2.2 Maxwell's Equations

The Maxwell equations written in terms of real vector quantities, the electric and magnetic field vectors **E**, **H** and the electric and magnetic flux densities **D**, **B** as functions of the position vector **r** and time t, are:

$$\nabla \times \boldsymbol{E}(\boldsymbol{r},\boldsymbol{t}) = -\frac{\partial \boldsymbol{B}(\boldsymbol{r},\boldsymbol{t})}{\partial \boldsymbol{t}} \tag{2-1}$$

$$\nabla \times \boldsymbol{H}(\boldsymbol{r},\boldsymbol{t}) = \frac{\partial \boldsymbol{D}(\boldsymbol{r},\boldsymbol{t})}{\partial \boldsymbol{t}} + \boldsymbol{J}(\boldsymbol{r},\boldsymbol{t}) \tag{2-2}$$

$$\nabla . \boldsymbol{B}(\boldsymbol{r},\boldsymbol{t}) = \mathbf{0} \tag{2-3}$$

$$\nabla . \boldsymbol{D}(\boldsymbol{r},\boldsymbol{t}) = \varrho(\boldsymbol{r},\boldsymbol{t}) \tag{2-4}$$

Here, the current vector **J** and the charge density ϱ are the postulated sources of electromagnetic fields and they satisfy the continuity condition:

$$\nabla . \boldsymbol{J}(\boldsymbol{r},\boldsymbol{t}) = -\frac{\partial}{\partial \mathbf{t}}\varrho(\boldsymbol{r},\boldsymbol{t}) \tag{2-5}$$

which is implicit in the equations(2-2) and(2-4) and can be obtained by the divergence and $\partial/\partial t$ operations.

The EM force could be calculated without any reference to EM fields, but the introduction of vectors **E**, **B**, which are calculated first, facilitates the problem. The force density is then obtained from the Lorentz expression:

$$\boldsymbol{F}(\boldsymbol{r},\boldsymbol{t}) = \varrho(\boldsymbol{r},\boldsymbol{t})\mathbf{E}(\boldsymbol{r},\boldsymbol{t}) + \mathbf{J}(\boldsymbol{r},\boldsymbol{t}) \times \mathbf{B}(\boldsymbol{r},\boldsymbol{t}) \tag{2-6}$$

The electromagnetic fields **E**, **B** have thus the physical significance in transmitting the force between currents and charges. Because they are not easily calculated from the sources, the problem is alleviated by introducing a second pair of auxiliary field vectors **H**, **D**.

Thus, we arrive at the Maxwell equations (3-1)-(3-4), which are a set of two vector and two scalar equations for four vector or twelve scalar unknowns. This is not enough for a unique solution of the fields. In fact, an additional set of two vector equations should exist between the field vectors **E, B, H,** and **D**. These equations are dependent on the medium and are called the constitutive equations or medium equations. For example, for the most general linear, local and non-dispersive media the additional equations can be written as follows:

$$\boldsymbol{D} = \bar{\bar{\epsilon}}.\boldsymbol{E} + \bar{\bar{\xi}}.\mathbf{H} \tag{2-7}$$

$$\boldsymbol{B} = \bar{\bar{\zeta}}.\boldsymbol{E} + \bar{\bar{\mu}}.\mathbf{H} \tag{2-8}$$

Here, the dyadic parameters $\bar{\bar{\epsilon}}, \bar{\bar{\xi}}, \bar{\bar{\zeta}}, \bar{\bar{\mu}}$ depend on properties of the medium. All physical phenomena within the medium are hidden behind these four dyadics. In fact, the macroscopic electromagnetic fields do not distinguish between two media if they have the same dyadic parameters, even if the physical processes behind those parameters are totally different. The problems considered here are concerned with effects of media on electromagnetic fields rather than the converse case.

2.2.1 Operator Equations

The logic leading to the Maxwell equations can be seen more easily using a mathematical formalism higher than the vector algebra. For example, using differential forms the equations take a very simple form. This notation can be simulated using mixed matrix operators as follows.

Starting from the electromagnetic source defined as current-voltage four-vector i:

$$\boldsymbol{i} = \begin{pmatrix} \boldsymbol{J} \\ \boldsymbol{\rho} \end{pmatrix} \tag{2-9}$$

the equation of charge conservation (2-5) can be written as:

$$\boldsymbol{D_1}.\mathbf{i} = \left(\nabla \frac{\partial}{\partial \mathbf{t}}\right).\begin{pmatrix} \boldsymbol{J} \\ \boldsymbol{\rho} \end{pmatrix} = \nabla.\mathbf{J} + \frac{\partial}{\partial \mathbf{t}}\varrho = \mathbf{0} \tag{2-10}$$

with a four-vector operator D_1 defined by:

$$\boldsymbol{D_1} = \left(\nabla \frac{\partial}{\partial \mathbf{t}}\right) \tag{2-11}$$

The physical fields **E**, **B** satisfy the combination of two Maxwell equations (2-1), (2-3). Writing the vector pair as a single six vector e:

$$\boldsymbol{e} = \begin{pmatrix} \mathbf{E} \\ \mathbf{B} \end{pmatrix} \tag{2-12}$$

and defining a second operator D_2 by:

$$\boldsymbol{D_2} = \begin{pmatrix} \boldsymbol{\nabla \times \bar{\bar{\mathbf{I}}}} & \boldsymbol{\bar{\bar{\mathbf{I}}} \frac{\partial}{\partial t}} \\ \mathbf{0} & \boldsymbol{\nabla} \end{pmatrix} \tag{2-13}$$

we can write:

$$\boldsymbol{D_2 . e} = \begin{pmatrix} \boldsymbol{\nabla \times \bar{\bar{\mathbf{I}}}} & \boldsymbol{\bar{\bar{\mathbf{I}}} \frac{\partial}{\partial t}} \\ \mathbf{0} & \boldsymbol{\nabla} \end{pmatrix} \cdot \begin{pmatrix} \mathbf{E} \\ \mathbf{B} \end{pmatrix} = \begin{pmatrix} \boldsymbol{\nabla \times \mathbf{E} + \frac{\partial \mathbf{B}}{\partial t}} \\ \boldsymbol{\nabla . \mathbf{B}} \end{pmatrix} = \mathbf{0} \tag{2-14}$$

Here, 0 on the right-hand side means a combination of the null vector and the scalar zero. It is easy to check that the following operator product results in the null operator:

$$\boldsymbol{D_1 . K D_2 = 0} \tag{2-15}$$

where we denote:

$$\boldsymbol{K} = \begin{pmatrix} \mathbf{1} & \mathbf{0} \\ \mathbf{0} & \mathbf{-1} \end{pmatrix} \tag{2-16}$$

Comparing equations (2-10) and(2-15) shows us that the former is satisfied identically if the source four-vector i is written in terms of another six-vector h in the form:

$$\boldsymbol{i = K D_2 K . h} \tag{2-17}$$

Writing $h = (H, D)^T$ as a matrix of two vectors, this equation equals:

$$\begin{pmatrix} \boldsymbol{J} \\ \boldsymbol{\varrho} \end{pmatrix} = \begin{pmatrix} \boldsymbol{\nabla \times \bar{\bar{\mathbf{I}}}} & \boldsymbol{-\bar{\bar{\mathbf{I}}} \frac{\partial}{\partial t}} \\ \mathbf{0} & \boldsymbol{\nabla} \end{pmatrix} \cdot \begin{pmatrix} \mathbf{H} \\ \mathbf{D} \end{pmatrix} \tag{2-18}$$

This together with (2-14) defines the Maxwell equations and can, thus, be interpreted as being just a definition of the source in terms of the fields **H**, **D**.

Finally, the medium equation can be written in an operator form:

$$\boldsymbol{e = M(h)} \tag{2-19}$$

where **M** contains the information of the medium. For a linear medium, the **M** operator is a matrix of four dyadics.

2.2.2 Medium Equations

The most general linear medium can be described in terms of four dyadic parameters defined in (2-7), (2-8). These equations can also be written as a relation between the vector pairs $e = (E, B)^T$ and $h = (H, D)^T$:

$$\boldsymbol{H} = \bar{\bar{\boldsymbol{M}}}.\boldsymbol{E} + \bar{\bar{\boldsymbol{Q}}}.\mathbf{B} \tag{2-20}$$

$$\boldsymbol{D} = \bar{\bar{\boldsymbol{P}}}.\boldsymbol{E} + \bar{\bar{\boldsymbol{L}}}.\mathbf{B} \tag{2-21}$$

The relation between the two sets of medium dyadics can easily be derived by substitution:

$$\bar{\bar{\epsilon}} = \bar{\bar{\boldsymbol{P}}} - \bar{\bar{\boldsymbol{L}}}.\bar{\bar{\boldsymbol{Q}}}^{-1}.\bar{\bar{\boldsymbol{M}}}, \bar{\bar{\xi}} = \bar{\bar{\boldsymbol{L}}}.\bar{\bar{\boldsymbol{Q}}}^{-1} \tag{2-22}$$

$$\bar{\bar{\zeta}} = -\bar{\bar{\boldsymbol{Q}}}^{-1}.\bar{\bar{\boldsymbol{M}}}, \bar{\bar{\mu}} = \bar{\bar{\boldsymbol{Q}}}^{-1} \tag{2-23}$$

The general linear medium is also called *magneto-electric* or *bi-anisotropic*. In the case of no special directions in the medium all medium dyadic $\bar{\bar{\epsilon}}, \bar{\bar{\mu}}, \bar{\bar{\xi}}, \bar{\bar{\zeta}}$ are multiples of the unit dyadic $\bar{\bar{I}}$ and the medium is called *bi-isotropic*.

Special cases of the bi-isotropic media are the *isotropic chiral medium* with $\bar{\bar{\zeta}} = -\bar{\bar{\xi}} = \zeta\bar{\bar{I}}$ and the *Tellegen medium* with $\bar{\bar{\zeta}} = \bar{\bar{\xi}} = \zeta\bar{\bar{I}}$.

For $\bar{\bar{\xi}} = 0, \bar{\bar{\zeta}} = 0$, the medium is *anisotropic* and if the dyadic $\bar{\bar{\epsilon}}, \bar{\bar{\mu}}$ are multiples of $\bar{\bar{I}}$, it is simply *isotropic*.

The constitutive equations of the bi-isotropic medium in the frequency domain can be also written in the form:

$$\boldsymbol{D} = \boldsymbol{\epsilon}\mathbf{E} + (\boldsymbol{\chi} - \mathbf{j}\boldsymbol{k})\sqrt{\boldsymbol{\epsilon_0}\mu_0}\boldsymbol{H} \tag{2-24}$$

$$\boldsymbol{B} = (\boldsymbol{\chi} + \mathbf{j}\boldsymbol{k})\sqrt{\boldsymbol{\epsilon_0}\mu_0}\boldsymbol{E} + \mu\boldsymbol{H} \tag{2-25}$$

The dimensionless coefficients χ and k are called the Tellegen and the chirality parameters, respectively, and for a lossless medium they turn out to be real numbers. A chiral medium can be produced by inserting material particles in a suitable base with specific handedness, i.e., particles whose mirror image cannot be brought into coincidence with the original particle, like particles of helical form. The Tellegen medium can be produced by combining permanent electric and

magnetic dipoles in similar parallel pairs and making a mixture with such particles. Such a medium was first suggested by Tellegen in 1948.

When the medium parameters are actually operators containing time differentiation $\partial/\partial t$, the medium is called *dispersive,* or, more exactly, *time dispersive*. If they contain the space differentiation ∇, the medium is called *space dispersive* or *non-local*. If the linear relations do not hold, the medium is, of course, *non-linear*.

Every physical medium can be understood to present time-dispersive properties due to the inevitable inertia of its molecules. In particular, at frequencies high enough every physical medium should act as if un-polarizable, like the vacuum. However, for some frequency ranges medium parameters may depend very little on frequency and they may be considered non-dispersive as a first approximation.

2.2.3 Bi-anisotropic Materials

A material medium consisting of metallic inclusions randomly or periodically distributed inside a host dielectric behaves, at least within a certain range of frequencies (typically in the microwave region), as an effective continuous medium whose electromagnetic constitutive parameters may have values well outside of the range covered by ordinary materials.

Thus, for instance, an artificial negative electric permittivity medium (NEPM) can be obtained by using long metallic wires as inclusions, which simulate the plasma behavior at microwave frequencies. Since free magnetic charges are not present in nature, this method cannot be used for manufacturing negative magnetic permeability media (NMPM). Such media, however, can be built up by using small resonant metallic *particles* with very high magnetic polarizability. Recently, a particle having this property, the so-called *split ring resonator* (SRR), has been proposed for this purpose [2-1].

An artificial medium consisting of an aggregate of these particles shows a negative permeability region near and above the resonance frequency. In this region, magnetic susceptibilities below -1 are possible. A combination of the artificial media proposed in [2-2] has been experimentally demonstrated to be a *left-handed* artificial medium, i.e., a medium having, simultaneously, negative electric permittivity and negative magnetic permeability [2-3].

On the other hand, embedding metallic resonant particles showing cross polarization effects (i.e., an electric polarization as a response to an applied magnetic field and vice versa), in a

host dielectric medium, is the usual technology for obtaining bi-isotropic and/or bi-anisotropic artificial media (i.e., media which replicate optical activity at microwave frequencies).

Indeed, all the aforementioned artificial materials (bi-isotropic, bi-anisotropic, NMPM, and left-handed materials) turn out to be very similar in many aspects. Thus, the presence of resonances in the commonly used bi-anisotropic and bi-isotropic inclusions suggests the existence of regions with negative permeability and/or permittivity, at least if losses are very low or, simply, ignored. Conversely, cross polarization effects could also be expected in some of the proposed resonant particles used to manufacture NMPM and left-handed materials.

The analysis of bi-anisotropic electromagnetic problems is difficult. Anisotropic, bi-isotropic, chiral and non-reciprocal materials are examples of bi-anisotropic media, which generally obey the constitutive relations:

$$\boldsymbol{D} = \bar{\bar{\epsilon}}.\boldsymbol{E} + \bar{\bar{\xi}}.\mathbf{H} \tag{2-26}$$

$$\boldsymbol{B} = \bar{\bar{\zeta}}.\boldsymbol{E} + \bar{\bar{\mu}}.\mathbf{H} \tag{2-27}$$

Here the relations between the electric and magnetic fields (**E** and **H**) and the electric and magnetic flux densities (**D** and **B**) are contained in the permittivity $\epsilon = \epsilon_r\epsilon_0$ and permeability $\mu = \mu_r\mu_0$ and the magneto-electric cross couplings of ζ and ξ. (The free-space parameters are ϵ_0 and μ_0, and the subscript "r" is used to distinguish relative material dyadics.) The dyadic nature of these material quantities emphasizes the anisotropy of the material. A useful distinction in the magneto-electric parameters is the separation of the dyadic ζ and ξ into a reciprocal part *k* and a non-reciprocal part χ [2-4]:

$$\xi = (\chi^T - jk^T)(\mu_0\epsilon_0)^{1/2} \tag{2-28}$$

$$\zeta = (\chi + jk)(\mu_0\epsilon_0)^{1/2} \tag{2-29}$$

where the coefficient j, indicating the time-harmonic notation exp(*jwt*), is there to guarantee real values for the parameters in the case of lossless media. Losses make the parameters complex. The superscript T denotes the transpose operation.

The isotropic chiral material is an important special case [2-5] which is defined through three parameters: all dyadics are (due to isotropy) multiples of the unit dyadic: $\epsilon = \epsilon I$, $\mu = \mu I$, and $k = kI$. Because the medium is reciprocal, its fourth dyadic vanishes: $\chi = 0$.

For the bi-anisotropic case, there are 36 material parameters for one component and, in a mixing rule, all these become coupled. Therefore, it is more helpful to use material matrices in the polarizability analysis.

The six-vector approach has been developed to account for bi-anisotropic effects in electromagnetics problems [2-6]. Six-vectors combine electric and magnetic quantities (that both have three components) into a single vector with six components. The electromagnetic six-vector field **e** and six-vector flux density **d** look like:

$$\mathbf{e} = \begin{pmatrix} \mathbf{E} \\ \mathbf{H} \end{pmatrix}, \mathbf{d} = \begin{pmatrix} \mathbf{D} \\ \mathbf{B} \end{pmatrix} \tag{2-30}$$

and the constitutive relations(2-26)–(2-27) can be written as a single equation:

$$\mathbf{d} = \mathbf{M}.\mathbf{e} \tag{2-31}$$

Where

$$\mathbf{M} = \begin{pmatrix} \boldsymbol{\epsilon} & \boldsymbol{\xi} \\ \boldsymbol{\zeta} & \boldsymbol{\mu} \end{pmatrix} \tag{2-32}$$

is the six-dyadic of the material parameters. It has a 6×6-element matrix representation and the full medium description requires 36 parameters.

2.3 Dispersive Models

From the observation of the frequency characteristics for Metamaterial effective parameters, it can be noticed that extracted curves closely follow Drude or Lorentz behavior with additional artifacts occurring near the resonance frequency. We can apply predefined dispersive models representing the electric permittivity and magnetic permeability of the Metamaterial.

2.3.1 Metallic Structure Epsilon Effective ε_{eff}: The Drude Model

In Metamaterials related research, the Drude characteristic is typically used as an analytical description of the electric properties for a lattice of continuous wires. One of the earliest and most celebrated of these composites occurs in metals and is known as a Plasmon [2-23], [2-24]: a collective oscillation of electron density. In equilibrium the charge on the electron gas is compensated by the background nuclear charge. Displace the gas and a surplus of uncompensated charge is generated at the ends of the specimen, with opposite signs at opposite ends supplying a restoring force resulting in simple harmonic motion,

$$\omega_p^2 = \frac{ne^2}{\varepsilon_0 m_{eff}} \tag{2-33}$$

The plasma frequency, ω_p, is typically in the ultraviolet region of the spectrum: around 15eV in aluminum. The Plasmon's have a profound impact on properties of metals, not least on their interaction with electromagnetic radiation where the Plasmon produces a dielectric function of the form,

$$\varepsilon(\omega) = 1 - \frac{\omega_p^2}{\omega(\omega + i\gamma)} \tag{2-34}$$

The parameter γ is a damping term representing dissipation of the Plasmon's energy into the system. In simple metals γ is small relative to ω_p. For aluminum, γ=0.1e.V, where ε is essentially negative below the plasma frequency, at least down to frequencies comparable to γ.

An artificial material, in which the effective plasma frequency is depressed by up to six orders of magnitude, will be shown. Our material is very thin metallic wires of the order of one micron in radius. These wires are to be assembled into a periodic lattice and Figure 2-1 shows this structure.

The density of electrons in these wires is n, the density of these active electrons in the structure as a whole is given by the fraction of space occupied by the wire.

$$n_{eff} = \mathrm{n}\frac{\pi r^2}{a^2} \tag{2-35}$$

By confining electrons to thin wires we have enhanced their mass by four orders of magnitude so that they are now as heavy as nitrogen atoms. Here is the reduction in the plasma frequency.

These microscopy quantities cancel leaving a formula containing only macroscopic parameters of the system: wire radius and lattice spacing. It is possible to formulate this problem entirely in terms of inductance and capacitance of circuit elements. However in doing so, we miss the analogy with the microscopic Plasmon. Our new reduced frequency plasma oscillation is every bit the quantum phenomenon as is its high frequency brother.

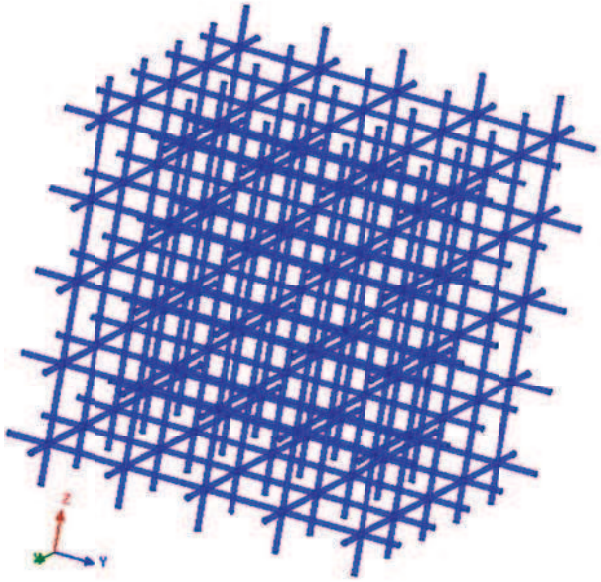

Figure 2-1: Thin metallic wire structure

$$\omega_p^2 = \frac{n_{eff}e^2}{\varepsilon_0 m_{eff}} = \frac{2\pi c_0^2}{a^2 \ln(a/r)} \tag{2-36}$$

$$\varepsilon_{eff} = 1 - \frac{\omega_p^2}{\omega\left(\omega + \frac{i\varepsilon_0 a^2}{\pi r^2 \sigma}\right)} \tag{2-37}$$

In this respect it is important that the structure be made of thin wires. (2-36) shows that the function of the small radius is to suppress the plasma frequency. In a thick wire structure in (2-36), ln (a/r) ≈ 1, so that the plasma frequency corresponds to a free space wavelength of approximately twice the lattice spacing.

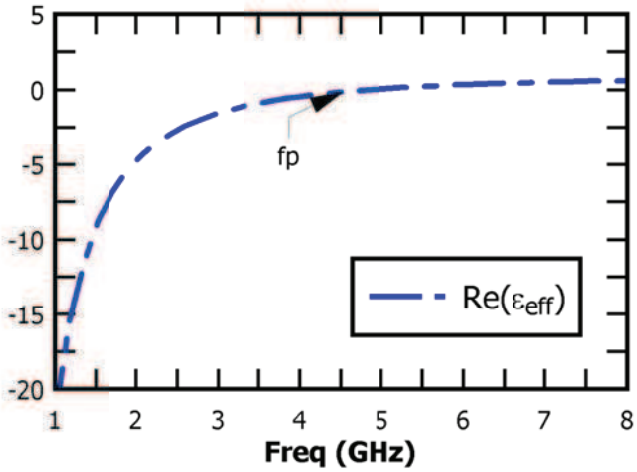

Figure 2-2: Simulation results of Plasmon wire structure using equation

Therefore Bragg diffraction effects would interfere with our simple Plasmon picture. Choosing a small radius ensures that diffraction occurs only at much higher frequencies. As an example, a Mathcad sheet that computes the effective permeability μ_{eff} over a band of frequency is added in appendix A at the end of the thesis.

2.3.2 Cylinders Array Effective Permeability μ_{eff}: The Lorentz Model

A very simple structure for the purposes of illustration is shown in Figure 2-3. Let us apply an external field, which we shall take to be parallel to the cylinders. We assume that the cylinders have a conducting surface so that a current per unit length flows.

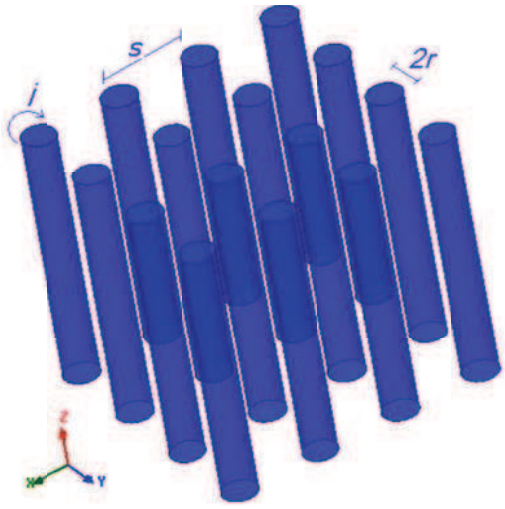

Figure 2-3: Model consists of a square array of metallic cylinders designed to have magnetic properties in the direction parallel to the axes of the cylinders

The field inside the cylinders is:

$$\mathbf{H} = \boldsymbol{H_0} + \boldsymbol{j} - \frac{\boldsymbol{\pi r^2}}{\boldsymbol{a^2}}\boldsymbol{j} \tag{2-38}$$

where the second term on the right-hand side is the field caused directly by the current, and the third term is the result of the depolarizing fields with sources at the remote ends of the cylinders. If the cylinders are very long, the depolarizing field will be uniformly spread over the unit cell, but will have the same number of lines of force in it as the direct field inside the cylinders. We now calculate the total electromotive force (emf) around the circumference of a cylinder as follows:

$$\begin{aligned}\mathbf{emf} &= -\pi r^2 \frac{\partial}{\partial t}\left[H_0 + j - \frac{\pi r^2}{a^2} j\right] - 2\pi r\sigma j \\ &= +i\omega\pi r^2 \mu_0 \left[H_0 + j - \frac{\pi r^2}{a^2} j\right] - 2\pi r\sigma j\end{aligned} \tag{2-39}$$

Where σ is the resistance of the cylinder surface per unit area. We are now in a position to calculate the relevant averages. The average of the field over the entire unit cell is:

$$B_{ave} = \mu_0 H_0 \tag{2-40}$$

$$\mu_{eff} = \frac{B_{ave}}{\mu_0 H_{ave}} = \frac{1 - \frac{\pi r^2}{a^2} + i\frac{2\sigma}{\omega r \mu_0}}{1 + i\frac{2\sigma}{\omega r \mu_0}} = 1 - \frac{\pi r^2}{a^2}\left[1 + i\frac{2\sigma}{\omega r \mu_0}\right]^{-1} \tag{2-41}$$

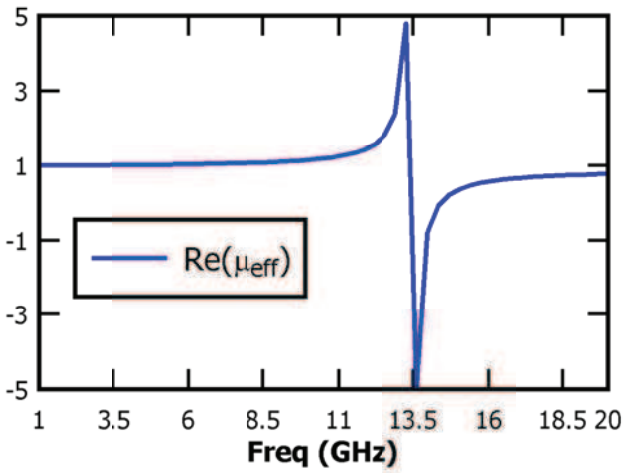

Figure 2-4: real part of the Lorentz effective permeability model

For an infinitely conducting cylinder or in the high frequency limit, is reduced by the ratio of the cylinder volume to the cell volume. This ratio of volumes will turn out to be the key factor in determining the strength of the effect in all our models. Evidently, in the present model, can never be less than zero or greater than unity. It should also be mentioned that to maximize the effect, we could have replaced the metallic cylinders with prisms of square cross section to maximize the volume enclosed within the prism.

As an example we introduce in appendix B a Mathcad sheet that computes the effective permeability μ_{eff} over frequency.

2.4 Bi-anisotropic Effect

The magneto-electric coupling problem can be avoided in 1D, and certain 2D Metamaterial structure. In the 3D isotropic materials geometries, with arbitrary polarization and direction of the electromagnetic incident wave, the lack of the effect can be guaranteed by inversion symmetry of the design [2-9]. The rule of thumb is stated as follow: "to avoid the electric field coupling to the magnetic resonance of the circular current in a split ring resonator, mirror symmetry of the SRR plane with respect to the electric field should be provided".

The extraction methods of the effective material parameters neglect the magneto-electric couplings effect. This approach simplifies the analysis, but on the other hand it may lead to ambiguous constitutive parameters. For this purpose, bi-anisotropic effect should be tested for such Metamaterials. Metamaterial electromagnetic coupling existence is based on the symmetries of the underlying resonant particles found in [2-7]. A systematic analysis of the symmetries for both constitutive elements and lattices was investigated recently in [2-8].

2.4.1 Investigation on the BC-SRR and EC-SRR Inclusions

We will consider in the investigation example, two topologies one is based on the broadside- coupled and the other on the edge-coupled split ring resonators (BC-SRR, EC-SRR) respectively. Figure 2-5 shows the two topologies under consideration.

(a) **(b)**

Figure 2-5: Topologies of (a) edge-coupled (EC_SRR) and (b) broadside-coupled split ring resonators (BC_SRR)

Four different cases exist for the propagation of the quasi TEM wave in the 2D Metamaterial. The cases are shown in Figure 2-6.

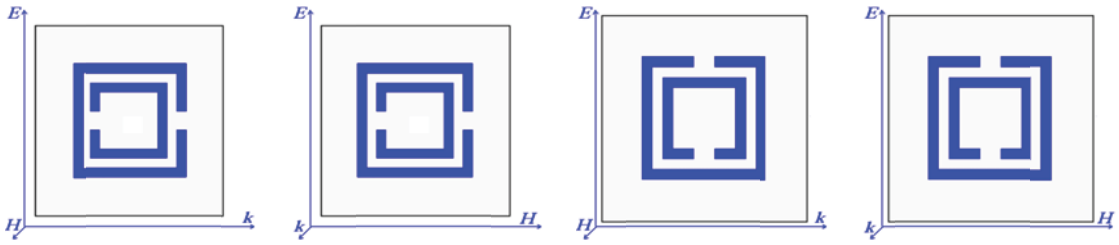

(a) (b) (c) (d)

Figure 2-6: Four different cases exist for the EC-SRR.

Regarding the figure above, it is clear that the E field component in the EC-SRR structure is parallel to the gap for case (a) and (b) and perpendicular to it in case (c) and (d), the study is based on [2-10].

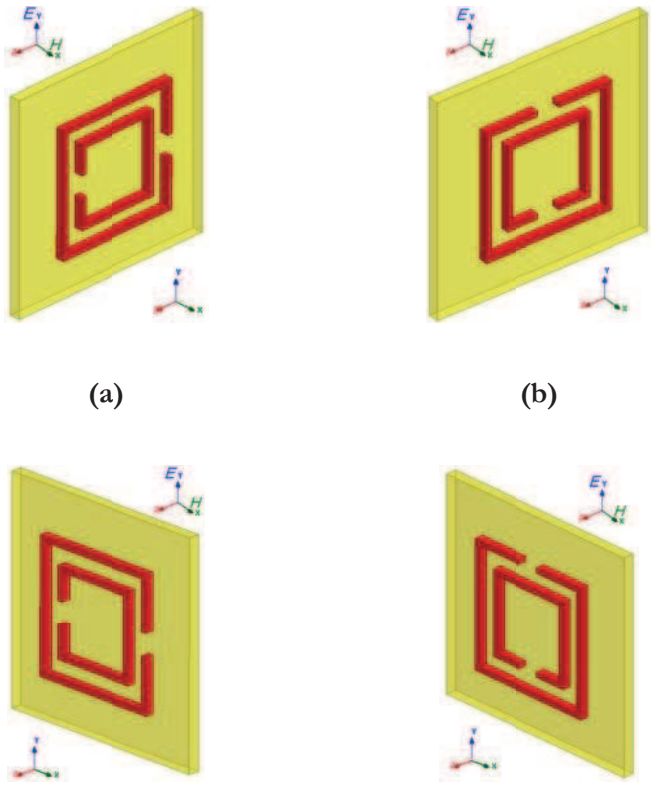

(a) (b)

(c) (d)

Figure 2-7: Different orientations (a)-(d) of the EC-SRR inside a parallel plate waveguide for magnetic (H_X) or electric (E_Y) excitation of inclusion resonances. The waveguide dimensions are: separation plates (y) 1 cm, width (x) 2.28 cm, length (z) 1 cm

- Case (a): E_Y, H_Z, K_X: electric and magnetic excitation.

An asymmetry exists in the EC-SRR structure with respect to the electric field direction Y, that indicating the presence of the magneto-electric coupling. The perpendicular magnetic field H or the electric field E parallel to the gap causes a circulating current in the rings.

- Case (b): E_Y, H_X, K_Z: electric excitation.

An asymmetry exists in the EC-SRR structure with respect to the electric field direction Y, that indicating the presence of the cross coupling effect. The parallel magnetic field H will not couple with the structure while the electric field E that is parallel to the gap causes the circulating current in the rings.

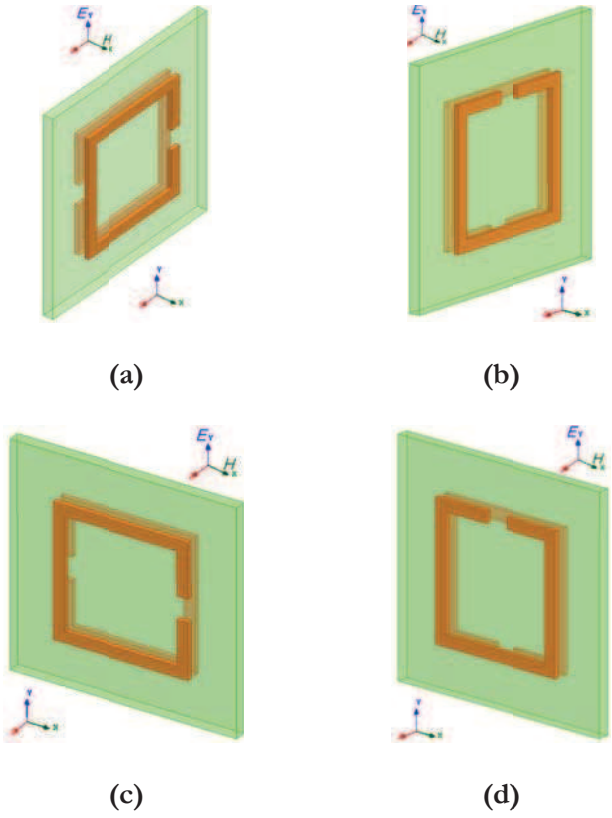

Figure 2-8: Different orientations (a)-(d) of the BC-SRR inside a parallel plate waveguide for magnetic (H_X) or electric (E_Y) excitation of inclusion resonances. The waveguide dimensions are: separation plates (y) 1 cm, width (x) 2.28 cm, length (z) 1 cm

- Case (c): E_X, H_Z, and K_Y: magnetic excitation.

Symmetry exists in the EC-SRR structure with respect to the electric field direction, indicating that the structure will do not have a magneto-electric coupling. The perpendicular magnetic field H causes a circulating current in the rings while the electric field E has no effect on the structure.

- Case (d): E_X, H_Y, and K_Z: no excitation.

Symmetry exists in the EC-SRR structure with respect to the electric field direction X, indicating that the structure will do not have a magneto-electric coupling. The parallel magnetic field H and the electric field E have no effect on the structure.

2.4.2 Experiment and Simulation Results

The theoretical analyses show that depending on the orientation of the EC-SRR to the external EM fields, the structure can exhibit either a bi-anisotropic or non-bi-anisotropic behavior.

On the other hand, the BC-SRR structure exhibits a non-bi-anisotropic effect due to the symmetry of the structure. This is an important result and will lead to a conclusion that the symmetrical structure has a lack of magneto-electric coupling.

Bi-anisotropy can also be detected experimentally from the measurement of the transmission coefficient of a square waveguide loaded by a SRR [2-8]. The experiments conducted on Metamaterial loaded waveguide allow one to identify the response type of the Metamaterial under test [2-11].

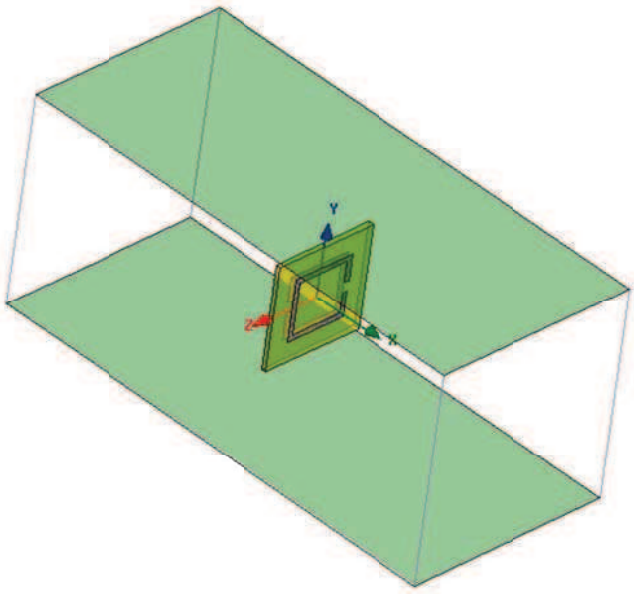

Figure 2-9: BC-SRR inside a parallel plate waveguide

The structure is excited by electric or magnetic field, for multiple orientations of it inside the parallel plate waveguide, to determine the SRR resonance type. The parallel plate waveguide used in the FEM simulator HFSS from Ansoft is shown in Figure 2-9.

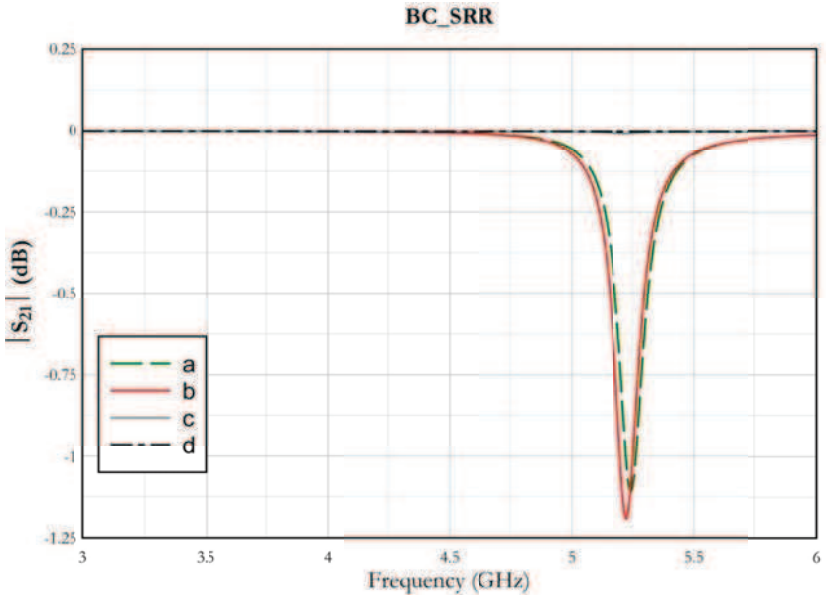

Figure 2-10: Transmission coefficient for different orientation of the BC-SRR structure in a parallel wave guide shown in Figure 2-7

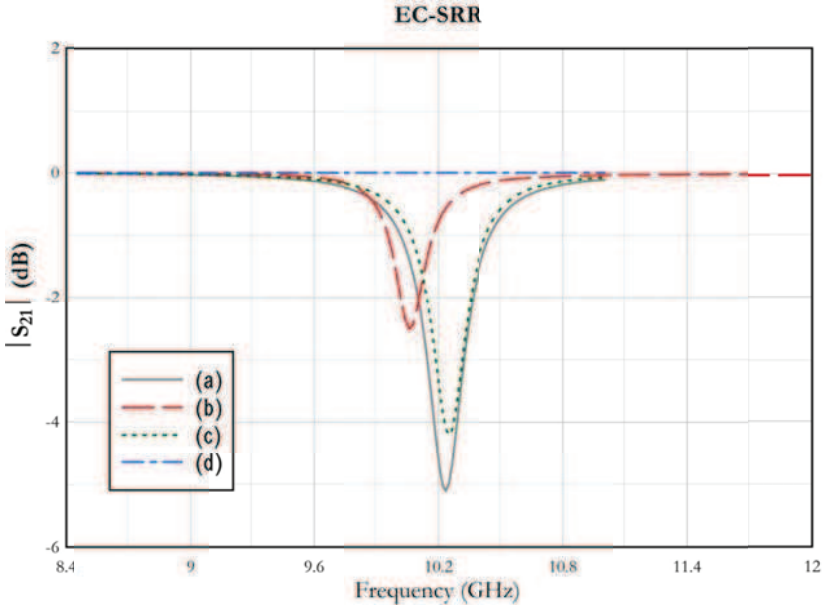

Figure 2-11: Transmission coefficient for different orientation of the EC-SRR structure in a parallel plate waveguide shown in Figure 2-8

The TEM mode used in the parallel plate waveguide is based on the E_Y and H_X field components. Thus in the orientations (a) and (b) of Figure 2-7, the SRR is excited by both fields E and H, while in the orientations (c) and (d), the magnetic field H_X is parallel to the structure and it is only excited by the electric field E_Y.

The simulated transmission coefficients for the different configurations of the SRR loading the waveguide are shown in Figure 2-10 and Figure 2-11 respectively where we assume the direction of propagation is in the z- direction. The waveguide used for the simulation has the X-band dimension i.e. (WR90) rectangular waveguide. PEC boundary is used on the top and bottom instead of the parallel plate. PMC boundary is used on the sides of the structure.

2.4.3 Results Interpretation

It can be shown from Figure 2-10 that the BC-SRR is excited in positions (a) and (b) of Figure 2-7 while it is not excited in position (c) and (d). Moreover, the simulation results of the transmission coefficient for the orientation (a) and (b) in Figure 2-7 are the same, which means that the electric field E_Y does not excite the structure. It can be concluded, that the BC-SRR resonance is of magnetic type.

The behavior of the EC-SRR is not the same and it is more complicated. From the results of Figure 2-11 corresponding to orientation (d) in Figure 2-8, it can be concluded that the EC-SRR does not respond to electric field polarized along the continuous branches of the rings E_X. Stronger dip occurs at orientation (a), where both electric and magnetic field present.

Weaker response occurs at orientation (b) and (c) that corresponds to separate electric and magnetic field excitation. This result leads to the conclusion that the EC-SRR structure is of magneto-electric behavior. The simulation result obtained is in good agreement with the theoretical one. These two approaches are valuable tools for the identification of the bi-anisotropic effect.

2.5 Homogenization Theory: The Effective Medium Approach

Before discussing the effective medium approach, a linear medium requires the foundation of 36 frequency dependent, complex constitutive parameters. The goal is to assign electromagnetic parameters to a composite or a mixture of more than one material. This is called the traditional analytic homogenization theory.

To our knowledge, all known analytical methods are valid for certain limitations and for particular geometries or structures. The analytical homogenization techniques are unreliable or at least not applicable for Metamaterials comprising resonant elements and characterized by a non-negligible lattice constant “a”. One way is to evaluate the numerical solution of the Maxwell’s equations assuming that the fields are local.

The Metamaterial homogenization method, extraction of effective material parameters, based on the retrieval S-parameters techniques requires certain knowledge of the electromagnetic behavior of the system, for instance, the magneto-electric coupling effects. The non-physical result obtained from this method can be explained or rejected in certain circumstance if one already has a deep understand of the bi-anisotropic effect.

2.5.1 Scattering Parameters Retrieving Method

One of the most popular approaches for the extraction of the constitutive parameters of Metamaterial is retrieval from transmission and reflection characteristics. This method is commonly used in laboratories as an experimental way to find the effective parameters of a material sample under test [2-12]. The scattering parameters are calculated or measured for a finite thickness of a Metamaterial, as an example a one unit cell, and related to analytical formulas for reflection and transmission coefficients of a homogeneous slab with the same thickness a [2-13], [2-14] and [2-15]:

$$\begin{aligned} \boldsymbol{S_{11}} &= \frac{\boldsymbol{(1-T^2)R}}{\boldsymbol{1-R^2T^2}} \\ \boldsymbol{S_{21}} &= \frac{\boldsymbol{(1-R^2)T}}{\boldsymbol{1-R^2T^2}} \end{aligned} \tag{2-42}$$

Here R is the reflection coefficient of a wave incident on the interface between a Metamaterial and a free space, and T is the transmission coefficient through the Metamaterial slab:

$$\begin{aligned} \boldsymbol{R} &= \frac{\boldsymbol{Z-Z_0}}{\boldsymbol{Z+Z_0}} \\ \boldsymbol{T} &= \boldsymbol{e^{-jk_0na}} \end{aligned} \tag{2-43}$$

Here Z_0, k_0 are wave impedance and wave number in free space, respectively. The normalized wave impedance $z = {}^{Z}/_{Z_0}$ and the refractive index n of the homogeneous slab can be expressed in terms of the scattering parameters as:

$$\boldsymbol{z = \pm\sqrt{\frac{(1+S_{11})^2 - S_{21}^2}{(1-S_{11})^2 - S_{21}^2}}} \tag{2-44}$$

$$\boldsymbol{n = -\frac{1}{ak_0}\{((Imag(lnT) + 2m\pi) - jRe(lnT))\}} \tag{2-45}$$

Here *m* is an integer and it is related to the branch index of *n'* and the transmission term in function of scattering parameters.

$$T = \frac{1 - S_{11}^2 - S_{21}^2}{2S_{21}} \pm j\sqrt{1 - \left(\frac{1 - S_{11}^2 + S_{21}^2}{2\,S_{21}}\right)^2} \tag{2-46}$$

The signs in (2-44) and (2-45) are determined by the requirements, and keep in mind that the material under consideration is a passive medium:

$$\begin{aligned} Re(z) &\geq 0 \\ n'' &\geq 0 \end{aligned} \tag{2-47}$$

The relative electric permittivity and magnetic permeability characterizing the effective properties of the medium and equivalent to obtained refractive index *n* and normalized impedance z are directly calculated as:

$$\begin{aligned} \varepsilon_{eff} &= \frac{n}{z} \\ \mu_{eff} &= nz \end{aligned} \tag{2-48}$$

The retrieval from scattering parameters is a straight forward method that allows the characterization of Metamaterial with sufficient accuracy. But, this procedure delivers a variety of artifacts in the retrieval parameters, related to the inherent homogeneity of the Metamaterial unit cell. An example of these anomalies is the resonance-anti-resonance coupling or the discrepancy between *n* and z about the positions of the resonance [2-16]. The retrieval process may fail in some cases when reflection or transmission coefficients are very small in magnitude [2-17]. Some improvements based on the determination of effective boundaries, forced continuity of the dispersive effective refractive index, and the elimination of the measurements or simulation noise influence on effective impedance have been proposed [2-18].

2.5.2 Case Studies and Simulation Results

We consider the BC-SRR, the Single-wire and the EC_SRR-Wire as a Metamaterial sample in order to extract its constitutive parameter by the S-parameters retrieval method. The unit cell for each sample is shown in Figure 2-12.

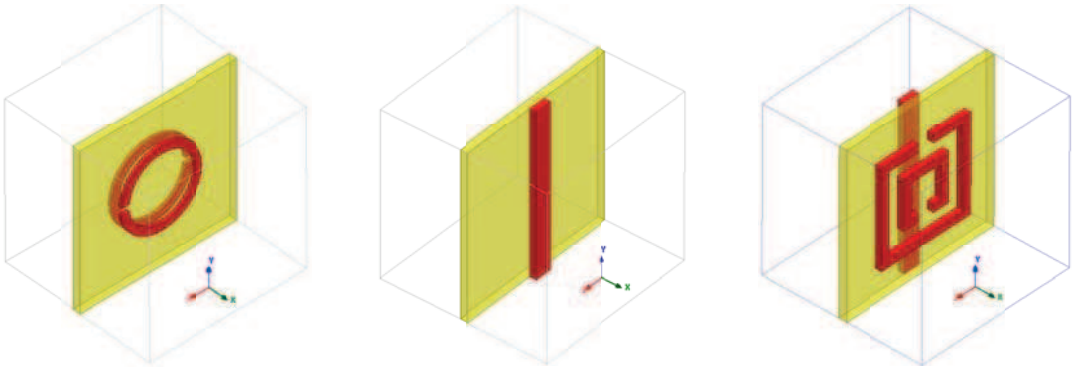

(a) (b) (c)

Figure 2-12: (a) Circular BC-SRR (lattice constant 10mm; substrate thickness h= 0.49 mm, ε'= 2.43, SRR: gap=0.4 mm, outer SRR radius =2.6 mm, strip width w = 0.5 mm). (b) Wire unit cell (lattice constant 5 mm; substrate thickness h= 0.25 mm, ε'=3.48, tan δ = 0.018, strip width w = 0.5 mm). (c) SRR-Wire (SRR at the front side, wire at the back side of the substrate) cell (lattice constant 5 mm; substrate thickness h= 0.25 mm, ε'=3.48, tan δ = 0.018, outer SRR length = 3 mm, inner SRR length =1.5 mm, ring spacing 0.5mm, SRR strip width w = 0.5 mm). All strips are modeled as finite conductor (copper type). All dimensions are parameterized

The structure is excited by the fundamental mode of a waveguide port located at ±z limits of the volume; it will look like a TEM wave with E_Y and H_X field components, propagating in the negative z direction. Perfect Electric Conductor PEC is used at the ±y boundary faces to act as periodic boundary condition. Also, Perfect Magnetic Conductor PMC is used at the ±x boundary faces. The FEM simulation engine used is from Ansoft HFSS and a different meshing is defined many times to ensure reliable results.

A Matlab code, as shown in Figure 2-13, for the retrieval procedure is written and the constitutive parameters are extracted one by one.

```
clear

clf

c=3e8;

t=xlsread(SRR_Wire.xls');

f=t(:,1);

%f=S11_mag(:,1)*1e9;%frequency
```

```
k_0=2*pi*f/c;

d=5e-3;%thickness of the one cell



S11=t(:,2).*exp(-i.*t(:,3)*pi/180);%the extracted phases from HFSS not
multiplied by -1

S21=t(:,4).*exp(-i.*t(:,5)*pi/180);



z=sqrt( ( (1+S11).^2 - S21.^2 )./( (1-S11).^2 - S21.^2) );

eink0d=S21./(1-S11.*((z-1)./(z+1)));
```

Figure 2-13: Matlab code for the extraction of the constitutive parameter from the measured and simulated S-parameters

2.5.2.1 BC_SRR Simulation Results

From our knowledge, we know that the BC-SRR structure, shown in Figure 2-12(a), responds only to the magnetic field and it is of the single negative type. Looking to the extracted permittivity ε' in Figure 2-14 , one can show the appearance of electric response near the SRR resonance. The anti-resonance from ε' and the negative value of ε" in the single negative frequency range are numerical artifacts typical for the S-retrieval method.

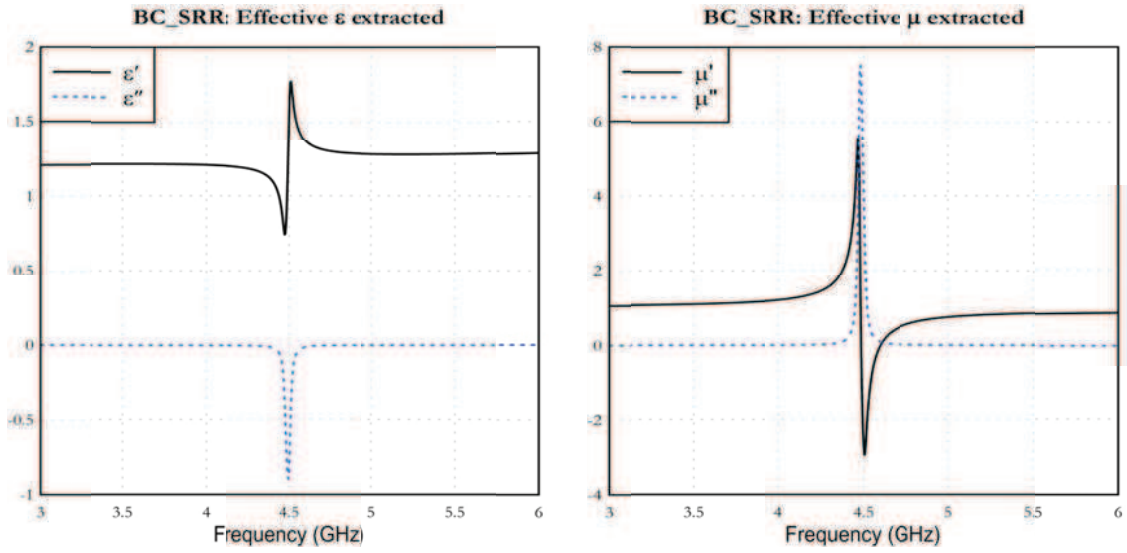

Figure 2-14: S-retrieved effective parameters for the BC-SRR with rings. The extracted electric permittivity shows non-physical behavior in the single negative range.

2.5.2.2 Single Wire Simulation Results

Also shown in Figure 2-15, the physical behavior of extracted effective permittivity or permeability by S-retrieval method for the single wire structure shown in Figure 2-12(b), and it was criticized in several papers, where it was conclude that such parameters cannot form the effective description of a homogenized material.

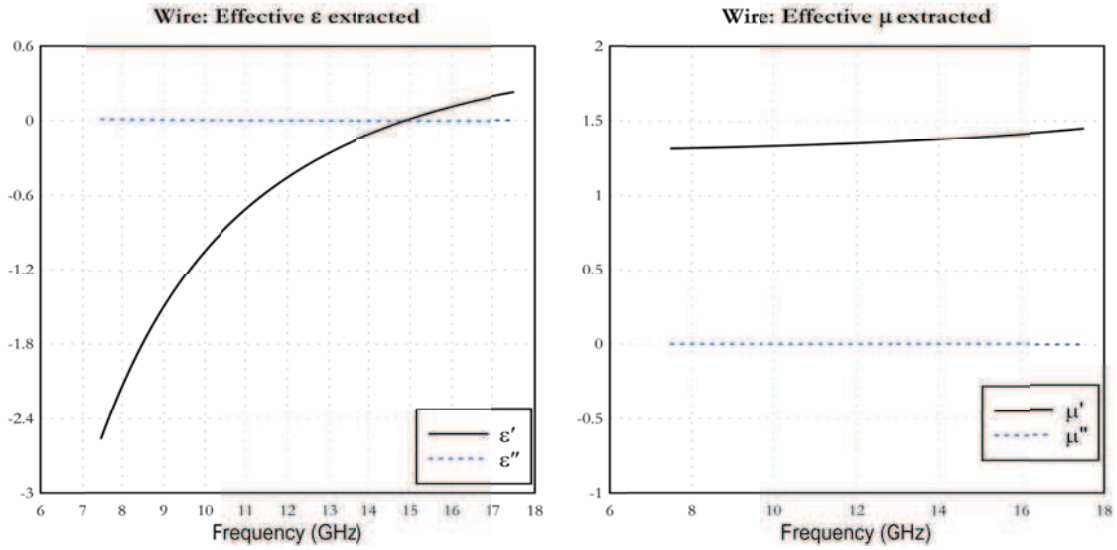

Figure 2-15: S-retrieved effective parameters for a single wire unit cell. Both extracted parameters show physical behavior

2.5.2.3 EC_SRR-Wire Simulation Results

On the other hand, in Figure 2-16, the effective parameters retrieved for a unit cell of a EC_SRR-Wire (see Figure 2-12(c)) lattice is shown. The same artifacts occur in the extracted parameters for double negative structures. In this case the excitation electric field E_Y is parallel and the magnetic field H_X is perpendicular to the strip. The extracted ε_{eff} indicates a non-physical response near the SRR resonance frequency.

2.5.3 ABCD Parameters Retrieving Method

In principle, the effective parameters of MSRR have to be calculated to characterize them as artificial magnetic or dielectric materials. They are conventionally retrieved from S-parameters of one unit cell thick sample under plane wave excitation [2-19]. However, the resulting effective parameters are only assigned to this one sample.

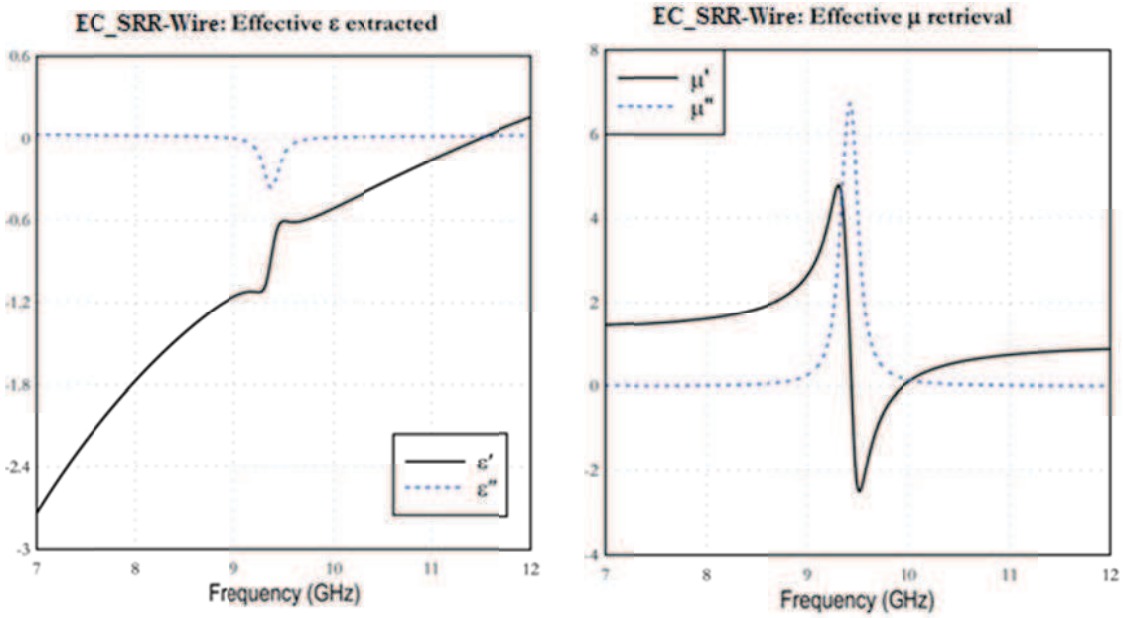

Figure 2-16: S-retrieved effective parameters for EC_SRR-Wire unit cell. Both extracted parameters show non-physical behavior

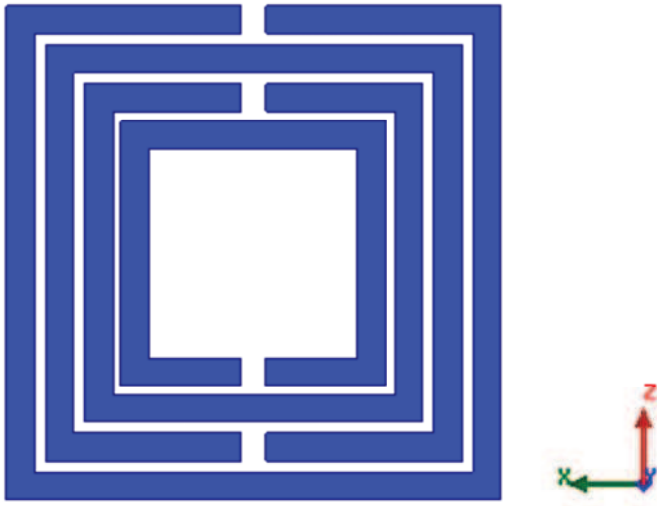

Figure 2-17: Top view of structure simulated in HFSS

An alternative procedure which we exploit is to calculate the dispersion diagram of an infinite number of unit cells in the propagation direction with certain phase shifts. In a first step, the numerically calculated Z parameters are transformed to ABCD parameters,

$$A = \frac{Z_{11}}{Z_{21}} \tag{2-49}$$

$$B = \frac{Z_{11}Z_{22} - Z_{21}^2}{Z_{21}} \tag{2-50}$$

$$C = \frac{1}{Z_{21}} \tag{2-51}$$

$$D = \frac{Z_{22}}{Z_{21}} \tag{2-52}$$

Then, the Bloch-Floquet theorem is used to calculate the Bloch impedance and the l-D Brillioun diagram from ABCD parameters with complex propagation constant γ and period d [2-20].

The effective permeability can then be easily calculated from Bloch impedance and propagation constant with free space wave number k_0 and line impedance Z_0 of the empty waveguide.

$$\gamma = \frac{\cos^{-1}\left(\frac{Z_{11} + Z_{22}}{2Z_{21}}\right)}{\mathrm{d}} \tag{2-53}$$

$$Z_{Bloch} = \frac{\mathrm{B}}{\exp(j\gamma d) - A} \tag{2-54}$$

$$\mu_{eff} = \frac{\gamma Z_{Bloch}}{k_0 Z_0} \tag{2-55}$$

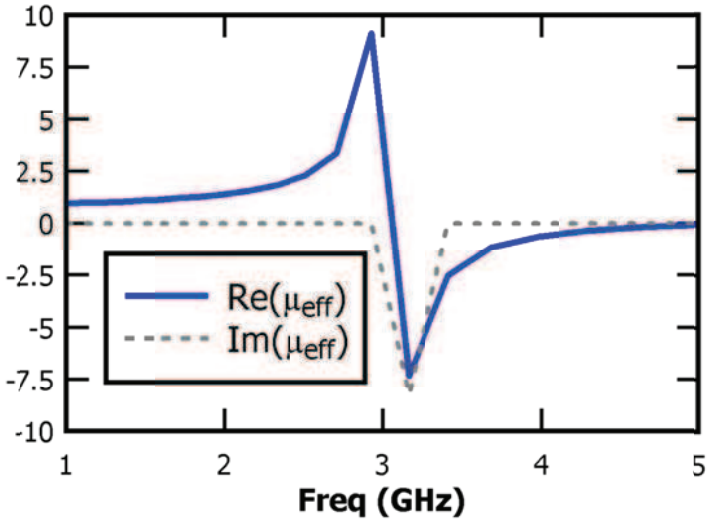

Figure 2-18: Real and imaginary parts of effective permeability

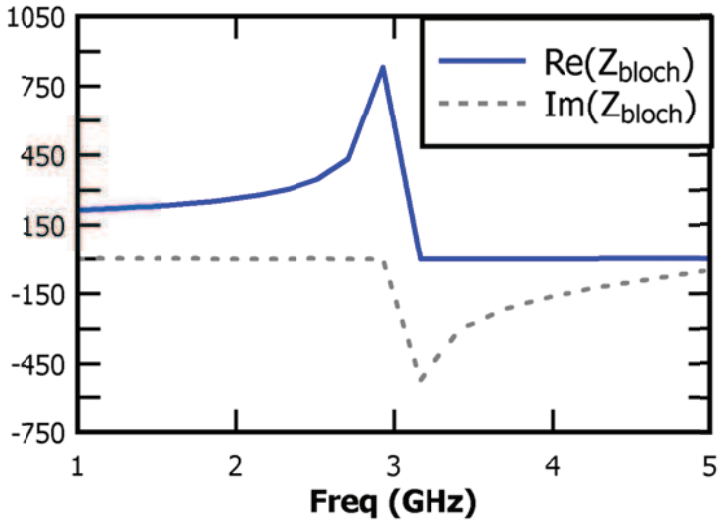

Figure 2-19: Real and imaginary parts of Bloch impedance

The effective permeability is shown in Figure 2-18 whereas Bloch impedance is shown in Figure 2-19. From Figure 2-18, the magnetic resonance frequency, 2.4 GHz, can be identified along with the resulting negative permeability, which is obtained between the magnetic resonance and plasma frequency. For additional knowledge, the computational procedure of this method is introduced in appendix C at the end of this thesis.

2.5.4 Averaging Method

If we have an effective medium, with only vacuum and responding currents (ε, μ) it is clear that we must apply appropriate averaging methods to compute effective material parameters. In fact, we may view the process as a discretization of Maxwell's equations, in which we replace the details of each unit cell by averaged fields and material constants. Pendry et al. introducing the following averaging scheme for the fields:

$$\langle \boldsymbol{E_i} \rangle = \boldsymbol{d^{-1}} \int \boldsymbol{E}.\boldsymbol{dx_i} \tag{2-56}$$

$$\langle \boldsymbol{D_i} \rangle = \boldsymbol{d^{-2}\epsilon_0} \int \boldsymbol{E}.\boldsymbol{ds_i} \tag{2-57}$$

$$\langle \boldsymbol{H_i} \rangle = \boldsymbol{\mu_0^{-1} d^{-1}} \int \boldsymbol{B}.\boldsymbol{dx_i} \tag{2-58}$$

$$\langle \boldsymbol{B_i} \rangle = \boldsymbol{d^{-2}} \int \boldsymbol{B}.\boldsymbol{ds_i} \tag{2-59}$$

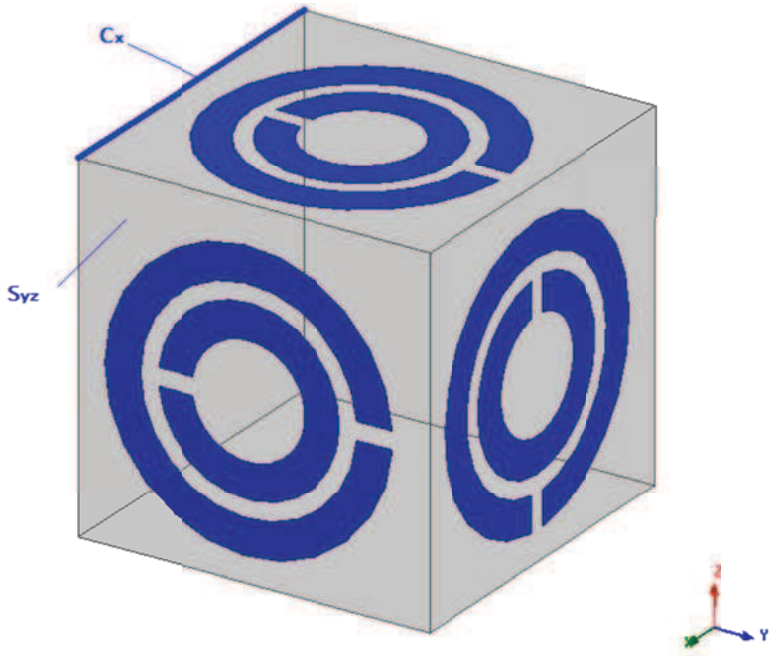

Figure 2-20: Example of a Unit Cell employed in the "Averaging method"

Where "d" is the length of an edge of the cell and "i" is one of the x, y, or z components. The averages for <E> and <H> involve line integrals along the edges of the unit cell shown in Figure 2-20, while the averages of <B> and <D> involve surface integrals over the faces of the cell. By following this scheme, the details of the actual structure are removed into the field averages, from which we can define the effective material parameters as:

$$\mu_{eff}^{i,j} = \frac{\langle B_i \rangle}{\langle H_j \rangle} \tag{2-60}$$

$$\epsilon_{eff}^{i,j} = \frac{\langle D_i \rangle}{\langle E_j \rangle} \tag{2-61}$$

The most straightforward of these is to use the field averages of (2-56) - (2-59) to compute the material parameters directly by the prescription shown in (2-60) - (2-61). When there is appreciable phase advance across a unit cell, however, we note that the averages are "incorrect" by a factor relating to the phase variation.

2.5.5 Other Retrieval Methods

After a long search to find the best method suggest for the extraction of the constitutive parameters, we found that all the method have its advantages and disadvantages and depend

mainly on the case under investigation. We will state many other methods more or less are suitable for some problems and fail for the others.

2.5.5.1 Smith's Field Averaging Method

In many MTM geometries, such as a SNG medium of continuous wires or a double negative combination of SRR-wires, a conducting element passes continuously from one unit cell to the next. For the flux averages to be correct in this case, the formulation of the effective medium parameters should be modified in order to include the contribution of the current flowing between the cells. Typically, as a more useful alternative, a gap is introduced in the wire near the integration surface so that the current is no longer continuous [2-21]. Moreover, the additional element in the MTM geometry can significantly increase the numerical costs.

2.5.5.2 Pendry's Field Averaging Method

The general idea relies on computation of the effective parameters from the electric and magnetic fields and fluxes averaged over certain spaces. A key question in this case is how to average the fields in order to obtain a reasonable representation of the Metamaterial under test. For the structures made of thin wires or sheets of metal, if the averages of fields and fluxes were taken over the same regions of space, ε_{eff} and μ_{eff} would always be constants related to the permittivity and permeability of the host material. Pendry et al. presented a straightforward approach based on averaging of the local fields. The integration surfaces, similar as the integration paths, cannot be crossed by any conducting element passing continuously from one unit cell to the next [2-21].This is a serious disadvantage of the method that limits its application to Metamaterial lattices not including continuous wires.

2.5.5.3 Acher's Field Averaging Method

As the field quantities are averaged over volume and surfaces instead of surfaces and lines, Acher's FAM is sometimes referred to as volume/surface approach (whereas Pendry's method is called surface/line averaging) [2-22]. Due to the application of the surface averages in the plane perpendicular to the direction of the electric field, Acher's method is characterized by the same disadvantage as Pendry's approach: "it cannot be directly applied to Metamaterials including continuous wires that would intersect the integration plane".

2.6 Metamaterials as Photonic Crystals

As Metamaterials do not satisfy the effective medium limit and they are conceptually located between homogeneous materials and photonic crystals as demonstrated in Figure 2-21, MTMs could be analyzed as lattices of periodically ordered single or double negative unit cells.

The description of photonic crystal as a periodic structure is valid for any ratio of the wave length related to the scale of in homogeneity.

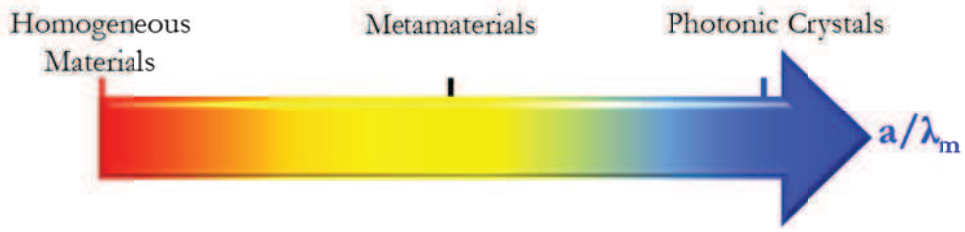

Figure 2-21: Materials classification according to a/λ_m

Here we will discuss the Bloch analysis and the Brillouin zone for a primitive cell based on the solid physics background. The explanations of the dispersion diagram and band gap are in relation to the different symmetries of the primitive cell.

Photonic crystals are characterized by band gap diagrams, also called dispersion diagram. The band diagram is plotted from the pairs of w(k) that are obtained from the solution of the Eigen value problem of the unit cell limited numerically with periodic boundary condition (PBC).

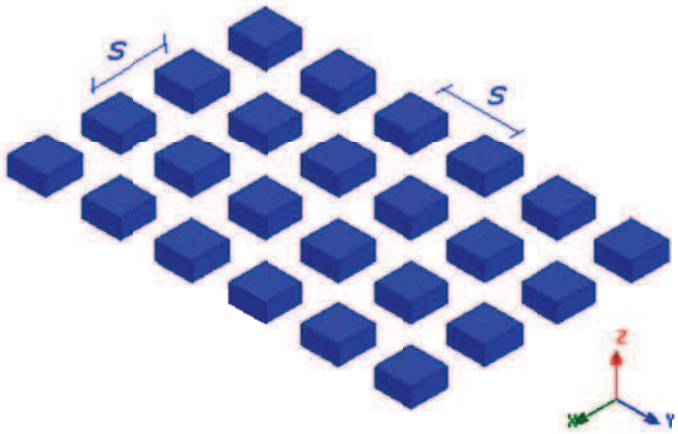

Figure 2-22: Square lattice of a two dimensional photonic crystal

The phase shift in a given direction of periodicity in combination with the lattice constant imposes the Bloch wave vector k, whereas the computed w values represent the Eigen frequencies of the analyzed periodic lattice. The Eigen values represent the squared angular Eigen frequencies of the system, whereas the Eigen vectors represent the electromagnetic field distribution of the Bloch modes supported by the periodic structure.

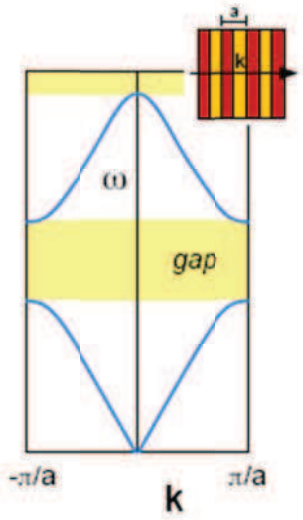

Figure 2-23: Dispersion relation (band diagram), frequency w versus wave number k, of a uniform one dimensional medium

The dispersion diagram, shown in Figure 2-23, can be presented in different ways, depending on the application of the considered photonic crystal. Usually, it is represented in 2 dimensional (2D) graphs of Eigen frequencies on the edge of the first reduced Brillouin zone.

Again a photonic crystal emerges from the translation of its unit cell and can be characterized by a various set of structural symmetries (inversion symmetry, mirror reflection, rotation…). Due to these symmetries, the infinite periodic lattice is represented by its irreducible Brillouin zone, i.e. a uniquely defined primitive cell of the reciprocal lattice that is reduced by all the symmetries in the point group of the lattice.

The square lattice (Figure 2-22) is a typical example of a two dimensional photonic crystal, consisting of dielectric columns embedded in free space. The photonic crystal is periodic along the x, y axes and homogeneous along the z axis. The lattice has a square reciprocal zone in wave vector space, whereas the irreducible Brillioun zone can be related to this wedge by rotational symmetry.

In photonic crystals, the period of the lattice is typically comparable to the operating free-space wavelength, the complete photonic band gap of the Yablonovite crystal occurs for frequencies corresponding to the lattice constant $0.5 < a/\lambda_0 < 0.6$ [2-25].

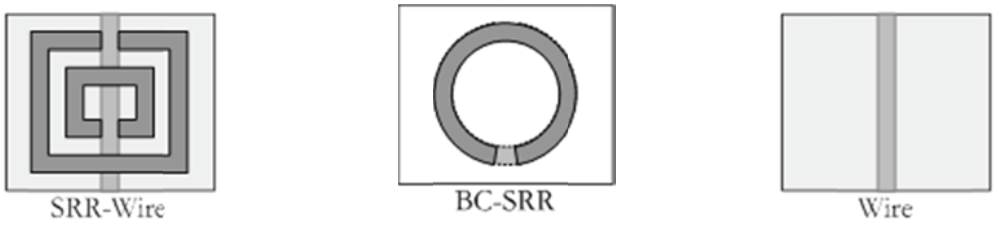

(a) **(b)** **(c)**

Figure 2-24: Top view of (a) SRR-wire, (b) BC-SRR and (c) Single wire

On the other hand, for Metamaterials analyzed the ratio of the lattice constant to free-space wavelength is about 1/7−1/6 for BC-SRR and SRR-Wire, whereas it can approach 1/4 in the case of the single negative wire medium (see Table 2-1).

Table 2-1: Ratio of lattice constant to free-space

Structure	Figure	Type	Freq (GHz)	a (mm)	a/λ_0 (mm)
SRR-Wire	Figure 2-24(a)	DNG	9.7-10.3	5	~1/6
BC-SRR	Figure 2-24(b)	SNG	4.5-4.6	10	~1/7
Wire	Figure 2-24(c)	SNG	< 15	5	< 1/4

As most Metamaterials are periodic structures with a finite size of the unit cell, the methods used for the analysis of photonic crystals may also be valuable for the characterization of Metamaterials. In principle, Metamaterials can be built as random mixtures of complex scatterers [2-26]. These structures, however, are less popular and not considered here.

2.6.1 SRR-Wire Structure

The Metamaterial lattice that is analyzed as a photonic crystal is formed by the double negative SRR-Wire based unit cells (see Figure 2-25). The measurements of the lattice formed by three layers of metallic patterns printed on a substrate, reported in [2-27], were conducted for the structure inserted in the parallel plate waveguide that ensures a proper polarization of the EM fields in the Metamaterial. The PEC boundaries at the top and bottom of the three-layered periodic lattice allow representing it by a single layer of SRRs and wires. According to the image theory, the layers are effectively repeated in the vertical direction as shown in Figure 2-27(c).

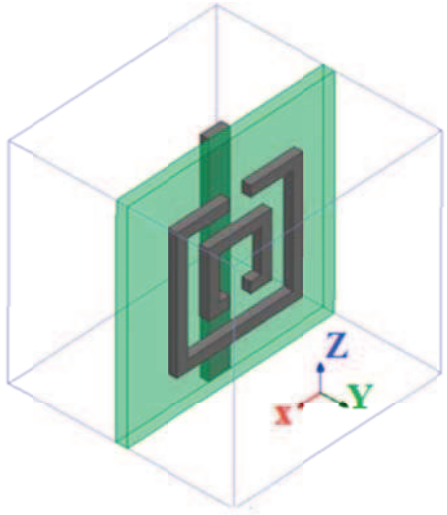

Figure 2-25: 3D view of a single unit EC_SRR-Wire

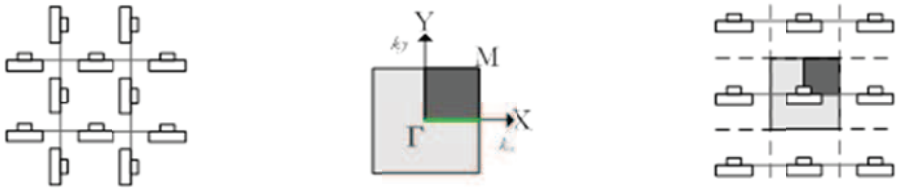

(a) **(b)** **(c)**

Figure 2-26: (a) Two-dimensional Metamaterial lattice (b) Face of the unit cell in the y-plane(c) Equivalent one dimensional lattice

The corresponding top view of the lattice is shown in Figure 2-24. As the propagation in the negative refraction experiment is limited to the x direction, the EM fields (E_z, H_y) interact mainly with the metallic inclusions patterned in the y plane and the lattice is effectively one-dimensional. This conclusion is supported by the study of transmission characteristics of parallel plate waveguides loaded with different orientations of split ring resonators.

Consequently, the two-dimensional Metamaterial lattice can be modeled by its one-dimensional equivalent shown in Figure 2-26c. In the 2D case, the irreducible Brillouin zone of this lattice contains four characteristic points: Γ, X and M, analogous to the case of a square lattice of dielectric rods, and additional Y point representing the face of the unit cell in the y plane and resulting from the lack of a rotational symmetry of the Metamaterial unit cell in the z plane (Figure 2-26b). For the 1D representation and propagation in the Metamaterial limited to the x direction, the relevant part of the irreducible Brillouin zone is its Γ− X edge.

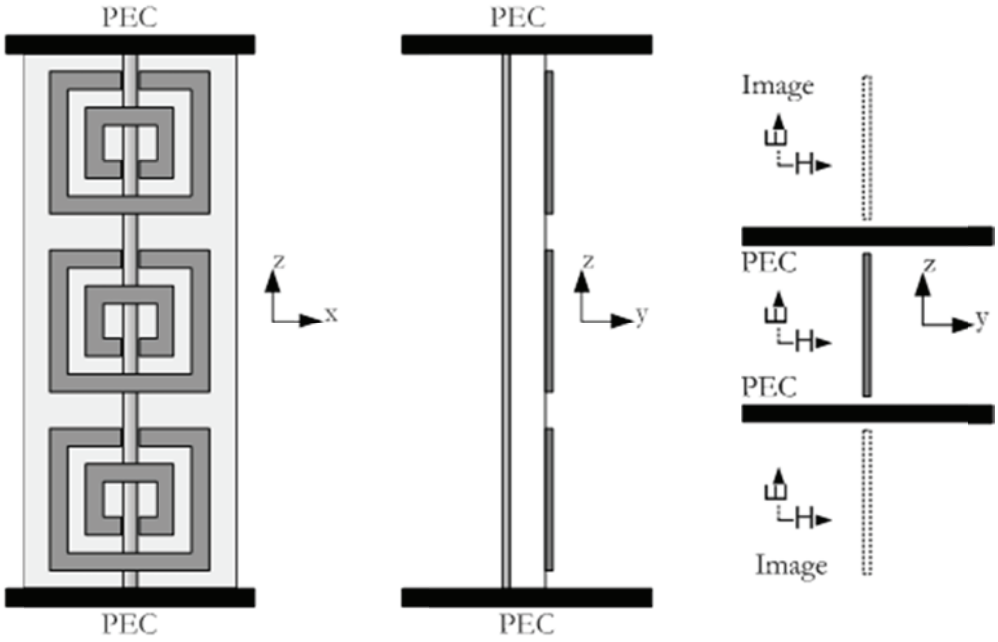

(a) **(b)** **(c)**

Figure 2-27: Three cells in a parallel plate waveguide

The band diagram of the Metamaterial lattice, computed with the Eigen mode solver using Ansoft HFSS and corresponding to the $\Gamma - X$ edge of the irreducible Brillouin zone is presented in Figure 2-28. PEC limits the unit-cell structure at the z boundaries of the unit cell, whereas in the x and y directions periodic boundary conditions (PBC) are used.

The transversal wave number k_y is assumed equal to zero and k_x, corresponding to the direction of propagation in the Metamaterial, is swept in the range $0 - \pi/a$ i.e. 180 degree. In the simulation, we assume that k_z is in the direction of propagation.

The dispersion diagram of the SRR-Wire unit cell shows two Eigen modes supported by the lattice up to the frequency of 20 GHz. The fundamental mode within the frequency range 9.9−10.1 GHz is characterized by the negative slope of the dispersive curve, as long as the wave vector magnitude k_z is less than $\pi/(3a)$ (or equivalently, the electrical size of the unit cell a/λ_m, where λ_m is the wavelength in the medium, is smaller than 1/6).

According to the homogenization of the photonic crystal theory, the negative slope of the dispersive curve indicates that the propagating mode is a backward wave and the medium is characterized by a negative refractive index that corresponds to double negative constitutive parameters.

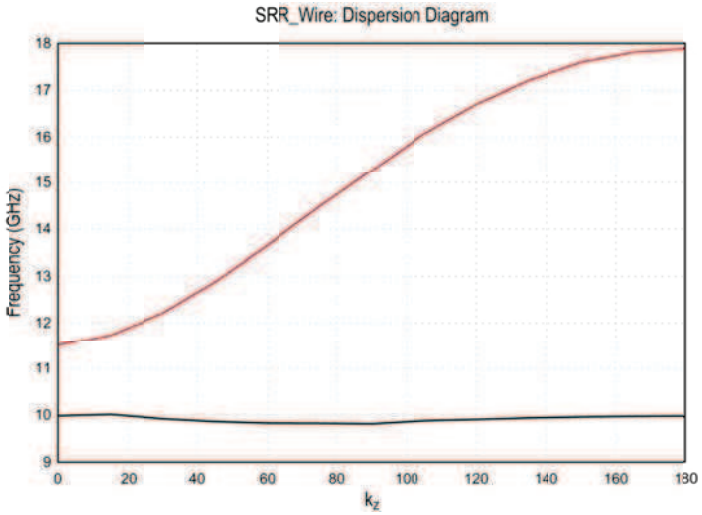

Figure 2-28: Band diagram of the Metamaterial lattice

In the range $\pi/(3a) < k_x < \pi/(2a)$ $(1/6 < a/\lambda_m < 1/4)$ the dispersion curve tends to flatten, corresponding to a very low group velocity ($d\omega/dk \approx 0$) and longer time constants in the interaction between the Metamaterial and the propagating wave [2-28]. Recent reports suggest that this type of mode is composed of counter propagating waves which results in the extremum away from the edge of the Brillouin zone [2-29]. For larger lattice constants $[k_x > \pi/(2a)]$ the fundamental mode changes its character to the forward wave. The second Eigen mode is supported in 11.6 − 18 GHz range, and the positive slope of the dispersive curve indicates its forward type.

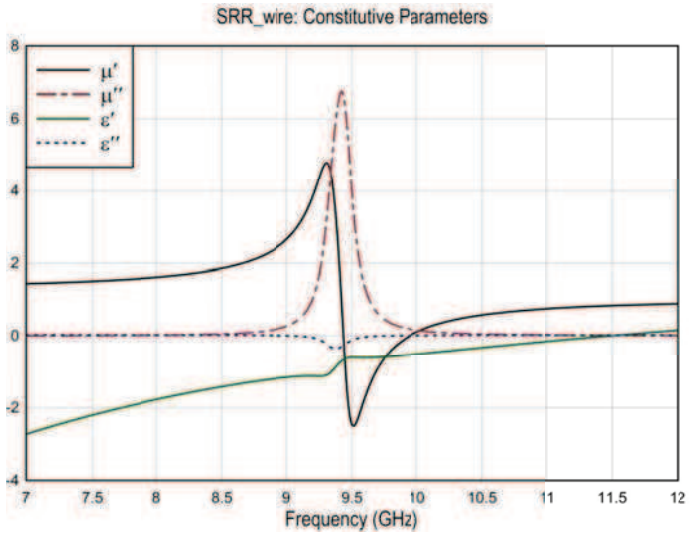

Figure 2-29: single or double negative constitutive parameters

In the frequency band of the second mode, the Metamaterial structure is described by a positive effective refractive index equivalent to double positive constitutive parameters ($\varepsilon' > 0$ and $\mu' > 0$).The frequency ranges obtained by Eigen mode solver Ansoft HFSS simulations and corresponding to single or double negative constitutive parameters (i.e. stopbands and passbands, respectively) are related to the results extracted with retrieval S-parameters method in Figure 2-29.

From Figure 2-29, it can be seen that the backward wave band of the first Eigen mode (9.8–9.98 GHz) fits in the double negative frequency range (9.4–9.98 GHz) extracted from scattering matrix. Moreover, the frequency band of the second Eigen mode matches the double positive constitutive parameters between 11.5 and 12 GHz.

Table 2-2: Results of both approaches mentioned above

Description type	Δf (GHz)	Band	Eigen mode	wave
SNG: $\varepsilon' < 0$ and $\mu' > 0$	7 - 9.4	Stop band	-	-
DNG: $\varepsilon' < 0$ and $\mu' < 0$	9.4 – 9.98	Band pass	first	backward
SNG: $\varepsilon' < 0$ and $\mu' > 0$	9.98 – 11.5	Stop band	-	-
DPS: $\varepsilon' > 0$ and $\mu' > 0$	11.5 - 18	Band pass	second	forward

The results of both approaches summarized in Table 2-2 shows a good agreement between the solution of the periodic boundary eigenvalue problem and the retrieval S-parameters extracted from scattering parameters. The discrepancy between the frequency bands related to the DNG range can be discussed on the number of modes used in the S-parameters calculation in the retrieval method used to extract the constitutive parameters.

2.6.2 BC-SRR Structure

The band diagrams are computed for single negative Metamaterials, i.e. BC-SRR. (Figure 2-30) unit cells. The field polarization and the direction of propagation are assumed analogous to the case of the SRR-Wire unit cell.

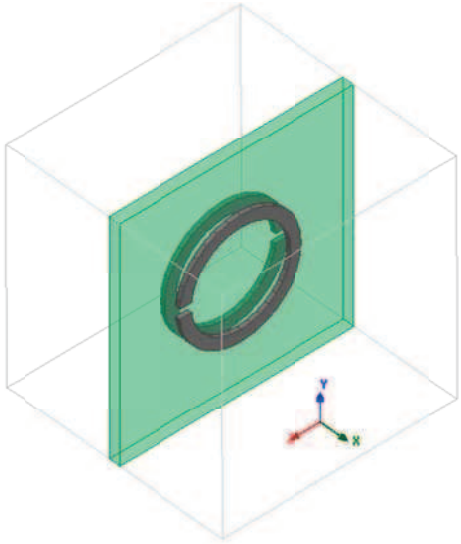

Figure 2-30: 3D view of a BC-SRR unit cell

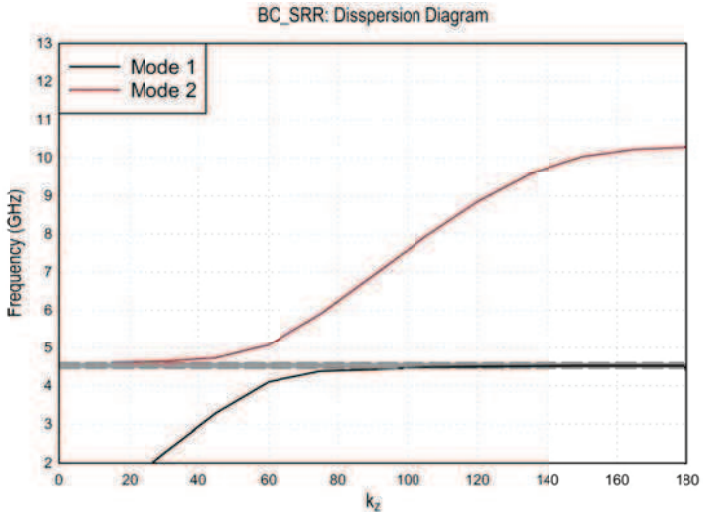

Figure 2-31: Dispersion diagram obtained for the broadside-coupled SRR

The dispersion diagram obtained for the broadside-coupled split ring resonator is shown in Figure 2-31. Up to the frequency of 4.5 GHz, there is one mode in the periodic structure, and the positive slope of its dispersion curve indicates the forward wave type.

The first band gap occurs for frequencies between 4.50 and 4.60 GHz and matches the single negative frequency band obtained by the S-parameters retrieval method as shown in Figure 2-32.

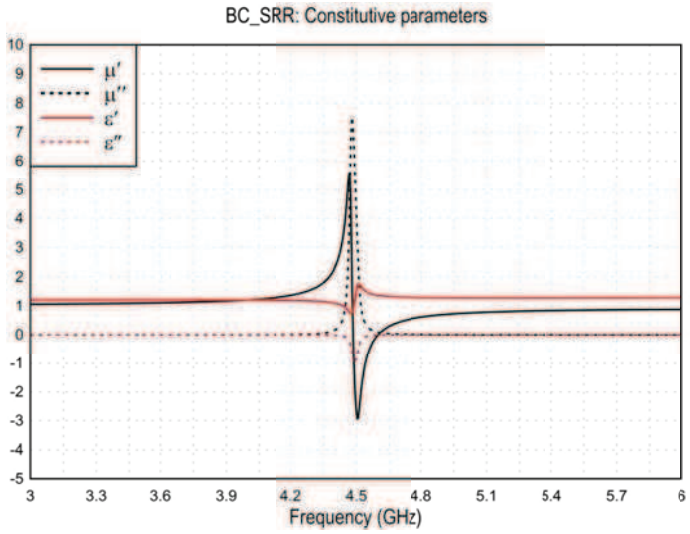

Figure 2-32: Single negative frequency band obtained by the S-parameters retrieval method

The second Eigen mode propagates in the lattice in the spectrum range 4.65−10.2 GHz and is also characterized by $\partial\omega/\partial k_x > 0$. The frequency bands of both forward waves correspond to double positive constitutive parameters of the BC-SRR effective description. A good agreement between the S-parameters retrieval method and Periodic Boundary Eigenvalue problem (PBE) is summarized in Table 2-3.

Table 2-3: S-parameters retrieval method and Periodic Boundary Eigen value problem (PBE)

Description type	Δf (GHz)	Band	Eigen mode	wave
DPS: ε' > 0 and μ' > 0	3–4.5	Band pass	first	forward
SNG: ε' > 0 and μ' < 0	4.5 – 4.58	Stop band	-	-
DPS: ε' > 0 and μ' > 0	4.58 - 6	Band pass	second	forward

2.6.3 Single Wire Structure

Another band dispersion diagram is computed for the single wire unit cell shown in Figure 2-33.

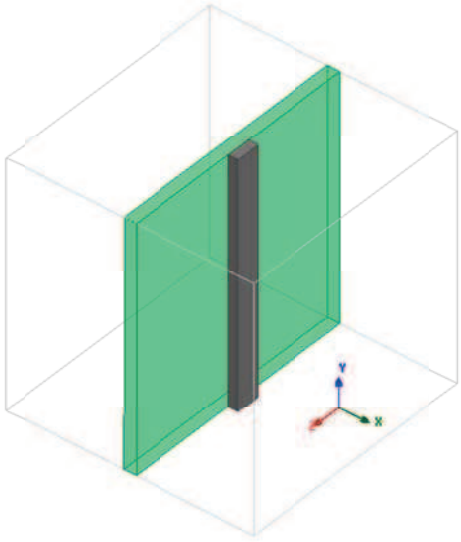

Figure 2-33: 3D view of a single wire unit cell

The dispersion diagram of a Wire unit cell is shown in Figure 2-34. The first Eigen mode of the periodic lattice describes the structure in the frequency range 14.9–24.8 GHz and is characterized by the positive slope of the dispersion curve that corresponds to the forward wave type.

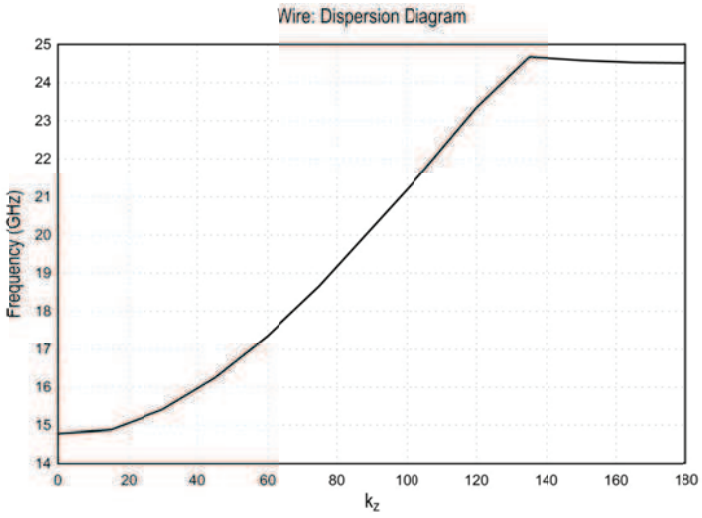

Figure 2-34: Dispersion diagram of a Wire unit cell

This Eigen mode starts to propagate at the frequency where effective electric permittivity ε' changes its sign from negative to positive at 14.8 GHz in Figure 2-34, which means that the solution of the eigenvalue problem is in good agreement with the S-parameters retrieval method extracted from frequency-domain simulations.

The results of the S-parameters retrieval method and PBE approaches applied to the Wire unit cell are summarized in Table 2-4. The solution of a periodic boundary eigenvalue problem presents a valuable tool that allows one to identify frequency ranges of forward and backward waves in a lattice, corresponding to double positive and double negative constitutive parameters, respectively.

Table 2-4: Results of the S-parameters retrieval method and PBE

Description type	Δf (GHz)	Band	Eigen mode	wave
SNG: ε' < 0 and μ' > 0	7.5 – 15	Stop band	-	-
DPS: ε' > 0 and μ' > 0	15 – 17.5	Band pass	first	forward

On the other hand, the band gaps represent the frequencies at which the structure is characterized by single negative parameters. Therefore, a PBE solution can be used for validation of the effective parameters extracted from a scattering matrix.

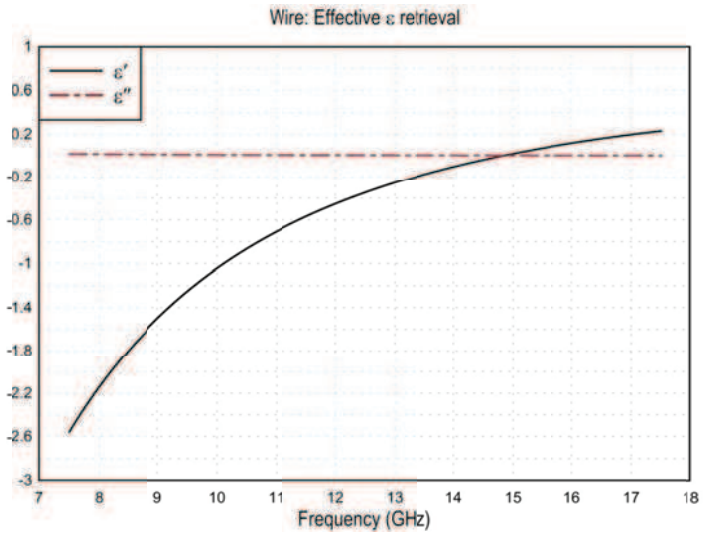

Figure 2-35: Effective electric permittivity

Moreover, it can be used for the extraction of the effective refractive index "n" for the Metamaterial structure under test. The band diagrams obtained with PBE approach are also useful in the design of Metamaterial based arrays.

2.7 Conclusion

In the first paragraph of this chapter, we presented classical Maxwell's equations that give two vector equations relating the field vectors of an EM wave by means of four dyadic parameters. All physical phenomena within the medium are hidden behind these four dyadic where the most general linear medium can be described in terms of these parameters. This general medium is also called magneto-electric or bianisotropic.

The second section of the chapter discusses bi-anisotropic materials. Anisotropic, bi-isotropic, chiral and non-reciprocal materials are examples of bi-anisotropic media. On the other hand, embedding metallic resonant particles showing cross polarization effects in a host dielectric medium is the usual technology for obtaining bi-isotropic and/or bianisotropic artificial media.

The bianisotropic effect for Metamaterials is then tested to extract the effective material parameters. The test is performed on a split ring resonator (SRR) of two different topologies; the broadside-coupled BC-SRR and the edge-coupled EC-SRR. The theoretical analyses show that depending on the orientation of the EC-SRR to the external EM fields, the structure can exhibit either a bianisotropic or non-bianisotropic behavior. On the other hand, the BC-SRR structure exhibits a non-bianisotropic effect due to the symmetry of the structure. This is an important result and will lead to a conclusion that the symmetrical structure has a lack of magnetoelectric coupling.

Another presented method is the extraction of the constitutive parameters of Metamaterial from transmission and reflection characteristics as well as from the ABCD parameters. A Matlab code for the retrieval procedure is written and the constitutive parameters are extracted one by one. The physical behavior of extracted effective permittivity or permeability by S-retrieval method was achieved where it is concluded that such parameters cannot form the effective description of a homogenized material.

Bloch analysis and the Brillouin zone for a primitive cell based on the solid physics background are then discussed. The Metamaterial lattice analyzed as a photonic crystal is formed by the double negative SRR-Wire, Wire, BC-SRR based unit cells. The results of both approaches show a good agreement between the solution of the periodic boundary eigenvalue problem and the retrieval S-parameters extracted from scattering parameters. For a single wire unit cell, The solution of a periodic boundary eigenvalue problem presents a valuable tool that

allows one to identify frequency ranges of forward and backward waves in a lattice, corresponding to double positive and double negative constitutive parameters, respectively.

2.9 References

[2-1] J. Garcia-Garcia, F. Martin, J. D. Baena, and R. Marques, "On the resonances and polarizabilities of split ring resonators," J. Appl. Phys., vol. 98, pp. 033103-1–9, Sep. 2005.

[2-2] J. Pitqrke, F. G. a Vidal, and J. Pendry, Phys. Rev. B 57, 15 261 (1998).

[2-3] J. Pendry, A. Holden, D. Robbins, and W. Stewart, IEEE Trans. Microwave Theory Tech. 47, 2075 (1999).

[2-4] Sihvola A H and Lindell I V 1995 Magnetoelectricproperties of reciprocal bi-anisotropic materials withfocus on the polarizability of chiro-omega spheres *Int. J.Appl.Electromag.Mech.* **6** 113–30.

[2-5] Lindell I V, Sihvola A H, Tretyakov S A and Viitanen A J1994 *Electromagnetic Waves in Chiral and Bi-isotropicMedia* (Boston: Artech House)

[2-6] Lindell I V, Sihvola A H and Suchy K 1995 Six-vectorformalism in electromagnetics of bianisotropic media*J.Electromag. Waves Appl.* **9** 887–903.

[2-7] Padilla, W. J. (2007). Group theoritical description of artificial electromagnetic Metamaterials. *Optics Express, 15*, 1639-1646.

[2-8] Baena, J. D., Jeilnek, L., & Marques, R. (2007). Towards a systematic design of isotropic bulk magnetic Metamaterials using the cubic point groups of symmetry. *Physical Review B, 76(12)*, 245115(1-14).

[2-9] Koschny, T., Zhang, L., & Soukoulis, C. M. (2007). Isotropic three-dimensional left-handed Metamaterials. *Physical Review B, 71(12)*, 121103(1-14).

[2-10] Marques, R., Martin, F., & Sorolla, M. (2007). *Metamaterials with negative parameters, theory, design, and microwave applications*. John Wiley and Sons.

[2-11] Garcia-Garcia, J., Martin, F., Baena, J. D., Marques, R., & Jelinek, L. (2005). On the resonances and polarizabilities of split ring resonator Metamaterial. *Journal of applied physics, 98*, 033103(1-9).

[2-12] Nicolson, A. M., & Ross, G. F. (1970). Measurement of the intrinsic properties of materials by time-domain techniques. *IEEE Transactions on Instrumentation and Measurement*, (pp. 377-382).

[2-13] Markos, P., & Soukoulis, C. M. (2003). Transmission properties and effective electromagnetic parameters of double negative Metamaterials. *Optic Express, 11(7)*, 649-661.

[2-14] Smith, D. R., Schultz, S., Markos, P., & Soukoulis, C. M. (2002). Determination of effective permettivity and permeability of Metamaterials from reflection and transmission coefficients. *Physical Review B, 65*, 195104(1-5).

[2-15] Chen, X., Grzegorczyk, T. M., Wu, B. I., Pacheo, J., & Kong, J. A. (2004). Robust method to retriev the constitutive effective parameters of Metamaterials. *Physical Review E, 70*, 016608(1-7).

[2-16] koschny, T., Markos, P., Economou, D. R., Smith, D. R., Vier, D. C., & Soukoulis, C. M. (2005). Impact of inherent periodic structure on effective medium description of left handed and related Metamaterials. *Physical Review B, 71(24)*, 245105(1-22).

[2-17] Ziolkowski, R. W. (2003). Design, fabrication and testing of double negative Metamaterials. *IEEE Transactions on Antennas and propagation, 51(7)*, 1516-1529.

[2-18] Chen, X., Grzegorczyk, T. M., Wu, B. I., Pacheo, J., & Kong, J. A. (2004). Robust method to retriev the constitutive effective parameters of Metamaterials. *Physical Review E, 70*, 016608(1-7).

[2-19] D. R. Smith, D. C. Vier, Th. Koschny, and C. M. Soukoulis, "Electromagnetic parameter retrieval from inhomogeneous Metamaterials", Phys. Rev. E 71, 036617, 2005.

[2-20] Christophe Caloz, Tatsuo Itoh, Electromagnetic Metamaterials:Transmission Line Theoryand Microwave Applications, Wiley,John & Sons, Incorporated,2005

[2-21] Smith, D. R., & Pendry, J. B. (2006). Homogenization of Metamaterials by field averaging (invited paper). *Journal of Optical Society of America B, 23(3)*, 391-402.

[2-22] Acher, O., Lerat, J. M., & Mallejac, N. (2007).Evaluation and illustration of the properties of metatmaterials using field summation. *Optic Express, 15(3)*, 1096-1106.

[2-23] D. Pines and D. Bohm, Phys. Rev. 85 338 (1952)

[2-24] D. Bohm and D. Pines, Phys. Rev. 92 609 (1953)

[2-25] J.D. Joannopoulos, R.D. Meade, and J.N. Winn."*Photonic crystals: molding theflow of light*". Princeton University Press, 1995.

[2-26] A. Sihvola. "Metamaterials in electromagnetics".*Metamaterials*, 1(1):2–11, 2007.

[2-27] R.A. Shelby, D.R. Smith, and S. Schultz."Experimental verification of a negative index of refraction",*Science*, 292:77–79, 6 Apr 2001.

[2-28] J.M. Lourtioz, H. Benisty, V. Berger, J.M. Gerard, D. Maystre, and A. Tschelnokov, "*Photonic crystals: towards Nano scale photonic devices*", Springer, 2005.

[2-29] M. Ghebrebrhan, M. Ibanescu, S.G. Johnson, M. Soljacic, and J.D. Joannopoulos, "Distinguishing zero-group-velocity modes in photonic crystals". *Physical Review* A,76:063810(1–6), 14 Dec 2007.

Chapter 3 Inclusion Designs and Applications

3.1 Introduction

Within the huge number of new applications of Metamaterials, one of the most productive ones is the implementation of microwave devices by means of artificial transmission lines. The following sections will deal with one of the approaches devoted to this purpose: the resonant-type approach.

Different sub-wavelength resonators employed in the design of Metamaterial transmission lines based on the resonant-type approach will be studied. The equivalent circuit models of different kinds of Metamaterial transmission lines, as well as the parameter extraction methods employed as design and corroboration tools will be also presented. In closing, a selection of application examples of resonant-type Metamaterial transmission lines in the design of microwave devices will be presented.

3.2 Sub-wavelength Resonators

The implementation of the first effective medium with left handed properties[3-1] was possible thanks to the employment of small metallic resonators known as split ring resonators (SRRs).

3.2.1 Split Ring Resonators (SRR)

These resonators had been previously presented as the first non-magnetic resonator capable of exhibiting negative values of the magnetic permeability around its resonance frequency. This was one of the characteristics which made the SRR suitable for the synthesis of such a medium; the second one was its small electrical size.

At the resonance frequency, the SRR perimeter is smaller than half the wavelength of the exciting wave. These small dimensions allow the use of SRRs in the implementation of effective media, which requires small unit, cell sizes (smaller than the wavelength). By this means, the

incident radiation does not detect the internal configuration of the medium, but the effective properties of the whole medium.

The split-ring resonator is formed by two concentric metallic open rings (see Figure 3-1). The resonator can be excited by an axial time-varying external magnetic field, which induces currents in the rings. The splits present in the rings force the current to flow as displacement current between them. The current loop is thus closed through the distributed capacitance that appears between the inner and the outer ring.

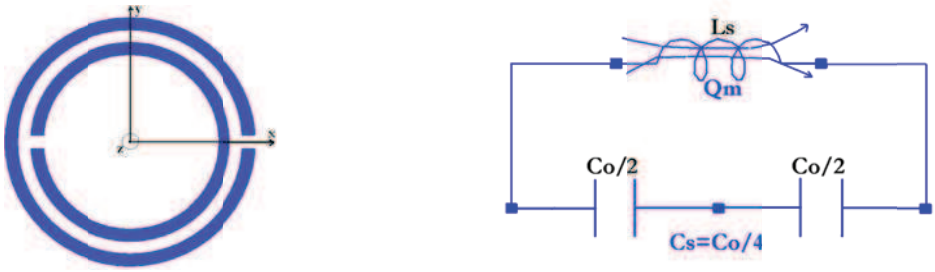

Figure 3-1: Split-ring resonator and its equivalent circuit

The resonator can be modeled as is shown in Figure 3-1[3-4]. $C_0/2$ is the capacitance related with each of the two SRR halves, whereas L_s is the resonator self inductance. C_0 can be obtained as $C_0=2\pi C_{pul}$, where C_{pul} represents the per unit length capacitance between the rings forming the resonator. As for L_s, it can be approximated to the inductance of a single ring with the average radius of the resonator and the width of the rings "c". Taking into account the circuit model of the resonator, its resonance frequency can be calculated as:

$$\omega_0 = \frac{1}{\sqrt{L_s C_s}} \tag{3-1}$$

As long as the inductance and the capacitance of the resonator can be increased (within the technology limits), the resonance frequency of the SRR can be decreased, reducing its electrical size.

The SRR resonator can be employed in the synthesis of effective media [3-1] and meta-surfaces [3-5], as well as, of course, artificial transmission lines [3-5], [3-6].

Taking SRR as a starting point, numerous resonators have been proposed. The new resonators are obtained by modifying the original topology in order to decrease the electrical size or obtain certain symmetry properties. In Figure 3-2, two different resonators can be found. The

first one is known as non-bianisotropic split-ring resonator. It has the same electrical size as the SRR, but it has been designed to avoid the cross polarization (bianisotropic) effects that the original SRR exhibits [3-4]. The electrical size can be reduced enhancing either the capacitance or the inductance of the resonator. This is achieved in the spiral resonator (Figure 3-2(b)) thanks to the increase of the total capacitance of the resonator in such a way that the resonance frequency is half the one of the SRR.

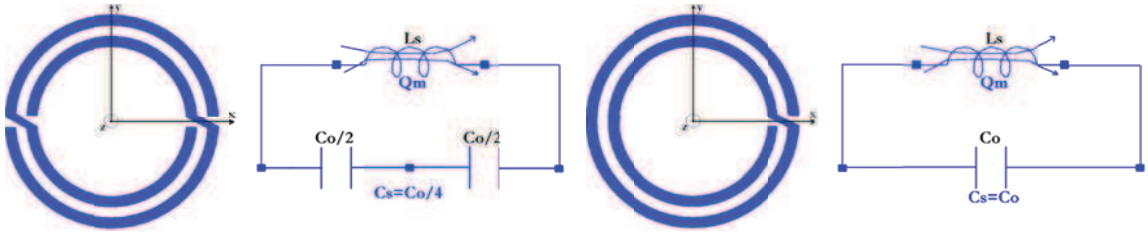

(a) **(b)**

Figure 3-2: SRR-based resonators and their circuit models. (a) Non-bianisotropic SRR (b) Spiral Resonator (SR)

3.2.2 Spiral Resonator (SR)

There are other strategies devoted to the miniaturization of the resonators. One of them is the addition or enlargement of the metallic strips in order to increase the inductance of the whole structure. One example of the application of this strategy is the spiral resonator (SR) shown in Figure 3-3(a) [3-7]; [3-8]. On the other hand, the capacitance can be enhanced designing the resonator so that their strips are broad-side coupled (see broad-side coupled SRR in Figure 3-3(b)) [3-9]. This strategy requires the use of two metal layers on which lay the different parts of the resonator. By this means the strips are broadside instead of edge-side coupled and the capacitance is enhanced, especially if thin substrates are employed.

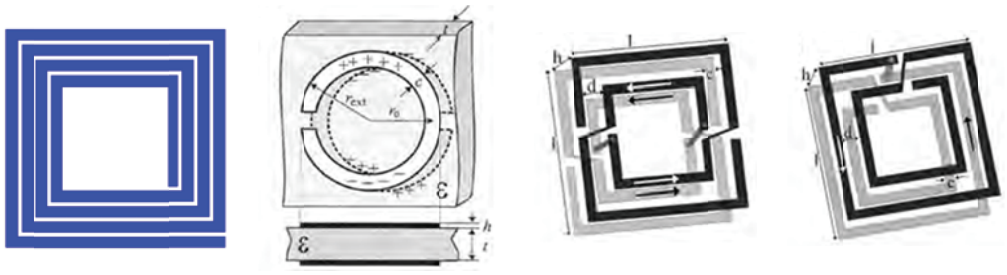

(a) **(b)** **(c)** **(d)**

Figure 3-3: SRR-based compact resonators. (a) Spiral resonator with 8 loops. (b) Broadside coupled split-ring resonator (BC-SRR). (c) Two-layer multi spiral resonator (TL-MSR). (d) Broad-side coupled spiral resonator with four turns

Both strategies are combined in the examples shown in Figure 3-3(c) and Figure 3-3(d) [3-10]. In these two resonators the strips are elongated connecting the two metal layers by means of vias, increasing the inductance of the resonator. Additionally, the capacitance is enhanced thanks to the broadside coupling. Following these strategies, the electrical size of the resonators can be drastically reduced.

3.2.3 Numerical Investigation

The numerical investigation for different types of inclusions was conducted via a FEM method simulation program using HFSS. However, the simulation result was in good agreements with the theoretical explanation.

3.2.3.1 SRR and SR Resonators

In order to prove the circuit models presented in the previous paragraphs, SRR and SR resonators depicted in Figure 3-1 and Figure 3-2(b) respectively, are subjected to electromagnetic simulation in HFSS environment. The two structures employed in this investigation are shown in Figure 3-4.

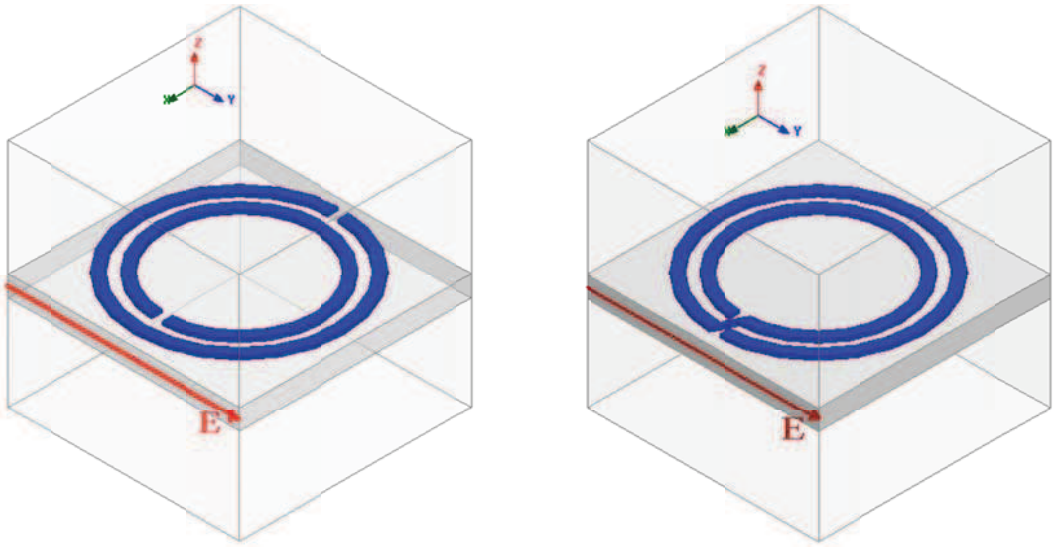

(a) **(b)**

Figure 3-4: 3D view of the structures simulated in HFSS (a) SRR (b) SR. Inclusion dimensions are: a= 11mm, r_{ext}=5mm, d=c=0.5mm, g=0.5mm, substrate thickness t=1mm, material FR4

Note that the equivalent capacitance of the SRR is $C_0/4$ whereas it is C_0 for the spiral resonator. So, we expect to find that the resonant frequency of the SRR is the twice of that of the SR.

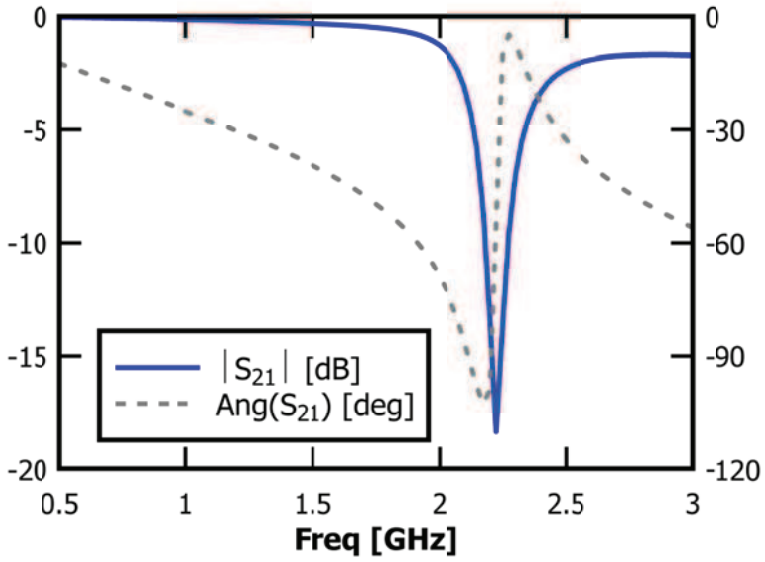

Figure 3-5: Transmission coefficient S_{21} of the SRR. The resonance frequency is 2.25GHz

This is well examined from the simulation results in Figure 3-5 and Figure 3-6 which show that the resonant frequency of the SR (1.2 GHz) is approximately the half of the frequency of the SRR (2.25 GHz). The spiral resonator is preferred over the split ring resonators for low frequency applications, especially in the UHF, L band applications.

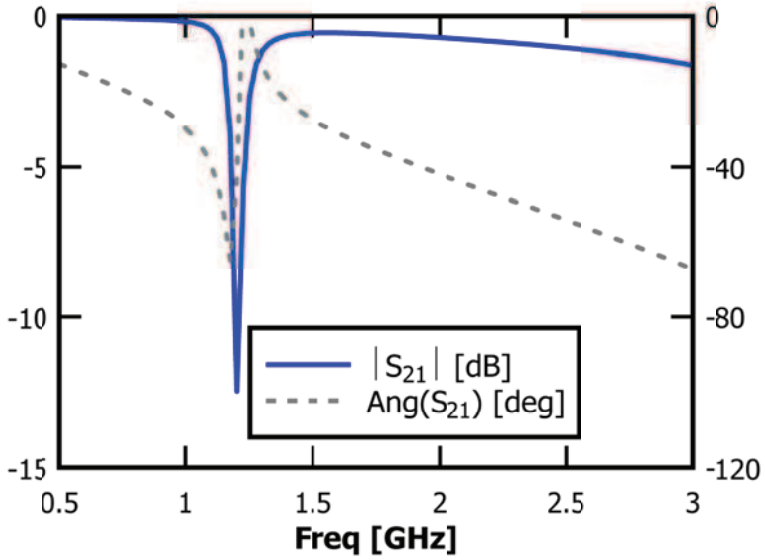

Figure 3-6: Transmission coefficient S_{21} of the SR. The resonance frequency is 1.20GHz

3.2.3.2 Rectangular Spiral Resonator (RSR)

Another investigation is conducted to show the response of the rectangular spiral resonator (RSR) shown in Figure 3-7. The dimension of the unit cell "a" is the same as the SRR.

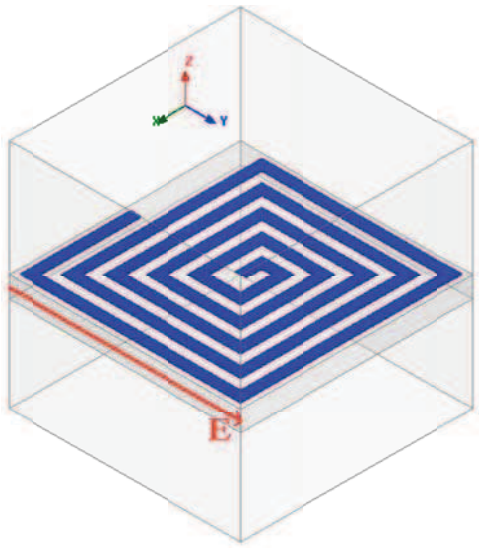

Figure 3-7: 3D view of RSP structure simulated in HFSS. Inclusion dimensions are: a=11mm, l_{ext}=10mm, w=s=0.5mm, g=0.5mm, substrate thickness t=1mm, material FR4

The simulation results are shown in Figure 3-8. It is clear from the transmission coefficient S21 that the resonance frequency of the inclusion is 700MHz. Also we note that the structure is a non-bianisotropic type.

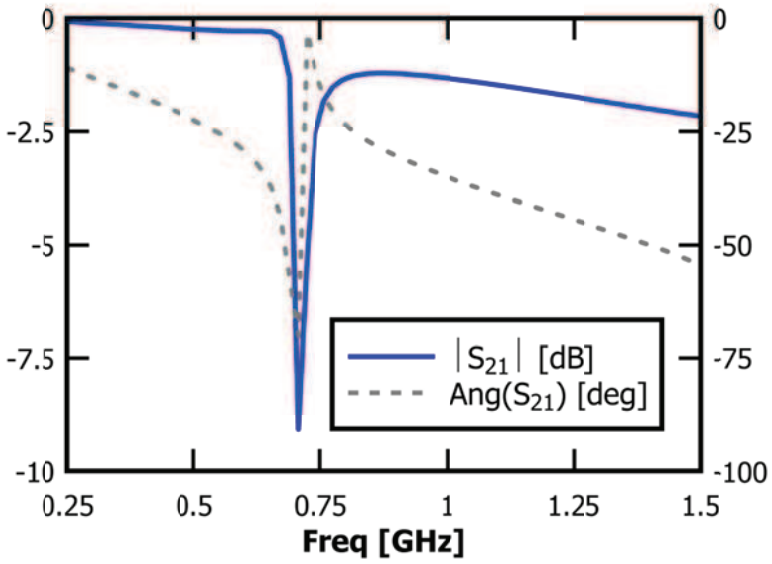

Figure 3-8: Transmission coefficient S_{21} of the RSR. The resonance frequency is 700MHz

3.2.4 Open Complementary SRR (OCSRR) and Open SRR (OSRR)

Different kind of SRR-based structures are open resonators. Figure 3-9 shows the layouts and equivalent circuit models of the open SRR [3-11] and the open complementary SRR [3-12]. As can be seen in the layout, the OSRR is based on the SRR and is obtained by truncating the

rings forming the resonator and elongating them outwards. The OCSRR can be obtained as the complementary particle of the OSRR. The resonators shown in Figure 3-9 can be implemented either in microstrip or in coplanar technology [3-13].

The equivalent circuit models of the resonators are also shown in Figure 3-9. The equivalent circuit model of the OSRR is a series LC resonator [3-11]. The inductance L_s can be obtained as the inductance of a ring with the average radius of the resonator and the same width, c, of the rings forming the OSRR. The capacitance C_0 is the distributed edge capacitance that appears between the two concentric rings.

In a similar way, the OCSRR can be modeled by means of a parallel LC resonant tank [3-12], where the inductance L_0 is the inductance of the metallic strip between the slot hooks and the capacitance is that of a disk with radius r_0-c/2 surrounded by a metallic plane separated by a distance c.

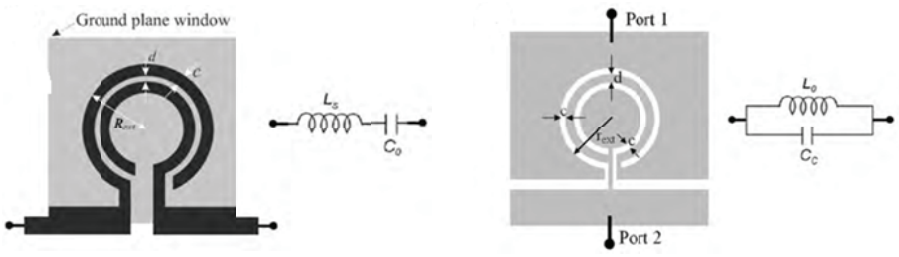

(a) **(b)**

Figure 3-9: (a) Open split-ring resonator (OSRR) and its equivalent circuit model. (b) Open complementary split-ring resonator (OCSRR) and its equivalent circuit model

The small size of all these resonant particles makes them suitable for the implementation of microwave devices based on resonant-type Metamaterial transmission lines with small dimensions and even new functionalities.

3.2.5 Multi Split Ring Resonator (MSRR)

A basic idea to reduce the dimensions of the resonant inclusions is to use multiple split-ring resonators (MSRRs) consisting of concentric split-rings, in order to increase the distributed capacitance between the strips without increasing the area occupied by the resonator. Even if the MSRR is a natural extension of the SRR, there are no papers reporting accurate design formulas for this kind of magnetic inclusion. One of the aims of this work is to show a proposed circuit model for the MSRR, which gives accurate results if compared with full-wave numerical simulations.

Since the inclusions are supposed to be very small compared to the operating wavelength, a quasistatic model may be used to describe the electromagnetic behavior of MSRRs. An MSRR inclusion consists of concentric split-rings with splits placed on the opposite sides of two consecutive rings. From this definition, it is evident that the SRR is a particular case of the MSRR with N=2.

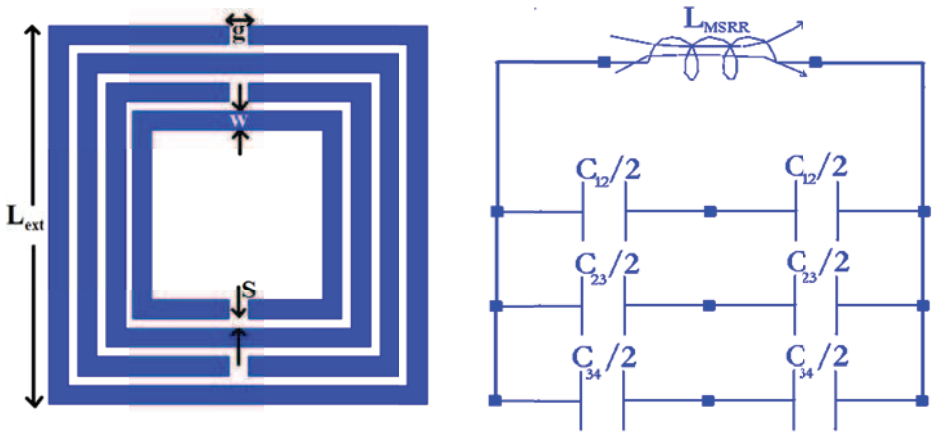

(a) **(b)**

Figure 3-10: (a) an example of a MSRR with N = 4 split-rings. (b) Quasi-static equivalent circuit of the MSRR

In Figure 3-10(a), a MSRR inclusion with N=4 split-rings is depicted. Extending the formulation reported in [3-4] and [3-14] for the case of the regular SRR, it easy to verify that in the quasi-static limit the current flows through the rings of the inclusion as reported in Figure 3-10(a). In the case of a MSRR, N-1 distributed capacitances between adjacent rings have to be considered.

Numbering the rings from the outer one to the most inner one, the distributed capacitances may be represented as C_{12}, C_{23}, …, $C_{(N-1)N}$, where the subscript reports the numbers associated to the two rings between which the distributed capacitance is calculated. As already outlined in [3-4] and [3-14] for the case of the SRR, when the two rings are excited in their fundamental mode, due to the voltage and current distributions, the distributed capacitance between the first half (with respect to the vertical dashed line in Figure 3-10(a)) of the two rings is in series with the one associated to the second half.

From the current flow schematically described in Figure 3-10(a) and from the voltage distribution, which for each pair of rings resembles the one reported in [3-14] for the SRR, it is clear that the distributed capacitances of adjacent rings are all connected in parallel. Therefore,

following this formulation, the equivalent circuit representation of the MSRR depicted in Figure 3-10(a) is the one reported in Figure 3-10(b).

This equivalent circuit neglects some high-order effects, which have, anyway, a slight influence in the determination of the resonant frequency of the inclusions. Namely, the mutual inductances between the parallel stems of the inclusion, the mutual capacitances between non adjacent rings and the split capacitances are neglected in the model.

3.2.5.1 Analytical Derivation

In order to derive the expressions of the inductance and of the distributed capacitances of the proposed model, we assume that the strip width ω, the separation between two adjacent rings, and the length of the split do not vary from a ring to another. We assume also that the inclusion is surrounded by free-space. The total strip length of the generic n^{th} ring is determined as:

$$\boldsymbol{l_n = 4[l - 2w(n-1) - 2s(n-1)]} \tag{3-2}$$

Being *l* the side length of the outer ring. We derive at first the expression of the total capacitance C_{MSRR}, given by the parallel of the n-1 capacitances associated to each separation between two adjacent rings. The general expression is given by:

$$\boldsymbol{C_{MSRR} = \sum_{n=1}^{N-1} \frac{C_{n(n+1)}}{4}} \tag{3-3}$$

where $C_{n(n+1)}/4$ is the series between the two equal-valued distributed capacitances $C_{n(n+1)}/2$ between the two halves of the n^{th} and the $(n+1)^{th}$ rings. The total distributed capacitance $C_{n(n+1)}$ between such rings can be expressed as:

$$\boldsymbol{C_{n(n+1)} = [l_{n+1} + 2(w+s)]C_0} \tag{3-4}$$

Being C_0 the per-unit-length capacitance between two parallel strips having width ω and separation *s*, given by:

$$\boldsymbol{C_0 = \varepsilon_0 \frac{K(\sqrt{1-k^2})}{K(k)}} \tag{3-5}$$

Where K(-) is the complete elliptic integral of the first kind and

$$k = \frac{s/2}{w + s/2} \tag{3-6}$$

Using (3-2) and (3-4), the total capacitance can be expressed as:

$$C_{MSRR} = \frac{N-1}{2}[2l - (2N-1)(w+s)]C_0 \tag{3-7}$$

Examine now the behavior of the total distributed capacitance C_{MSRR} as a function of the number N of the rings ($N \geq 2$). When the number N of the rings increases, it is expected that the contribution of the distributed capacitances associated to the inner rings is progressively less significant. Therefore, we expect that the curve describing the behavior of C_{MSRR} as a function of the number N of the rings has at a certain point a flat slope. This happens in correspondence of $N=N_{max}$, when there is no more space to place further concentric rings in the middle of the MSRR.

The derivation of an effective expression for the inductance when defining the equivalent circuit model of the SRR is considered from one of the circular (or squared) loop having an equivalent radius (or side) given by the average between the inner and the outer radii (or sides) of the rings [[3-15]–[3-17]. Using these formulas, it is not possible to take properly into account how the multiple rings fill the available area. An accurate formula should consider also this effect and, thus, involve the so called fill ratio (ρ) which takes into account how hollow the MSRR is. The expression of the fill ratio adapted to the case of the MSRR is given by:

$$\rho = \frac{l - l_N}{l + l_N} = \frac{(N-1)(w+s)}{l - (N-1)(w+s)} \tag{3-8}$$

The fill ratio is a function of all the geometrical parameters involved in the determination of the response of the MSRR (*l*, *w*, *s*, and N). Finally, the expression of the total inductance of the spiral inductor, which is similar to that, for the MSRR is derived as:

$$L_{MSRR} = \frac{\mu_0}{2}\frac{l_{avg}}{4}4.86\left[\ln\left(\frac{0.98}{\rho}\right) + 1.84\rho\right] \tag{3-9}$$

where is the average strip length calculated over all the rings as:

$$L_{avg} = \frac{1}{N}\sum_{n=1}^{N} l_n = 4[l - (N-1)(s+w)] \tag{3-10}$$

Using (3-10) the final expression for the inductance of the MSRR is derived in the following analytical form:

$$L_{MSRR} = 4\mu_0[l-(N-1)(s+w)]\left[\ln\left(\frac{0.98}{\rho}\right)+1.84\rho\right] \quad (3\text{-}11)$$

3.2.5.2 Numerical Investigation: MSRR Resonators

In order to prove the circuit models presented in the previous paragraphs, MSRR resonators depicted in Figure 3-10(a) is subjected to electromagnetic simulation in HFSS environment. The structure employed in this investigation is shown in Figure 3-11.

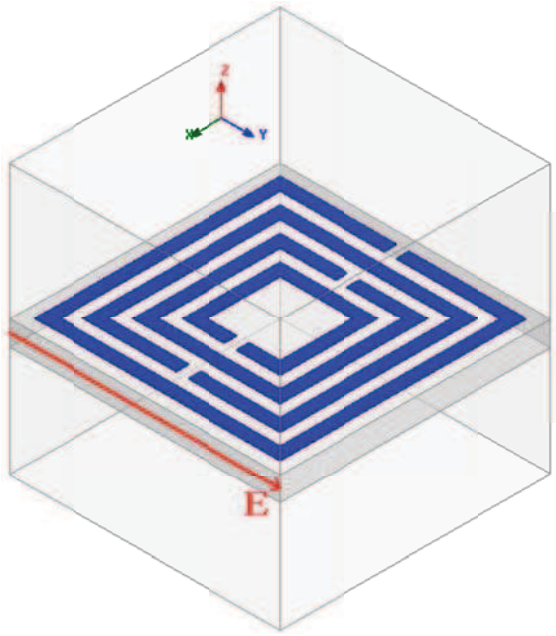

Figure 3-11: 3D view of the MSRR structure simulated in HFSS. Inclusion dimensions are: a=11mm, l_{ext}=10mm, w=s=0.5mm, g=0.5mm, substrate thickness t=1mm, material FR4

Note that the equivalent capacitance of the MSRR is 3×C/4. So, we expect to find that the resonant frequency of the MSRR is lower than that of SSR for the same structure dimensions.

This is well examined from the simulation result in Figure 3-12 which shows that the resonant frequency of the MSRR (1.825 GHz). The MSRR spiral resonator is preferred over the split ring resonators for low frequency applications, especially in the UHF, L band applications.

Another important note is that the MSRR bianisotropic effect exists, however the SR inclusion is a non-bianisotropic structure.

Also we have studied an MSRR unit cell, depicted in Figure 3-13. It consists of four rings parameterized in such a way that the width w and the spacing s of the ring can be varied simultaneously. After the simulation environment setup using an Eigen mode solver from Ansoft, the results are shown in Figure 3-14.

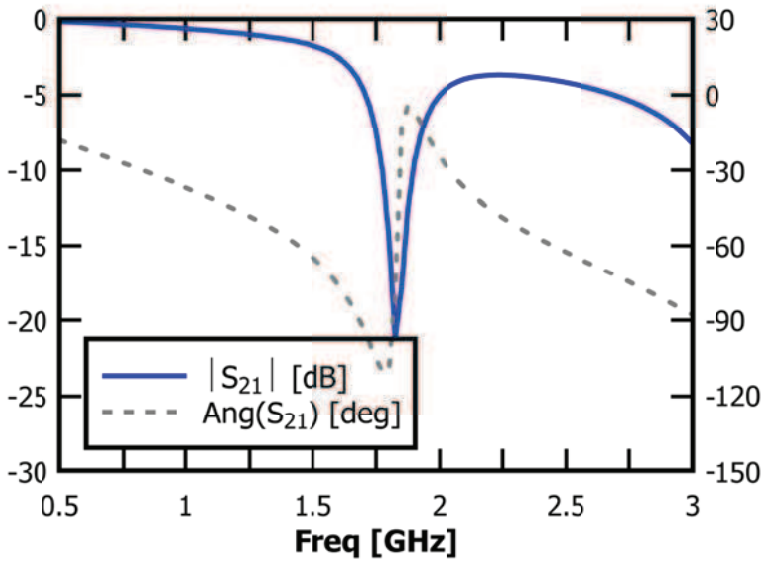

Figure 3-12: Transmission coefficient S_{21} of the MSRR. The resonance frequency is 1.825GHz.

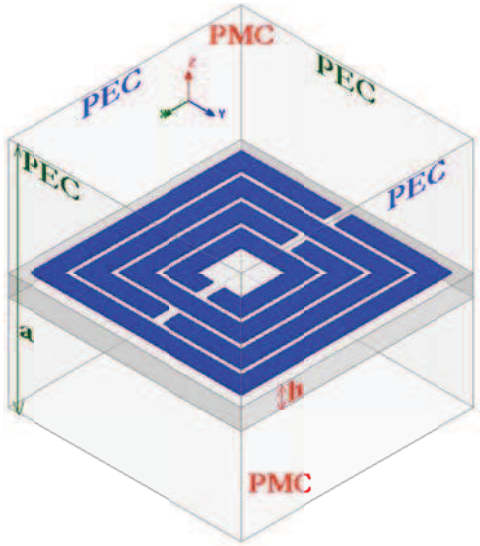

Figure 3-13: 3D view of MSRR structure simulated in HFSS Eigen Solver. Inclusion dimensions are: a=11mm, l_{ext}=10mm, "w" & "s" are variables, g=0.5mm, substrate thickness h=1mm, material used FR4. Boundary conditions are PMC for the top & bottom faces, PEC are used for the other faces

It is clear from the results that the resonance frequency of the MSRR varies with "w" and "s" directly. For a fixed spacing "s", the resonance frequency increased as "w" increased. These

phenomena can be understood by the decreased value of the ring inductance, where the resonance frequency of the MSRR is inversely proportional to the ring inductance L.

Note that, for practical reasons, the width "w" of the rings is limited to 400μm when "s" is larger than 750μm. If the width becomes wider, the four rings can not fill the unit cell.

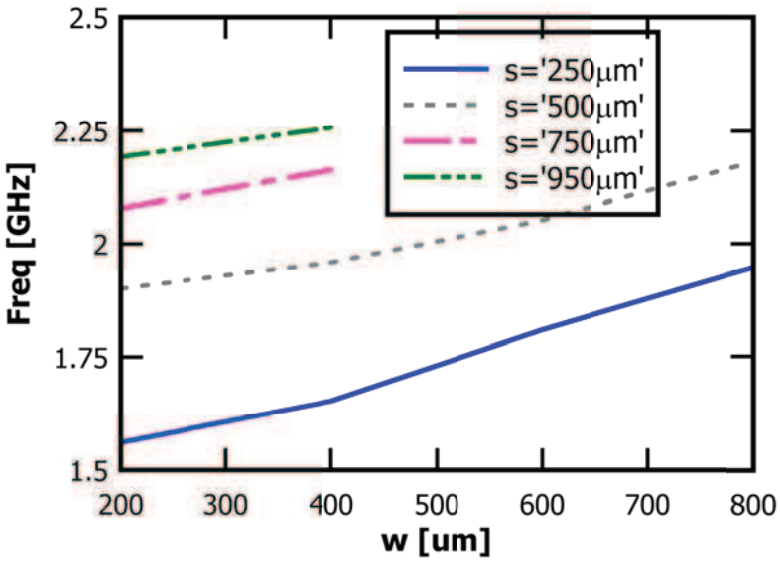

Figure 3-14: frequency variation as a function of both "w" and "s" for a fixed substrate thickness h= 1mm

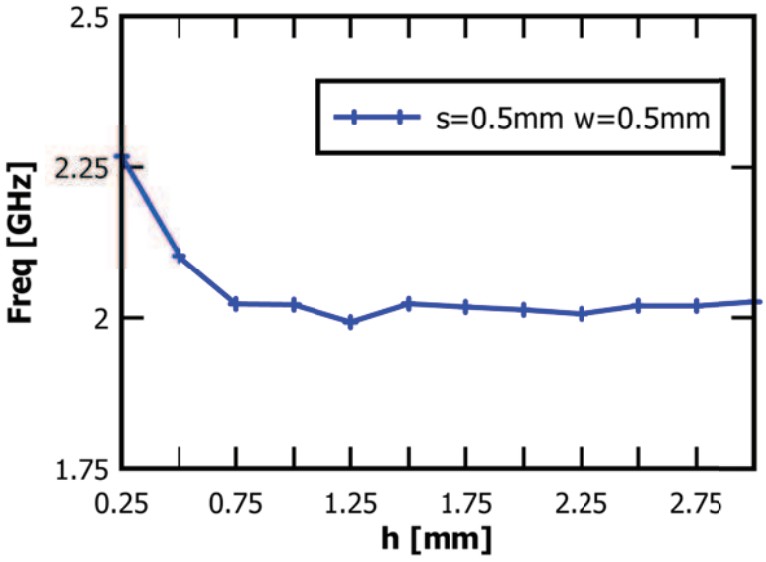

Figure 3-15: frequency variation as a function of substrate thickness "h" for a fixed "w" and "s" of 0.5mm

Again the variation of the unit cell MSRR resonance frequency, as a function of the substrate thickness "h", is shown in Figure 3-15. The result shows the resonance frequency will

saturates after h= 1mm thickness. We conclude that the dominant variation of frequency is related to "w" and "s" respectively.

3.3 Electromagnetic Behavior of the Sub-wavelength Resonators

This section will describe the models of polarizability of SRR and for the composite negative magnetic permeability media (NMPM) and left-handed media (LHM) Metamaterials based on this particle.

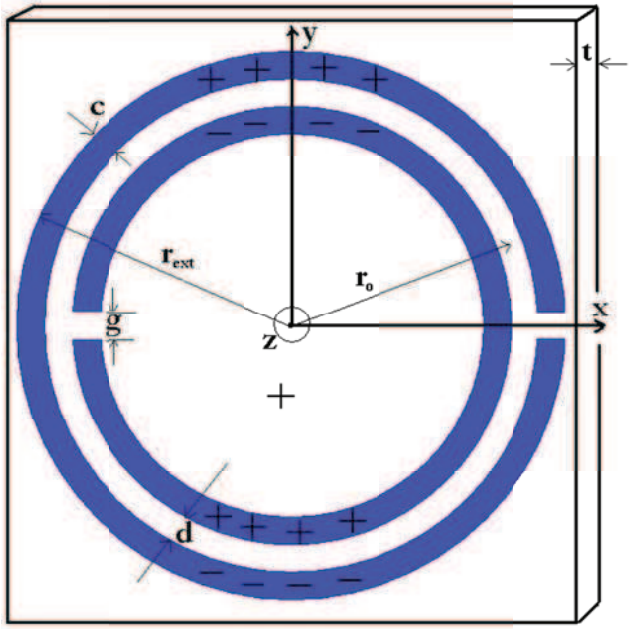

Figure 3-16: Edge coupled SRR (EC_SRR)

The SRR cell to be analyzed is shown in Figure 3-16. Two similar split rings are coupled by means of a strong distributed capacitance in the region between the rings (the slits are meaningfully wider than the distance between the rings, "d" and "t", respectively). When a time-harmonic external (or local) magnetic field of angular frequency ω is applied along the axis of these structures, an electromotive force will appear around the SRRs.

Provided that the electrical size of the SRR can be considered small, a quasistatic behavior is expected. With this quasistatic model in mind, it is not difficult to see how the induced current lines will pass from one ring to the other through the capacitive gaps between them in the form of field displacement current lines (the current lines can be viewed as tracing almost circular trips). Therefore, the total current intensity flowing on both rings remains the same for any cross section of the structure (i.e., it is independent of the angular polar coordinate).

3.3.1 SRR Equivalent Circuit: Baena's Analytical Model [3-4]

The whole device then behaves as an LC circuit driven by an external electromotive force. The total capacitance of this LC circuit will be the series capacitance of the upper and the lower halves (with respect the line containing the ring gaps) of the SRR and the resonance frequency is given by:

$$\omega_0 = \frac{1}{\sqrt{\frac{2}{\pi r_0 L C_{pul}}}} \tag{3-12}$$

where C_{pul} is the per unit length (p.u.l.) capacitance between the rings, L is the total inductance of the SRR, and r_0 is the average radius of the considered SRR.

The polarizability equations for the SRR are given as follows:

$$\boldsymbol{m_z = \alpha_{zz}^{mm} B_z^{ext} - j\alpha_{yz}^{em} E_y^{ext}} \tag{3-13}$$

$$\boldsymbol{p_y = \left(\alpha_{yy}^{ee} + \alpha_{yy}^{\prime ee}\right) E_x^{ext} + j\alpha_{yz}^{em} B_z^{ext}} \tag{3-14}$$

$$\boldsymbol{p_x = \alpha_{xx}^{ee} E_x^{ext}} \tag{3-15}$$

where $\mathbf{m}$ and $\mathbf{p}$ are the magnetic and electric induced dipoles, B^{ext} and E^{ext} the external fields and $\boldsymbol{\alpha}$ the polarizabilities, which are found to be [3-18]:

$$\boldsymbol{\alpha_{zz}^{mm} = \alpha_0 \left(\frac{\omega_0^2}{\omega^2} - 1\right)^{-1}, \alpha_0 = \frac{\pi^2 r_0^4}{L}} \tag{3-16}$$

$$\boldsymbol{\alpha_{xx}^{ee} = \alpha_{yy}^{ee} = \varepsilon_0 \frac{16 r_{ext}^4}{3}} \tag{3-17}$$

$$\boldsymbol{\alpha_{yz}^{em} = 2\omega_0 \pi r_0^2 d_{eff} C_{0,pul} \frac{\omega}{\omega_0} \left(\frac{\omega_0^2}{\omega^2} - 1\right)^{-1}} \tag{3-18}$$

$$\boldsymbol{\alpha_{yy}^{\prime ee} = 4\omega_0^2 r_0^2 \left(d_{eff} C_{0,pul}\right)^2 L \left(\frac{\omega_0^2}{\omega^2} - 1\right)^{-1}} \tag{3-19}$$

with d_{eff}=c+d and $C_{0,pul}$ being the p.u.l. capacitance between the rings when the dielectric slab is removed. The subscripts stand for Cartesian components and superscripts for magnetic/magnetic (mm), electric/electric (ee) or electric/magnetic (em) interaction between the particle and the external field.

Ohmic losses can be approximately incorporated to the model by means of an effective resistance of the rings R that can be introduced as an imaginary part of the total inductance L thus, giving the following complex inductance:

$$\hat{L} = L + \frac{R}{j\omega} \tag{3-20}$$

which substitutes L to in the above expressions for the polarizabilities.

The computation of the SRR polarizabilities using the above expressions requires the evaluation of L, C_{pul}, $C_{0,pul}$. Assuming that the ring curvature has negligible effect, several methods for computing the p.u.l. capacitance between the rings the SRR can be found. The tables in [3-19] provide design formulas for the phase constant β and the impedance Z of a microstrip transmission line and a pair of coupled metallic strips on a dielectric substrate, respectively.

The capacitances C_{pul} of these structures are obtained from the well-known expression: $C_{pul}=\beta/(\omega Z)$ [3-19]. Once they are obtained, the p.u.l. capacitance of the pair of coupled strips directly gives the C_{pul} of the SRR. The proposed method of computation is fast and, as was aforementioned, gives enough accuracy in the frame of the present model.

However, better results could be obtained by using more specific methods which can take into account the effects of curvature. Nevertheless, this improvement only would have sense if other aspects of the model, such as the computation of the ring inductance, are improved too.

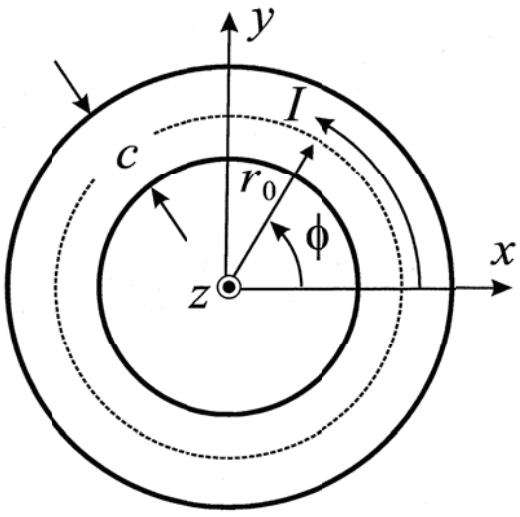

Figure 3-17: Equivalent single ring model for computing L of SRR. Adapted from [3-9]

The computation of the total inductance of the SRR is not so straightforward, although an appropriate approximation can provide a considerable simplification while keeping reasonable accuracy. According to the previous assumptions on the behavior of the line currents along the SRR, it can be assumed that the total inductance of both SRR can be approximated by the inductance of a single equivalent ring whose average radius is the average radius of the considered SRR and width equal to the width of each original ring (see Figure 3-17).

The inductance can be then computed making use of the variational expression $L=2U_M/I^2$, where U_M is the magnetostatic energy for the total current intensity supported *I* by the ring. Solving for the magnetostatic potential in the Fourier-Bessel domain, and after some algebraic manipulations, it is finally obtained that:

$$\boldsymbol{L = \frac{\mu_0 \pi^2}{I^2} \int_0^\infty [\tilde{I}(k)]^2 k^2 dk} \qquad \textbf{(3-21)}$$

Where $\tilde{I}(k)$ is the Fourier-Bessel transform of the current function on the ring, $I(r)$ defined by:

$$\boldsymbol{I(r) = \int_r^\infty J_{s,\phi}(r')dr'} \qquad \textbf{(3-22)}$$

with being the azimuthal surface current density on the ring. For practical computations it has been assumed a constant value for on the ring, that is,

$$\boldsymbol{J_{s,\phi} = \begin{cases} \frac{I}{c} & for \;\; r_0 - \frac{c}{2} < r < r_0 + \frac{c}{2} \\ 0 \;\; otherwise \end{cases}} \qquad \textbf{(3-23)}$$

This approximation gives a reasonable approximation for L. In this case, the Fourier-Bessel transform, $\tilde{I}(k)$, is analytically obtained in terms of the Struve and Bessel functions and the integration in L is carried out numerically. A better approximation could be obtained if a more accurate description for (multiple basis functions) had been employed. Nevertheless, this numerical improvement is not expected to enhance substantially the quality of the approach since other approximations are already involved in the theory.

Finally, as aforementioned, ohmic losses are introduced in the model by means of the effective resistance, R, of the SRR. This effective resistance is obtained by using the equivalent

ring model for the current distribution on the SRR. If a constant is assumed on the ring of Figure 3-17, the resistance can be approximated as:

$$R = \begin{cases} \dfrac{2\pi r_0}{ch\sigma}, & if \quad \dfrac{h}{2} < \delta \\ \dfrac{\pi r_0}{c\delta\sigma}, & otherwise \end{cases} \tag{3-24}$$

where **δ** is the skin depth and **h** and **σ** the thickness and conductivity of the metallization, respectively.

Once the SRR polarizabilities have been obtained in a self-consistent way, they can be used in a local field theory in order to determine the macroscopic constitutive parameters of media consisting of a regular array of SRRs. This local field theory makes use of the well-known Lorentz theory and directly applies to any SRR-based NMPM. It can be also applied to the analysis of discrete LHM made by the superposition of artificial plasma and a SRR-based NMPM. In this latter application, it will be implicitly assumed that the constitutive parameters of the LHM media are the superposition of those of the artificial plasma and the NMPM.

The application of the proposed theory to discrete LHM would account for the artificial plasma by simply introducing an additional effective dielectric susceptibility χ_{eff} (which may be tensorial for anisotropic artificial plasmas).

For 2-D artificial plasma made of a regular array of parallel metallic plates separated a distance "*a*", and for electric field polarization and wave propagation both parallel to the plates χ_{eff}, is given by:

$$\chi_{eff} = -\left(\frac{\omega_0}{\omega}\right)^2 \tag{3-25}$$

where ω_0 plays the role of an effective plasma frequency, which coincides with the cutoff frequency of the parallel-plate waveguides: $\omega_0 = \pi\left(a\sqrt{\varepsilon_0\mu_0}\right)^{-1}$. For 2-D and 3-D arrays of wires, the expressions for χ_{eff} and ω_0 may become more complicated.

3.3.2 SRR Equivalent Circuit: Saha's and Shamonine's Analytical Approach

3.3.2.1 First Approach

Different approaches to model the circuit of split ring resonators are demonstrated by several authors. In addition to the equivalent circuit of MSRR, two approaches are presented to visualize the equivalent circuit of SRR. First we start by the work of C. Saha [3-21] who

presented theoretical formulations to estimate the resonant frequency and magnetic polarizability of SRR.

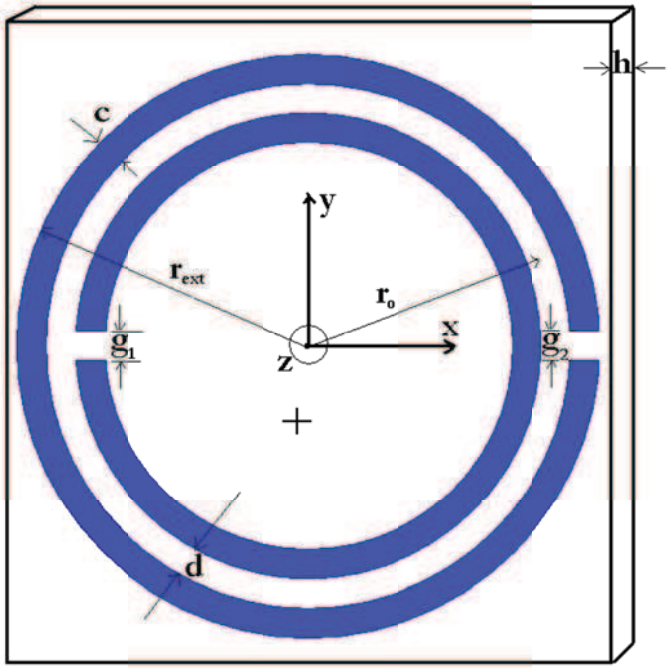

Figure 3-18: SRR schematic of line width "*c*" having radii r_0 and r_{ext} with inter ring spacing "d" and split gap dimensions, $g_1 = g_2$, printed on a dielectric substrate having thickness, "h" and dielectric constant ε_r

3.3.2.1.1 Resonance Frequency

Figure 3-18 shows the schematic diagram of a circular SRR and its equivalent circuit model is shown in Figure 3-19.

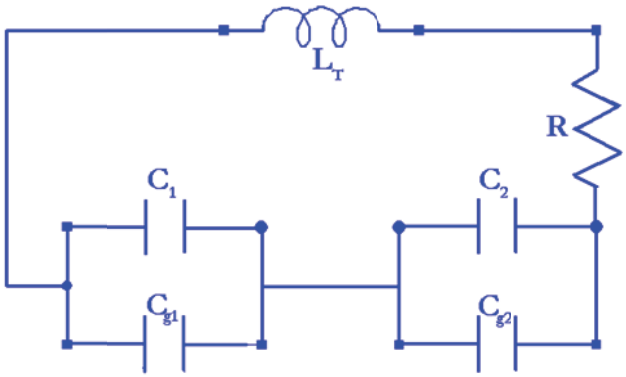

Figure 3-19: Equivalent circuit model of the circular SRR

Application of an external magnetic field along the z-axis of the SRR induces an electromotive force around the SRR with induced currents passing from one ring to the other

through the inter ring spacing, d and the structure behaves as a LC circuit. As shown in the equivalent circuit in Figure 3-19, the metallic rings contribute a total inductance, L_T and distributed capacitances C_1 and C_2 forming at the two halves of the SRR structure above and below the split gaps. This new equivalent circuit also incorporates the gap capacitances, C_{g1} and C_{g2} formed due to the split within the inner and outer rings, respectively.

The resonant frequency ω_0 of the circular SRR, thus is given by:

$$\boldsymbol{\omega_0 = \sqrt{\frac{1}{L_T C_{eq}}}} \tag{3-26}$$

where, C_{eq} is the total equivalent capacitance of the structure.

Again, from the equivalent circuit of Figure 3-19, the total equivalent capacitance, C_{eq} can be evaluated as:

$$\boldsymbol{C_{eq} = \frac{(C_1 + C_{g1})(C_2 + C_{g2})}{(C_1 + C_{g1}) + (C_2 + C_{g2})}} \tag{3-27}$$

As the split gaps are of identical dimensions $g_1 = g_2 = g$, hence the gap capacitances $C_{g1} = C_{g2} = C_g$ and the series capacitances $C_1 = C_2 = C_0$ and therefore (3-35) is modified as:

$$\boldsymbol{C_{eq} = \frac{(C_0 + C_g)}{2}} \tag{3-28}$$

Considering a metal thickness, t of the strip conductors, the gap capacitances C_{g1} and C_{g2} can be represented as:

$$\boldsymbol{C_{g1} = C_{g2} = C_g = \frac{\varepsilon_0 c t}{g}} \tag{3-29}$$

where, c and t are the width and thickness of the metallic rings, respectively and ε_0 is the free space permittivity. The distributed capacitances C_1 and C_2 are also a function of the split gap dimensions $g_1 = g_2 = g$ and the average ring radius r_{avg} and is given as:

$$\boldsymbol{C_0 = C_1 = C_2 = (\pi r_{avg} - g) C_{pul}} \tag{3-30}$$

$$\boldsymbol{r_{avg} = r_{ext} - c - \frac{d}{2}} \tag{3-31}$$

and C_{pul} is the capacitance per unit length and is calculated as:

$$\mathbf{C_{pul}} = \sqrt{\boldsymbol{\varepsilon_e}}/\boldsymbol{C_0 Z_0} \quad \textbf{(3-32)}$$

where $c_0 = 3\times10^8$ m/s is the velocity of light in free space, ε_e is the effective permittivity of the medium and Z_0 is the characteristic impedance of the line.

The characteristic impedance Z_0 is given as:

$$\boldsymbol{Z_0} = \frac{\mathbf{120\pi}}{\sqrt{\boldsymbol{\varepsilon_e}}}\frac{\boldsymbol{K(k)}}{\boldsymbol{K(k')}} \quad \textbf{(3-33)}$$

K(k) is a complete elliptic function of the first kind and K(k') is its complimentary function. The final expression of C_{eq} is given as follows:

$$\boldsymbol{C_{eq}} = \frac{(\boldsymbol{\pi r_{avg} - g})\boldsymbol{C_{pul}}}{\mathbf{2}}\frac{\boldsymbol{\varepsilon_0 ct}}{\mathbf{2g}} \quad \textbf{(3-34)}$$

A simplified formulation for the evaluation for the total equivalent inductance L_T for a wire of rectangular cross section having finite length *l* and thickness *c* is proposed as [3-22]:

$$\boldsymbol{L_{SRR}} = \mathbf{0.0002}\boldsymbol{l}\left[\mathbf{2.303}\times\boldsymbol{log_{10}}\left(\frac{\mathbf{4}\boldsymbol{l}}{\boldsymbol{c}}\right) - \boldsymbol{\gamma}\right]\times\mathbf{10^{-3}}\boldsymbol{H} \quad \textbf{(3-35)}$$

where, the constant $\gamma = 2.451$ for a wire loop of circular geometry. The length "l" and thickness "c" are in mm. The evaluation of the wire length l is straight forward as:

$$\boldsymbol{l} = \mathbf{2}\boldsymbol{\pi r_{ext}} - \boldsymbol{g} \quad \textbf{(3-36)}$$

For close proximity wires at high frequencies, the current is confined to the wire surfaces and effectively reduces the spacing between them [3-23]. The finite length "l" is calculated considering a single loop with r_{ext} as the radius. The mutual inductance hence has been ignored.

3.3.2.1.2 Numerical Application

By employing the equations of L & C presented in the previous paragraph, the dimensions of the SRR are selected to have a resonance at 2.4 GHz (see Figure 3-20). These equations are introduced in a Mathcad sheet added to appendix D at the end of the manuscript.

In order to validate the desired resonance of the SRR electromagnetically, a simulation on HFSS is accomplished on a waveguide having a cutoff frequency λ_{cutoff} less than 2 GHz (WG_R23) and containing an SRR cell shown in the Figure 3-20(a). The electric field $\vec{E}$ is polarized in parallel to the gap (parallel to y-axis) of the outer ring as displayed on Figure 3-20(b);

whereas its mode of excitation is the fundamental mode TE_{01}. On the other hand, the magnetic field $\vec{H}$ is considered perpendicular to the plane of the rings.

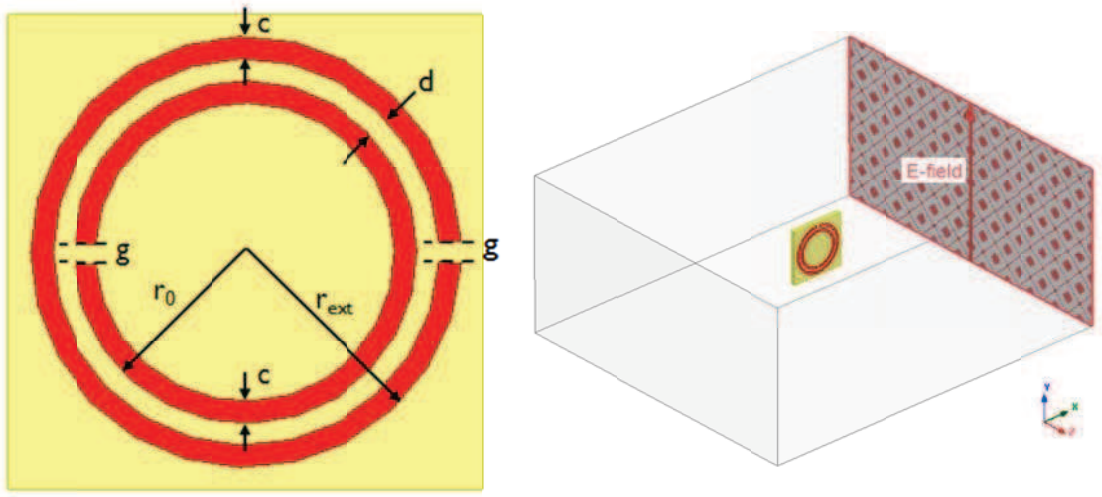

(a) **(b)**

Figure 3-20: (a) Schematic view of a circular SRR (r_{ext}=5mm, r_0=4mm, g=0.5mm, c=0.5mm, & d=0.5mm); (b) 3D view of the waveguide including the SRR unit cell

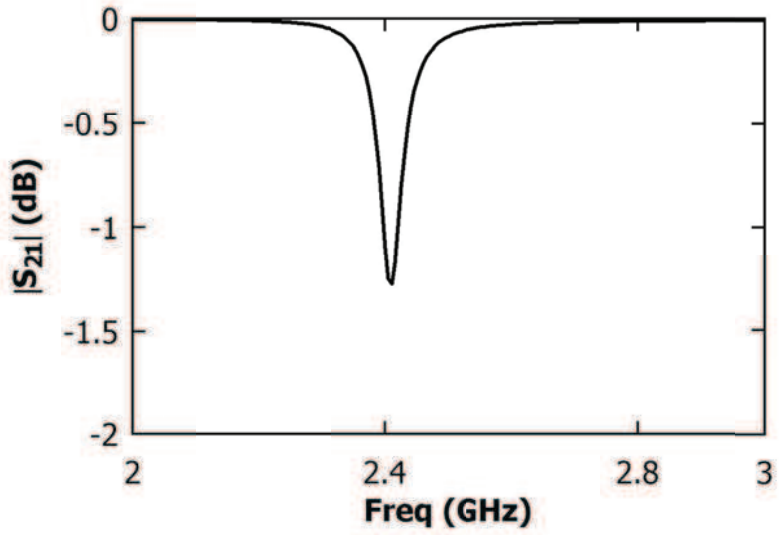

Figure 3-21: Insertion loss response obtained after simulation

Figure 3-21 shows the transmission dip obtained as a result of simulating the SRR shown in Figure 3-20. One can notice that this result is in good agreement with the resonance frequency calculated by using the analytical equations of L & C.

This numerical application validates this approach and opens a way to select the appropriate dimensions that suit our desired resonance frequency in order to add the inclusion to any structure in order to be optimized without wasting time on tuning the dimensions of the SRR.

3.3.2.2 Second Approach

The second approach presented in this context is applied by [3-24]. That is, a set of differential equations describing the current and voltage distribution in a split-ring resonator is derived and solved analytically. The resonant frequencies may be obtained from the solution of a characteristic equation.

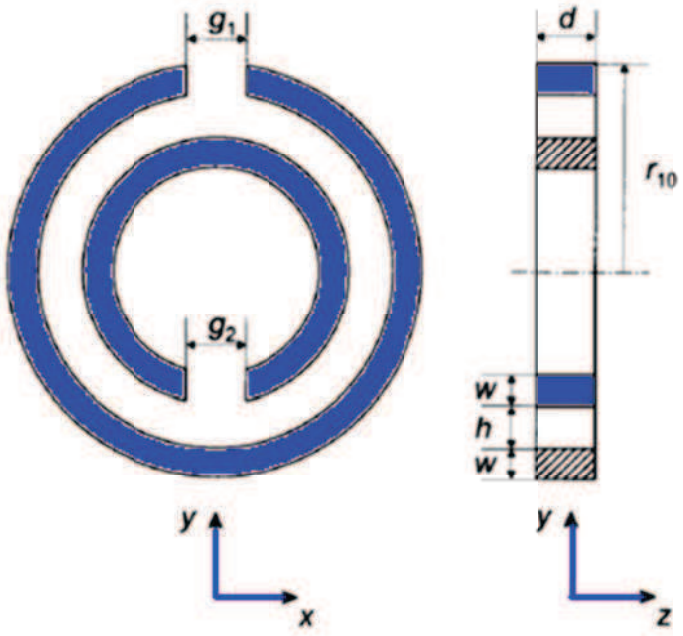

Figure 3-22: Schematic of the studied SRR

The element most often used in experiments is the split ring resonator (SRR) shown schematically in Figure 3-22. When excited by a time-varying magnetic field, it exhibits resonance at a set of frequencies of which the lowest is the most significant for the design of Metamaterials. The SRR is regarded as made up by distributed circuits joined together by the two gap capacitances, as shown in Figure 3-23.

The distributed circuit is similar to that used in transmission-line theory, with the difference that there are now inductances in both lines with a mutual inductance between them, and the excitation is represented by distributed voltages. It would be easy to include resistances as well, but for the sake of simplicity, here we treat only the lossless case.

The method of the solution follows traditional lines. Kirchhoff's equations applied to a $d\varphi$ element of the distributed circuit yields the following set of differential equations:

$$-\frac{\partial V}{\partial \varphi} = I_1 j\omega(L_1 - L_{12}) - I_2 j\omega(L_2 - L_{12}) + G_2 - G_1 \quad \textbf{(3-37)}$$

$$-\frac{\partial I_1}{\partial \varphi} = -j\omega CV, -\frac{\partial I_2}{\partial \varphi} = -j\omega CV \quad \textbf{(3-38)}$$

where ω is the angular frequency, V is the inter-ring voltage, I_1 and I_2 are the respective currents in the outer and inner rings, G_1 and G_2 are the induced voltages, C is the inter-ring capacitance, L_1 and L_2 are the respective inductances of rings 1 and 2, and L_{12} is the mutual inductance between them.

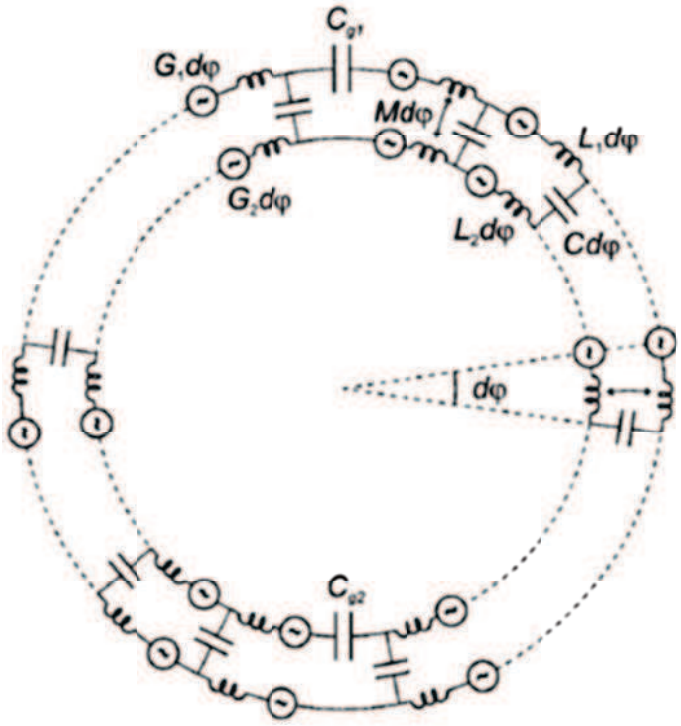

Figure 3-23: Equivalent circuit of the SRR

The differential equations are of a constant coefficient, which can be easily solved subject to the above conditions in terms of trigonometric functions. The resonant frequencies may then be obtained as the roots of a characteristic equation. Several calculations are presented to compare the resonant frequency of the proposed model with those obtained from electromagnetic simulations. As given by the author, the results are of good accuracy.

3.3.3 SRR Magnetic Polarizability

Magnetic polarizability of the SRR is a measurement of magnetic response of the SRR in which a magnetic resonance occurs when a magnetic field vertical to SRR plane is incident (along Z-axis), shown in Figure 3-24. The response of the SRR element to incident EM wave is crucial for metamaterial application. Around the resonant frequency, the dominant effect in the SRR structure is the magnetic polarizability, which gives rise to a strong diamagnetic behavior near and above the SRR resonance [3-9] and [3-18].

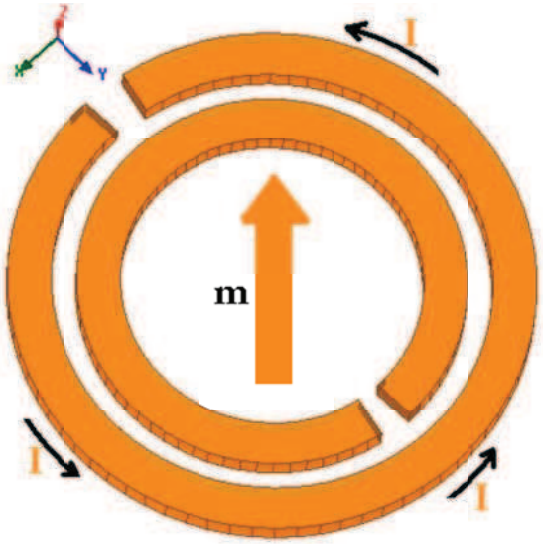

Figure 3-24: SRR Magnetic dipoles

Neglecting the effect of cross-polarization, which results in a bianisotropic behavior of using this structure, the experimental determination of the magnetic polarizability α_{zz}^{mm}, in [3-18] have been simulated using an EM simulator to determine the resonant frequency, ω_0 and the magnetic polarizability constant α_0 where:

$$\alpha_{zz}^{mm} = \alpha_0\left(\frac{\omega_0^2}{\omega^2} - 1\right)^{-1} \tag{3-39}$$

$$\alpha_0 = \frac{\pi^2 r_{avg}^4}{L_T} \tag{3-40}$$

Here L_T is the total equivalent inductance and r_{avg} is the average radius in mm.

3.4 Bianisotropy

3.4.1 Role of Bianisotropy

We have mentioned before that the polarizability equations for the SRR are given as follows:

$$\boldsymbol{m_z = \alpha_{zz}^{mm} B_z^{ext} - j\alpha_{yz}^{em} E_y^{ext}} \quad \textbf{(3-41)}$$

$$\boldsymbol{p_y = \left(\alpha_{yy}^{ee} + \alpha_{yy}^{\prime ee}\right) E_x^{ext} + j\alpha_{yz}^{em} B_z^{ext}} \quad \textbf{(3-42)}$$

$$\boldsymbol{p_x = \alpha_{xx}^{ee} E_x^{ext}} \quad \textbf{(3-43)}$$

From these equations, which clearly shows the bianisotropic behavior of the particle, it should be possible to obtain the macroscopic susceptances of an effective continuous medium consisting of a random or periodic arrangement of these particles. The suitability of such a homogenization procedure will be mainly limited by the electrical size of the unit cell. There exists wide experimental evidence of an appropriate homogenization procedure that provides a good description of the main features of the electromagnetic behavior of left-handed and/or bi(iso/aniso)tropic Metamaterials, provided that the size of the unit cell is smaller than approximately one-tenth of the free space wavelength.

Losses can also play an important role in the homogenization procedures, but the numerical simulations show that, for the particular SRR analyzed here, the main experimental results can be accounted for by neglecting losses in the analysis of the artificial atoms. Furthermore, they could be easily incorporated in the proposed model by simply adding a frequency-dependent imaginary part $-iR/\omega$ to the inductance L (accounting for the series resistance R of the metallic strips) and an imaginary part $i\omega G$ to the p.u.l. capacitance C (accounting for the p.u.l. shunt conductance G across the slot between the rings).

3.4.2 Consequences of Bianisotropy

In order to evaluate the physical implications of the bianisotropic nature of the SRR particle, both the anisotropic NMPM and a two dimensional left-handed medium LHM have been analyzed. The first medium consists of a number of identical SRR particles printed on a dielectric slab (relative dielectric permittivity "ε_r"and thickness "t") and arranged in a cubic lattice with spacing "a". See Figure 3-25.

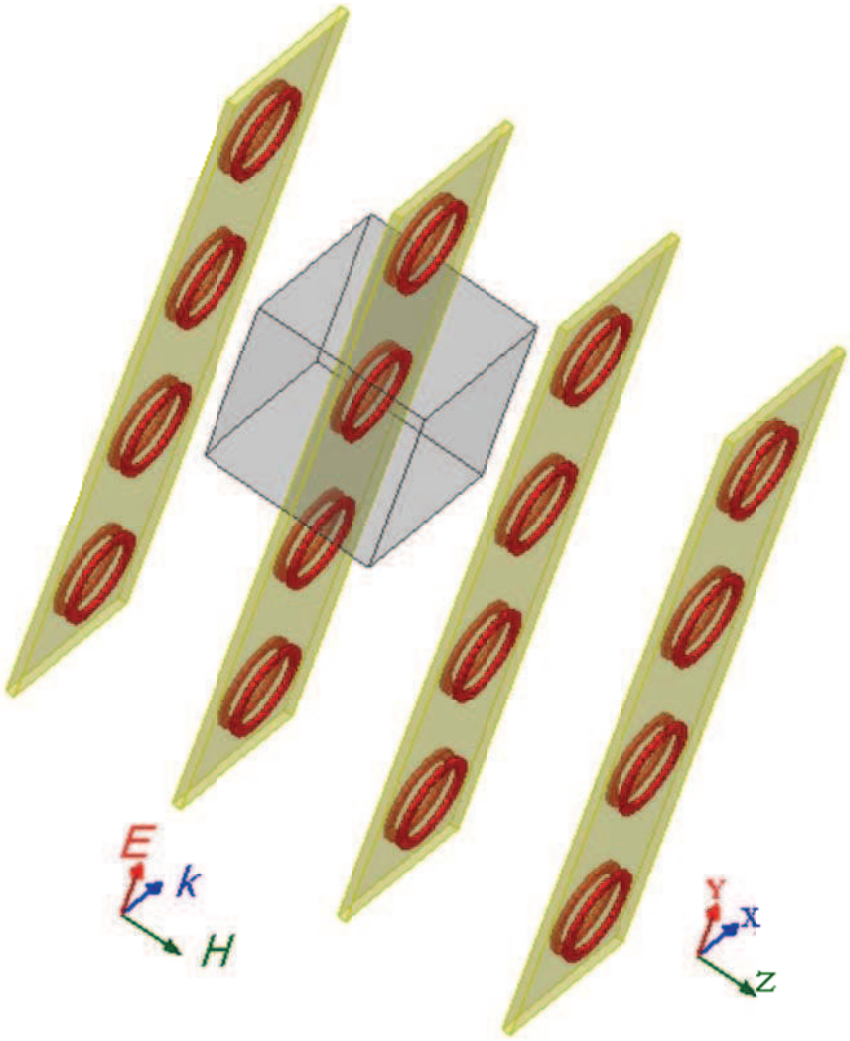

Figure 3-25: SRR particles printed on a dielectric slab (relative dielectric permittivity "ε", and thickness "t") and arranged in a cubic lattice with spacing *a*

The left-handed material is formed by placing between the SRR particles of the medium wires of (equivalent) infinite length, which are parallel to the y-axis of these particles. The wire medium behaves as anisotropic plasma, with $\epsilon_{yy} = \epsilon_0(1 - \omega_p^2/\omega^2)$, ω_p being the plasma frequency. Neglecting losses and taking into account the constraints imposed by the reciprocity theorem, the constitutive relations for these media can be written as:

$$\boldsymbol{D} = \boldsymbol{\epsilon}\mathbf{E} + (\boldsymbol{\chi} - \mathbf{j}\boldsymbol{k})\sqrt{\boldsymbol{\epsilon_0}\mu_0}\boldsymbol{H} \tag{3-44}$$

$$\boldsymbol{B} = (\boldsymbol{\chi} + \mathbf{j}\boldsymbol{k})\sqrt{\boldsymbol{\epsilon_0}\mu_0}\boldsymbol{E} + \mu\boldsymbol{H} \tag{3-45}$$

where, accordingly to (3-41)–(3-43), only χ_{eyy}, χ_{exx}, $\varkappa_{yz}$, and χ_{mzz} are different from zero. When losses are neglected all these quantities are real numbers. It can be easily realized that plane transverse electromagnetic TEM waves can propagate along the x-axis in an homogeneous

medium described by the constitutive relations (3-44) and (3-45) (with the aforementioned restrictions), provided that E and H are polarized along the y and z axes of the SRR's, respectively. The wave number of these TEM plane waves is given by:

$$\kappa_x = \omega\sqrt{\mu_{zz}\epsilon_{yy} - \mu_0\epsilon_0\kappa_{yz}^2} \tag{3-46}$$

Note that a very important consequence of (3-46) is the existence of a forbidden band at those frequencies satisfying:

$$\mu_{zz}\epsilon_{yy} - \mu_0\epsilon_0\kappa_{yz}^2 > 0 \tag{3-47}$$

while transmission is possible for:

$$\mu_{zz}\epsilon_{yy} - \mu_0\epsilon_0\kappa_{yz}^2 < 0 \tag{3-48}$$

Using (3-46) for the TEM wave number instead of the simplified equation $\kappa_x = \omega\sqrt{\mu_{zz}\epsilon_{yy}}$ leads to quantitatively different results, but also to a meaningfully different qualitative behavior. Assuming that the NMPM has a positive dielectric constant (> 0) in the whole frequency range of interest, assuming that the composite SRR and wire medium (i.e., the left-handed material) has a negative dielectric constant at the same frequencies ($\epsilon_{yy}^{LH} < 0$), and assuming that the magnetic properties of both media are identical ($\mu_{yy}^{NMPM} = \mu_{zz}^{LH}$ and $\kappa_{yy}^{NMPM} = \kappa_{zz}^{LH}$), the simplified relation $\kappa_x = \omega\sqrt{\mu_{zz}\epsilon_{yy}}$, which neglects bianisotropy i.e., the magnetoelectric coupling in the SRR predicts a forbidden band for the NMPM which exactly coincides with the transmission band for the left-handed material.

When numerical simulations are carried out for the same structure and for plane waves propagating in the same direction, but with the electric field polarized along the *x* axis of the SRR particle, the rejection band of the NMPM and the transmission band of the left-handed material exactly coincide. This result can be interpreted by taking into account that the cross polarization α_{xz}^{em} vanishes in the SRR particle and, therefore, the coupling parameter κ_{xz} must vanish in the corresponding effective medium. We can thus conclude that the presence of bianisotropy provides an explanation of some unexplained qualitative results of the numerical simulations and experiments.

The electromagnetic behavior of artificial bianisotropic media, NMPM, and left-handed Metamaterials, made with resonant metallic inclusions in host uniform medium, present noticeable similarities. In particular, the bianisotropic characteristics of recently reported NMPM

and left-handed Metamaterials have been investigated. An analytical model, accounting for magnetoelectric coupling, has been proposed for the SRR, which is the elementary atom of the aforementioned NMPM and left-handed Metamaterials. That coupling is responsible for the bianisotropic behavior of the equivalent continuous medium consisting of an aggregate of those particles. Considering bianisotropy, some up-to-date unexplained features of the electromagnetic waves propagating through those media can be explained. In particular, the transmission and forbidden frequency bands for those materials can be more adequately described accounting for bianisotropy.

3.4.3 MSRR and SR Bianisotropic Behavior Investigation

This study is devoted to compare the performances of the multi split-ring resonator (MSRR) and the spiral resonator (SR). The two structures, shown in Figure 3-26, have the same outer dimensions but they differ in the filling ratio. The boundary conditions (PEC & PMC) in addition to the polarizations of the electric and magnetic fields (E & H) are also shown on the same figure.

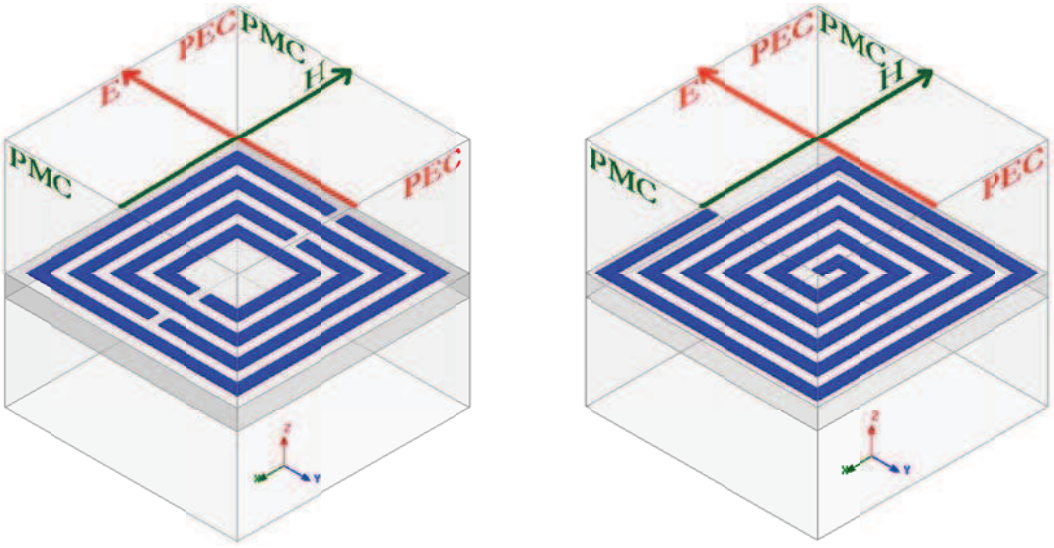

(a) **(b)**

Figure 3-26: 3D setup for bianisotropic behavior (a) MSRR boundary conditions (b) SR boundary conditions

The selected resonator is devoted to an application that requires that E & H being in parallel to the plane of the rings; this is well indicated in the 3D views (see Figure 3-26) of the structures prepared to be simulated in HFSS. For this reason, the selected resonator should give a resonance by applying this configuration.

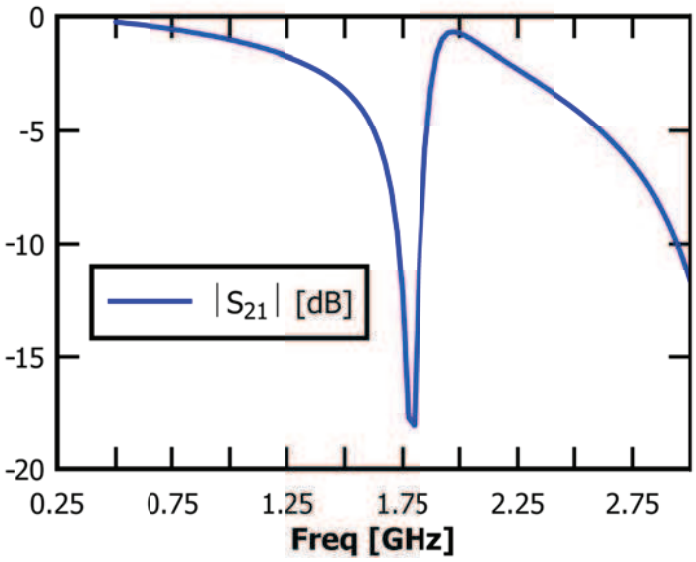

Figure 3-27: Transmission coefficient response S_{21} for the MSRR

The transmission coefficient obtained from simulating the MSRR is depicted on Figure 3-27. One can remark the resonance at 1.75 GHz whereas no resonance is achieved from the simulation of the SR as appears from the response of S21 parameter presented in Figure 3-28.

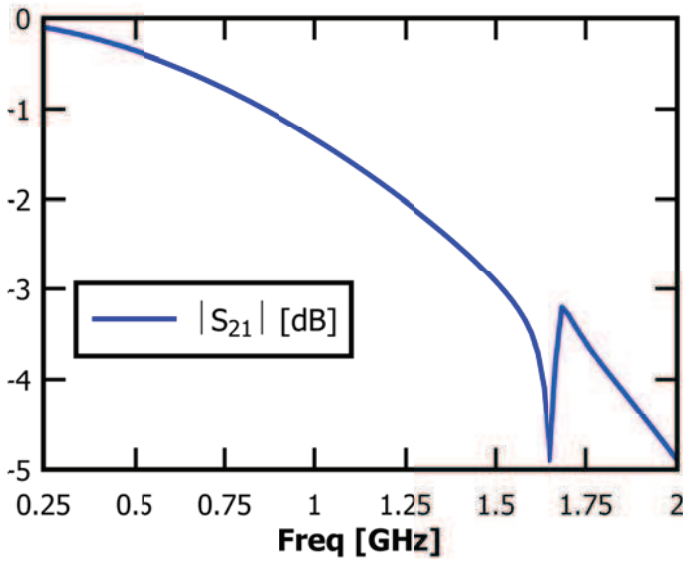

Figure 3-28: Transmission coefficient response S_{21} for the SR

Despite that the resonance of the MSRR is higher than that of the SR, this latter is discarded and the MSRR is selected for the proposed application (AMC plane in the next paragraph) because of its bi-anisotropic behavior.

3.5 Low Profile Antenna AMC-Based Surface

The great revolution in wireless communications domain obligates the electrical engineers to create novel approaches

in order to cover the needs worldwide under several operating conditions. One of the most important challenges in this domain is the design of antenna structures and the improvement of its performance. This is related to the evolution in the functioning of numerical computational electromagnetic tools that improve the capability to build non-classical complex 3D structures and to visualize different results in an acceptable simulation time.

3.5.1 Artificial Magnetic Conductors (AMCs)

A flat metal sheet is used in many antennas as a reflector, or a ground plane [3-25]. Its presence improves the gain of the antenna by 3 dB. Unfortunately, a reduction in the radiation efficiency results if the antenna is too close to the conductive surface. This problem was usually solved by placing the antenna $\lambda/4$ apart from the metal sheet [3-26].

However, such distance affects the compactness and the size of the structure; a disadvantage in some applications where small sizes and low frequencies are required. Several researches have explored solutions to replace the metallic conductive surface with other sheets that perform the same task and permit to locate the antenna in close proximity.

Metamaterials structures are typically realized from periodic dielectric substrates and various metallization patterns [3-27], [3-28]. The reflection phase of these materials is defined as the phase of the reflected electric field at the reflecting surface. It is known that perfect electric conductors (PECs) have a 180º reflection phase for a normally incident plane wave, whereas it is 0º for Perfect Magnetic Conductors (PMCs) [3-29]. Since PMCs does not exist in nature, a special effort has been devoted to realize PMC-like surfaces [3-30]. Artificial Magnetic Conductors (AMCs), a special name of fabricated PMC, are designed from Metamaterials and proposed to replace the metallic conductive surface [3-26].

Antenna research area is interested in AMCs as they can replace PMCs for low profile antennas [3-31]. This is referred to the fact that, from a designing point of view, the overall height of the structure of these antennas is less than $\lambda/10$ [3-32]; a critical distance if a ground plane is implemented nearby. Different kinds of magnetic inclusions had been used in the synthesis of artificial materials and Metamaterials.

Split-Ring Resonators (SRRs) are proposed to achieve miniaturization at microwaves [3-33]. This type of resonators has a limitation at relative low frequency ranges and higher rates of miniaturization. Multiple Split-Ring Resonators (MSRRs) are proposed in order to increase the capacitance of a resonant magnetic inclusion while conserving the same outer dimensions of the resonator. This is due to the increasing number of inner split rings where more distributed capacitances between the rings are created and consequently a lower resonant frequency [3-8].

In fact, with the same outer dimension of a circular SRR, a square ring SRR has a lower resonant frequency due to its longer strip [3-8]. Figure 3-29 shows a comparison between the schematic diagrams of circular and rectangular MSRRs. Thus, for higher miniaturization rates, squared rings are used in the thesis work.

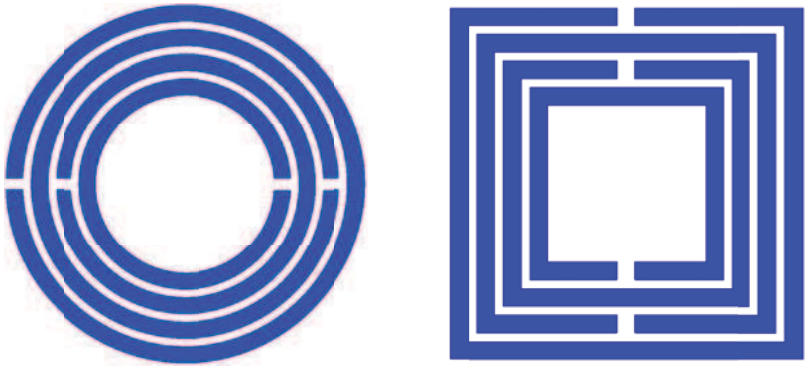

Figure 3-29: Schematic diagrams of circular and rectangular MSRRs

Moreover, a very low cost dielectric substrate (Epoxy FR4) is employed to print on the inclusions. This is one of the great features of MSRRs where a low permittivity material is used while conserving the same frequency achieved with higher permittivity values (ceramic as an example).

In this section of our manuscript, the reflection phase of a single rectangular MSRR is characterized. Then, the performance of an AMC surface, based on the proposed MSRR, is studied. The following paragraph presents the functioning of a low profile dipole antenna that is implemented nearby the AMC surface. The electromagnetic simulator that is employed to simulate all the structures shown in this paper is ANSOFT High Frequency Structure Simulator (HFSS) [3-34].

3.5.2 Characterization of MSRR-based AMC Surface Reflection

3.5.2.1 Rectangular MSRR Unit Cell Design

Figure 3-30(a) and Figure 3-30 (b) and show the basic structure of the proposed four rings MSRR and its equivalent circuit respectively. C_{12}, C_{23} and C_{34} are the distributed capacitances between adjacent rings. With respect to the vertical dashed line in Fig, the distributed capacitance between the first half of the two rings is in series with the one associated to the second half.

The unit cell is composed of four concentric split rings implemented on FR4 dielectric substrate with ε_r=4.4, loss tangent = 0.02 and thickness h = 3 mm. The printed metal is copper with 18μm thickness. The dimensions of the square MSRR are depicted on the schematic of Figure 3-30(b). Their numerical values are as follows: g = 0.35mm, s = 0.25mm, w = 0.5mm, L= 11mm & unit cell size a = 11.25 mm.

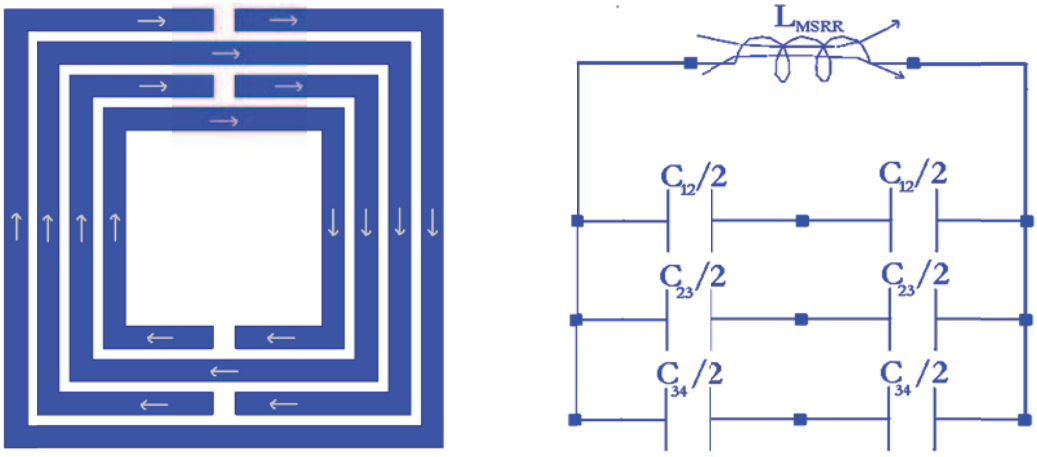

(a) **(b)**

Figure 3-30: Current flow and the circuit model of MSRR

The model designed on HFSS to calculate the reflection phase characteristics of the proposed MSRR is shown in Figure 3-31. The scattering parameters are obtained by simulating a single port waveguide with two parallel perfect electric conductors (PECs) in the yz-plane and two perfect magnetic conductors (PMCs) in the xy-plane. The magnetic field vector (H) of the incident plane wave is usually considered normal to the rings surface [3-36].

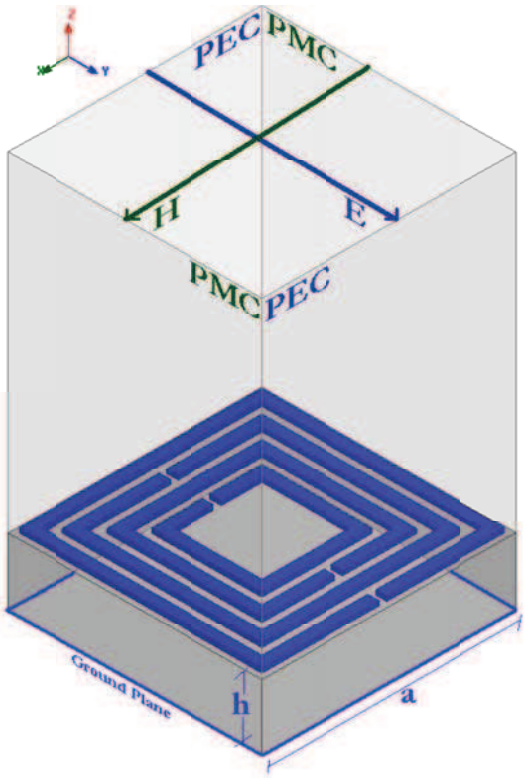

Figure 3-31: HFSS model for MSRR reflection characterization

However, in the work of this thesis, the MSRR is fed in a manner where (H) is parallel to the surface (y-axis direction). That is, the propagating plane wave is polarized parallel to the PMC walls and normal to the PEC walls.

The use of parallel-plate waveguide gives the capability simulate infinite number of unit cells that are implemented periodically in order to produce the wanted AMC surface. Nevertheless, the simplicity of such model beside its fastness and accuracy are of great importance.

3.5.2.2 MSRR Reflection Characterization

The magnitude of the reflection coefficient S_{11}, its phase and the surface impedance of the simulated MSRR unit cell are shown on Figure 3-32. The initial dimensions results in a resonance around 2.4 GHz. The reflection phase of the AMC surface decreases from 180º to -180º. This surface exhibits 90º around 2.32 GHz and 0º reflection phase around the resonant frequency 2.4 GHz.

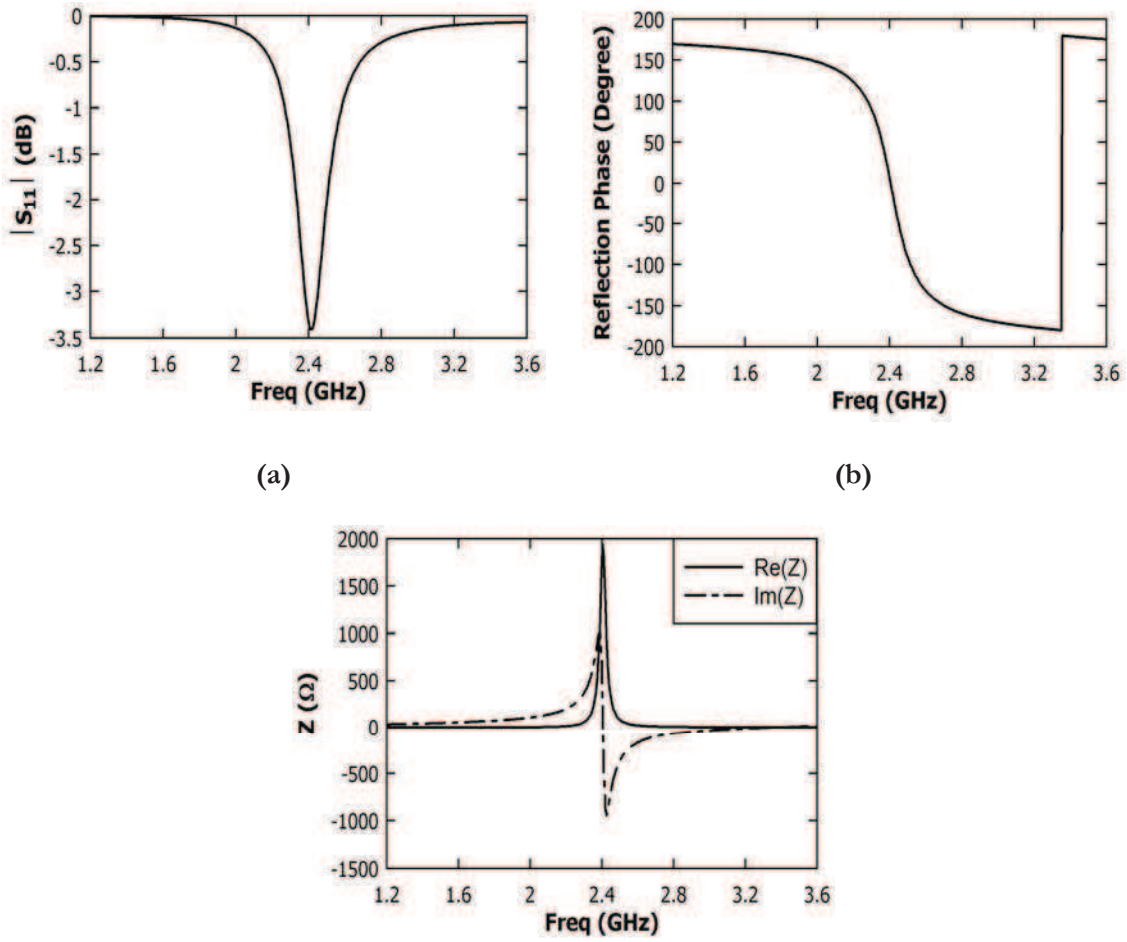

Figure 3-32: (a) Magnitude (b) reflection (c) impedance of the return loss of the unit cell

This structure presents an impedance of 2000 Ω at resonance; a very high value if compared with 120π. With respect to this unusual boundary condition, AMC surface can operate as a new type of ground plane for low-profile antennas.

3.5.2.3 AMC Surface Reflection Phase

In order to compare the reflection characteristics of an AMC surface with those obtained for a MSRR unit cell structure, an array of five MSRRs is simulated by applying the same boundary conditions. The results are not shown in the paper because they are very close to the previous ones got for a unit cell.

3.5.3 Dipole Low Profile Antenna

Once the reflection coefficient of the AMC surface is characterized, one can proceed to investigate the performance of a low profile dipole antenna fixed nearby this surface that is

proposed to operate instead of a ground plane. Two different AMC surfaces containing different numbers of MSRR unit cells are investigated. The next two paragraphs are dedicated to compare the gain and the directivity of two antennas positioned above two surfaces of 7×7 and 9×9 MSRR unit cells respectively.

3.5.3.1 7×7 Cells Array

Figure 3-33 shows the complete structure including the dipole rectangular antenna and the AMC ground plane. The antenna is placed 3 mm above the AMC surface whereas its planar dimensions are 2.4 mm × 56.37 mm.

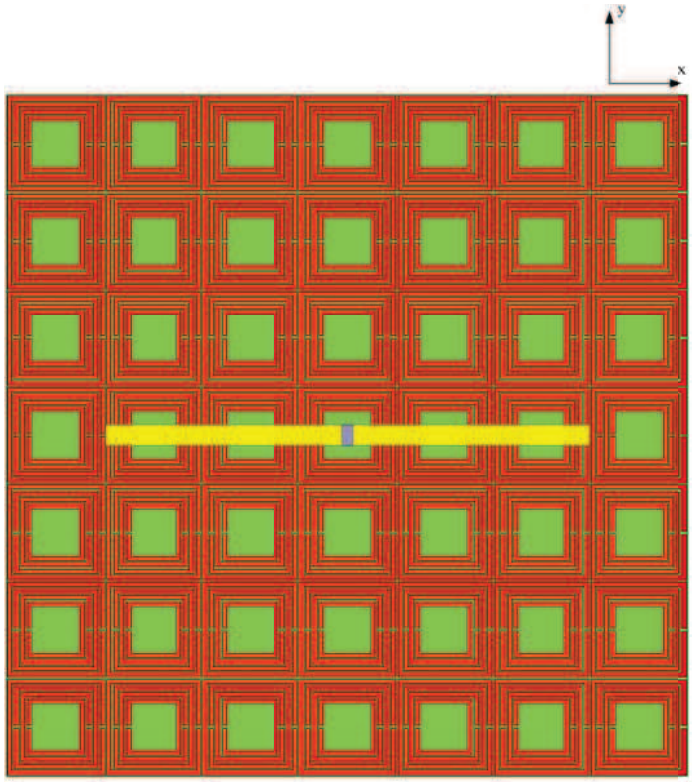

Figure 3-33: 2D view of a 7×7 cells AMC array

In order to compare the AMC surface with that of a PEC, the return loss of the same antenna on solid PEC ground plane is simulated and depicted on the same graph that presents the return loss of an antenna above the AMC ground (see Figure 3-34).

One can notice that the return loss of the dipole is only -0.35 dB if located above the PEC ground plane. This is because PEC surface has a 180º reflection phase. That is, the image current cancels that of the original dipole and a very low return loss results. On the other hand, the return loss is -15.2 dB at 2.3 GHz when employing an AMC surface. The latter serves as a

ground plane for the dipole antenna especially when the reflection phase varies from 90º to -90º where a good match is achieved.

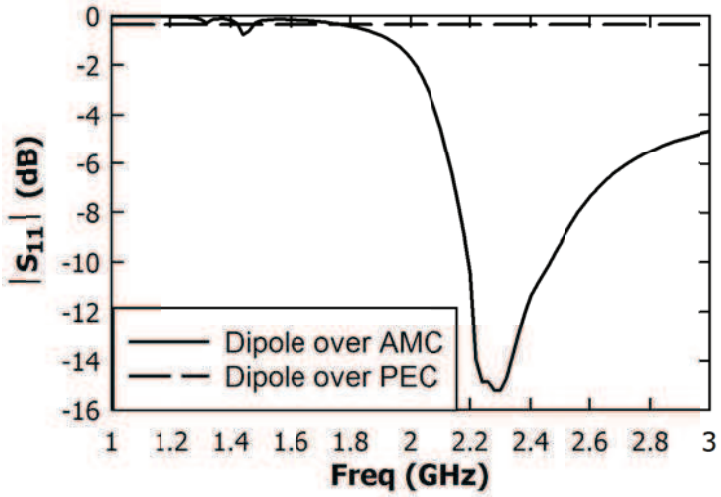

Figure 3-34: Return loss magnitude of the dipole antenna over a) PEC and b) 7×7 cells AMC array

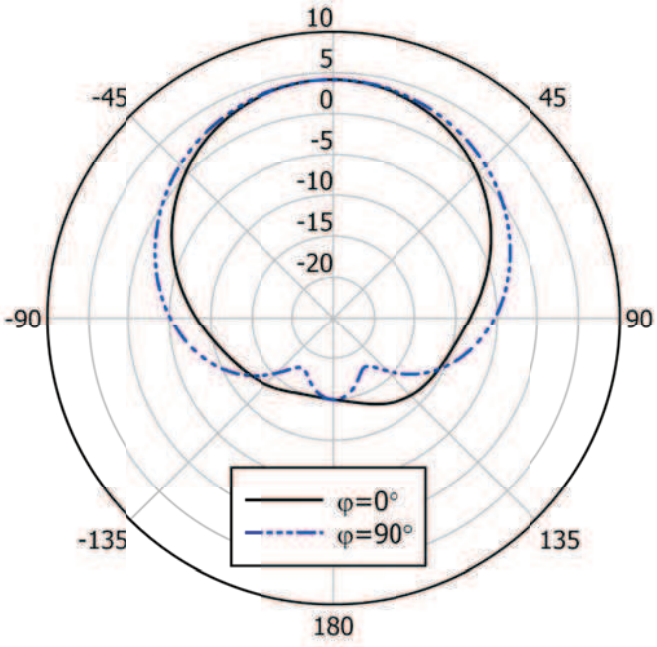

Figure 3-35: Antenna directivity above a 7×7 cells AMC array

The radiation patterns of the antenna are then evaluated. Figure 3-35 shows the diagram of the dipole directivity for φ = 0º and 90º. The result is evident as the directivity of the antenna reaches 4 dB at θ = 0º.

3.5.3.2 9 × 9 Cells Array

After having highlighted on the performance of an AMC surface based on an array of 7×7 MSRRs, the study continues to observe the performance of another dipole antenna located above an array of 9×9 MSRR cells. The dimensions of the antenna and the vertical distance separating it from the AMC surface are the same as those in the previous paragraph.

The dipole return loss and the proposed AMC reflection phase are both plotted in Figure 3-36. The practical operational frequency band of the AMC structure is the frequency region inside where the AMC shows 90º ±45º reflection phases [3-32]. This is of great agreement with the presented results. The return loss is -13 dB at 2.4 GHz.

The other resonance observed at 2.9 GHz is due to the finite size of the ground plane used. This might be avoided by changing the number of cells in the array; more investigations and simulations are required.

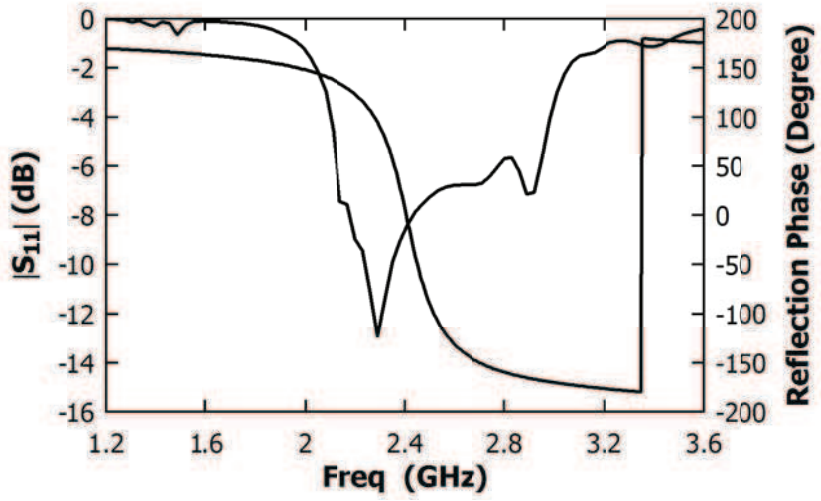

Figure 3-36: Return loss phase and magnitude for the dipole antenna over 9×9 cells AMC array

An obvious improvement obtained in this array is the antenna radiation patterns diagrammed in Figure10. That is, the new directivity attains 6 dB; 2 dB of enhancement if compared with the 7×7 cells array.

The performance of a 9×9 cells AMC array could be suggested as a perspective to follow this work. Unfortunately, more resources concerning the computational tools are needed to simulate such structure with high accuracy.

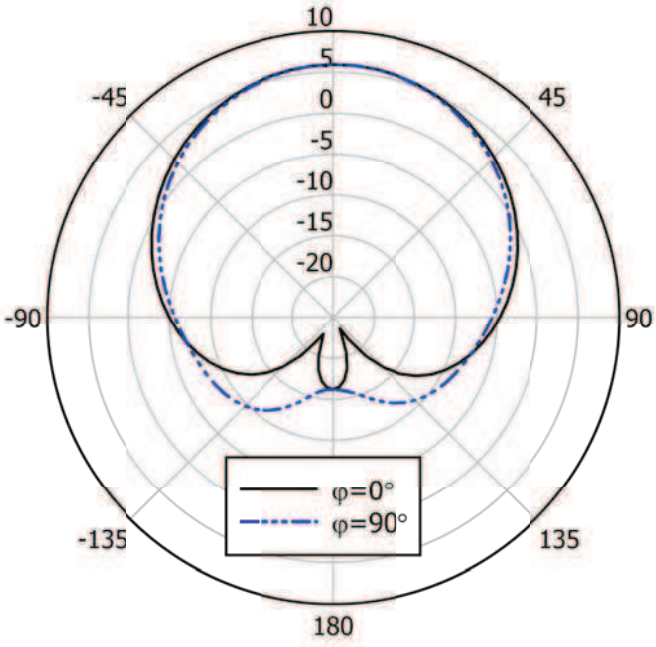

Figure 3-37: Antenna directivity above a 9×9 cells AMC array

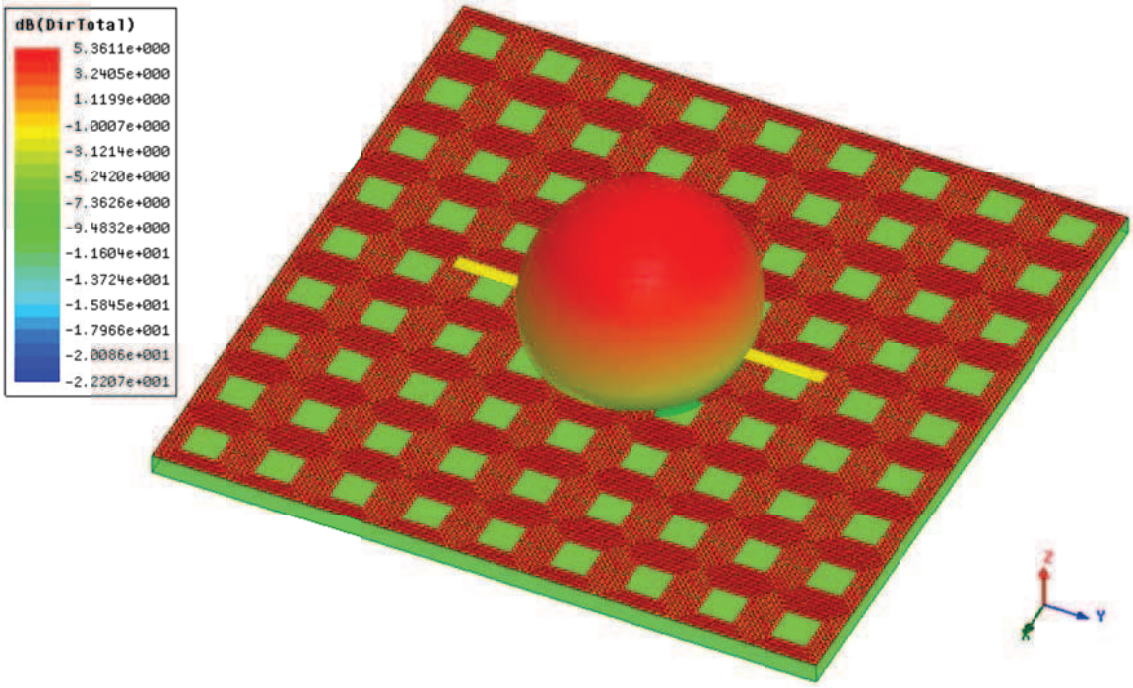

Figure 3-38: Radiation pattern of the dipole antenna at 2.4 GHz

The radiation pattern of the rectangular dipole antenna above the 9×9 cells AMC plane at the operating frequency 2.4 GHz is shown in Figure 3-38.

3.6 Conclusion

In this chapter, the performance improvement of a dipole antenna placed on AMC surface is demonstrated. Using Metamaterial structures, the gain and the directivity of such antenna have been widely improved. All the obtained results have proved that the MSRR cells can perfectly replace the conventional ground plane in order to improve the radiation characteristics. Moreover, the impact of the MSRR cells number on the antenna performance has also been investigated.

3.7 References

[3-1] Smith, D. R.; Padilla, W. J.; Vier, D. C.; Nemat-Nasser S. C. & Schultz, S. "Composite medium with simultaneously negative permeability and permittivity,"*Physical Review Letters*, vol. 84, May 2000, pp. 4184-4187.

[3-2] Veselago, V. G. "The electrodynamics of substances with simultaneously negative values of ε and μ,"*Soviet Physics Uspekhi*, January 1968, pp. 509-514.

[3-3] Schurig, D.; Mock, J. J.; Justice, B. J.; Cummer, S. A.; Pendry, J. B.; Starr A. F. & Smith, D. R. "Metamaterial electromagnetic cloak at microwave frequencies,"*Science*, vol. 314, 2006, pp. 977-980.

[3-4] Baena, J. D.; Bonache, J.; Martín F.; Sillero, R. M.; Falcone, F.; Lopetegi, T.; Laso, M. A. G.; García-García, J.; Gil, I.; Portillo, M. F. & Sorolla, M. "Equivalent-circuit models for split-ring resonators and complementary split-ring resonators coupled to planar transmission lines,"*IEEE Transactions on Microwave Theory and Techniques*, vol. 53, April 2005, pp. 1451-1461

[3-5] Falcone, F.; Lopetegi, T.; Laso, M. A. G.; Baena, J. D.; Bonache, J.; Beruete, M.; Marqués, R.; Martín, F. & Sorolla, M. "Babinet principle applied to the design of metasurfaces and Metamaterials,"*Physical Review Letters*, vol. 93, November 2004.

[3-6] Martín, F.; Bonache, J.; Falcone, F.; Sorolla M. & Marqués, R. "Split ring resonator-based left handed coplanar waveguide,"*Applied Physics Letters*, vol. 83, December 2003, pp. 4652-4654.

[3-7] Alici, K. B.; Bilotti, F.; Vegni L. & Ozbay, E. "Miniaturized negative permeability materials,"*Applied Physics Letters*, vol. 91, August 2007

[3-8] Bilotti, F.; Toscano, A.; Vegni, L.; Aydin, K.; Alici K. B. & Ozbay, E. "Equivalent-circuit models for the design of Metamaterials based on artificial magnetic inclusions,"*IEEE Transactions on Microwave Theory and Techniques*, vol. 55, December 2007.

[3-9] Marqués, R.; Mesa, F.; Martel, J. & Medina, F. "Comparative analysis of edge- and broadsidecoupled split ring resonators for Metamaterial design - Theory and experiments,"*IEEE Transactions on Antennas and Propagation*, vol. 51, October 2003.

[3-10] Aznar, F.; Gil, M.; Bonache, J.; Jelinek, L.; Baena, J. D.; Marqués, R. & F. Martín, "Characterization of miniaturized Metamaterial resonators coupled to planar transmission lines through parameter extraction,"*Journal of Applied Physics*, Vol 104, December 2008.

[3-11] Martel, J.; Marqués, R.; Falcone, F.; Baena, J. D.; Medina, F.; Martín F. & Sorolla, M. "A new LC series element for compact bandpass filter design,"*IEEE Microwave and Wireless Components Letters*, vol. 14, May 2004.

[3-12] Vélez, A.; Bonache, J. & Martín, F. "Metamaterial transmission lines with tunable phase and characteristic impedance based on complementary split ring resonators,"*Microwave and Optical Technology Letters*, Vol. 51 Issue 8, August 2009

[3-13] Durán-Sindreu, M.; Aznar, F.; Vélez, A.; Bonache, J. & Martín, F. "New composite, Right/Left handed transmission lines based on electrically small, open resonators,"*Proceedings of IEEE MTT-S International Microwave Symposium*, pp. 45-48, Boston (MA), USA, June 2009.

[3-14] J. D. Baena, R. Marques, F. Medina, and J. Martel, "Artificial magnetic Metamaterial design by using spiral resonators," *Phys. Rev. B*, vol. 69, 2004.

[3-15] J. D. Baena, J. Bonache, F. Martín, R. Marqués, F. Falcone, T. Lopetegi, M. A. G. Laso, J. García–García, M. F. Portillo, and M. Sorolla, "Equivalent-circuit models for split-ring resonators and complementary split-ring resonators coupled to planar transmission lines," IEEE Trans. Microw. Theory Tech., vol. MTT-53, pp. 1451–1461, 2005.

[3-16] J. Garcia-Garcia, F. Martin, J. D. Baena, and R. Marques, "On the resonances and polarizabilities of split ring resonators," J. Appl. Phys., vol. 98, pp. 033103-1–9, Sep. 2005.

[3-17] F. Bilotti, "Application of Metamaterials for miniaturized components," in Workshop Metamaterials for Industry, Short Course for Industries and SMEs, Jouy-en-Josas, France, Nov. 28–30, 2005.

[3-18] R. Marqués, F. Medina, and R. Rafii-El-Idrissi, "Role of bianisotropy in negative permeability and left-handed Metamaterials," *Phys. Rev. B*, vol. 65, pp. 144 440(1)–144 440(6), 2002.

[3-19] I. Bahl and P. Bhartia, *Microwave Solid State Circuit Design*. New York: Wiley, 1988.

[3-20] F. Tefiku and E. Yamashita, "Capacitance characterization method for thick-conductor multiple planar ring structures on multiple substrate layers," *IEEE Trans. Microwave Theory Tech.*, vol. 40, pp. 1894–1902, Oct. 1992.

[3-21] C.Saha and J.Y. Siddiqui, Versatile CAD Formulation for Estimation of the Resonant Frequency and Magnetic Polarizability of Circular Split Ring Resonators, Microwave Opt Technol Lett 21 (2011), 432-438.

[3-22] F.E. Terman, Radio engineers' handbook, Mcgraw-Hill, NewYork, 1943.

[3-23] F.W. Grover, Inductance calculations: Working formulas and tables, Dover Publications Inc., New York, 1946.

[3-24] M. Shamonin, E. Shamonina, V. Kalinin, and L. Solymar, Resonant Frequencies of a Split-ring Resonator: Analytical solutions and numerical simulations, J Appl Phys 95 (2004), 3778–3784.

[3-25] C. Balanis, Antenna Theory, Analysis, and Design, 2nd ed., John Wiley and Sons, New York (1997)

[3-26] D. Sievenpiper, L. Zhang, Romulo F. Jimenez Boras, N. G. Alexopolus and Eli Yablonovitch, "High-Impedance Electromagnetic Surfaces with a Forbidden Frequency Band," IEEE Trans. Microwave Theory and Tech., vol. 47, pp. 2059-2074, Nov. 1999.

[3-27] F.-R. Yang, K.-P.Ma, Y. Qian, and T. Itoh "A uniplanar compact photonic-bandgap (UC-PBG) structure and its applications for microwave circuit," IEEE Trans. Microwave Theory and Tech., vol. 47, pp. 1509-1514, Aug. 1999.

[3-28] A.S. Barlevy and Y.Rahmat-Samii "Characterization of electromagnetic band-gaps composed of multiple periodic tripods with interconnecting vias: Concept, analysis, and design," IEEE Trans. Antennas Propagat., vol. 49, pp. 242-253, Mar. 2001.

[3-29] F. Yang and Y.Rahmat-Samii "Reflection Phase Characterizations of the EBG Ground Plane for Low Profile Wire Antenna Applications," IEEE Trans. Antennas Propagat., vol. 51, pp. 2691-2703, Mar. 2001.

[3-30] P.-S. Kidal, "Definition of artificially soft and hard surfaces for electromagnetic waves," Electron.Lett., vol. 24, pp. 168-170, Feb. 1988.

[3-31] M.K. Taher Al-Nuaimi and W.G. Whittow, "Novel Planar AMC for Low Profile Antenna Applications," Loughborough Antennas & Propagation Conference, pp. 145-148, Nov. 2009.

[3-32] F. Yang, H. Mosallaei, and Y. Rahmat-Samii, "Chapter 34: Low Profile Antenna Performance Enhancement Utilizing Engineered Electromagnetic Materials," in Antenna Engineering Handbook, 4th edition, edited by J. Volakis, McGraw-Hill Inc., 2007.

[3-33] J. B. Pendry, A. J. Holden, D. J. Robbins, and W. J. Stewart, "Magnetism from conductors and enhanced nonlinear phenomena," IEEE Trans. Microwave Theory Tech., Vol. 47, No. 11, pp. 2075-2081, Nov. 1999.

[3-34] www.ansoft.com

[3-35] F. Bilotti, A. Toscano and L. Vegni,"Design of spiral and multiple split-ring resonators for the realization of miniaturized Metamaterial samples," IEEE Trans. Antennas Propag., vol. 55, pp. 2258-2267, Aug. 2007.

[3-36] R. W. Ziolkowski, "Design, Fabrication, and Testing of Double Negative Metamaterials," IEEE Trans. Antennas Propag., 2003, vol. 51, pp.1516-1529.

Chapter 4 Metamaterial-Loaded Multi-Band PCB Antennas

4.1 Introduction

Metamaterials can be broadly defined as electromagnetic structures engineered to achieve exotic or unusual properties [4-1], [4-3] & [4-10]. Recently these features have been used in microwave and antenna engineering to develop devices with extraordinary properties. For example, microwave devices with extraordinary characteristics such as miniaturization or operation over multiple frequency bands have been developed [4-1], [4-2] & [4-10]. The effort in the antenna field has been put on the use of Metamaterials for travelling-wave antennas and as substrates and superstrates to enhance the performance of the original antennas [4-1], [4-2] & [4-3].

One of the main applications of Metamaterial structures in microwave engineering is the development of artificial Left-Handed (LH) Transmission Lines (TLs) [4-1] & [4-2].These TLs are termed as LH because their behavior is the dual of the conventional or Right-Handed (RH) ones. In the LH TLs, the electric field, magnetic field and propagation vectors form a LH triplet, allowing the propagation of backward-waves, contrary to the conventional case. If we consider a TL as the concatenation of infinite unit cells, the equivalent circuit model of a LH unit cell is a series capacitance and a shunt inductance which is the dual of a RH unit cell (a series inductance and a shunt capacitance) [4-1].

During the last years, wireless systems have achieved a great popularity and penetration in society. Cellular systems, positioning systems (GPS, Galileo), personal area networks (Bluetooth) and wireless local area networks (WiFi) are good examples. This fact has made that user terminals designed for two or more of these services are very common nowadays.

4.2 Radiating Elements Characteristics

From the antenna engineering point of view, the radiating elements for these terminals require challenging features. The first one is multi-frequency, which means that the antennas

must work at two or more arbitrary bands simultaneously. Another challenging feature is multi functionality because in some cases different characteristics, such as polarization or radiation pattern, are required at each working band. Moreover, all these antennas must be small to integrate them into compact handheld devices attractive for the users.

4.3 Metamaterial Loaded Printed Dipoles

The use of cheap technologies is crucial for mass production. All these requirements cannot be easily achieved with conventional approaches. For that reason, novel technologies such as those based on Metamaterial structures are being proposed to fulfill all of these requirements.

The proposed approach is called Metamaterial-loaded printed circuit antennas. It is based on conventional printed antennas loaded with a small number of Metamaterial particles. Although Metamaterial structures are ideally formed by an infinite number of unit cells, a small number of unit cells can be used to achieve devices with enhanced performance for practical purposes. For example, microwave devices such as filters or couplers have been developed with a small number of Metamaterial cells [4-1], [4-2] & [4-10].

Furthermore, the use of a small number of particles does not increase the complexity and the size of the antennas, providing easy design and manufacturing processes and allowing the antennas to fit into modern devices. Finally, it is important to note that printed circuit board antennas have low profile, light weight, low cost and they are easy to integrate with circuitry and as elements of antenna arrays [4-4] & [4-9].

4.3.1 Dipole Antenna

The dipole is one of the most basic antennas. The dipole is a straight piece of wire cut in the center and fed with a balanced generator or transmission line. This structure is resonant, or non-reactive, at the frequency where the conductor length is 1/2 wavelength. For the ISM band, this length is approximately 6 cm or about 2 ½ inches. At this length, the dipole shows resonance, the feed impedance is resistive, and is close to 73 Ohms. This also holds true for a very thin wire in free space.

A practical dipole of some thickness, loaded with different dielectric materials (PCB etc.), and perhaps relatively close to ground, shows resonance at a slightly shorter length than calculated, and the radiation resistance drops somewhat. For dipoles not too close to ground, the shorting factor is typically in the range of 5-20%, the shorter being more heavily dielectric

loaded, and radiation resistance is in the range of 35-65Ohms.This dipole setup exhibits a relatively good match to a 50 Ohm generator, but the feed is differential.

A small ceramic balun can be used for single-ended feed. The bandwidth is typically 2-5%, depending on the return loss required. The radiation pattern in free space is doughnut-shaped, with pronounced dips along the direction of the wires. To fill out these dips, the outer ends of the antenna can be bent at a 45 degree angle. Several configurations are possible, including the broken arrow shape. Any materials close to the antenna can distort the radiation pattern.

To reduce the size of the dipole, several options exist:

- Replacing some of the wire length with loading coils.
- Bending the dipole ends back on the dipole.
- Folding the dipole into a meander pattern.
- Hairpin or coil loading of the center.
- Capacitive loading of the dipole ends.

As the antenna size is smaller, the lower the radiation resistance and the lower the efficiency. The antenna should also be removed somewhat from the ground plane, preferably at least ¼wavelengths (3 cm) but not less than 1 cm. Sometimes a loading technique is employed where the dipole ends are bent close to the ground plane, or even loaded with small capacitors to ground. This technique shorts the dipole considerably but causes heavy RF currents to flow in the ground plane, resulting in low efficiency. Often some of the other loading techniques result in better performance.

4.3.2 Miniaturization Trade Off

As stated, reducing antenna size results in reduced performance. Some of the parameters that suffer are:

- Reduced efficiency (or gain).
- Shorter range.
- Smaller useful bandwidth.
- More critical tuning.
- Increased sensitivity to component and PCB spread.
- Increased sensitivity to external factors.

As stated, several performance factors deteriorate with miniaturization, but some antenna types tolerate miniaturization better than others. How much a given antenna can be reduced in

size depends on the actual requirements for range, bandwidth, and repeatability. In general, an antenna can be reduced to half its natural size without much impact on performance.

However, after a one half reduction, performance gets progressively worse as the radiation resistance drops off rapidly. As a rule, one half the antenna sizes equals one quarter the radiation resistance. As loading and antenna losses often increase with reduced size, it is clear that efficiency drops off quite rapidly.

The amount of loss that can be tolerated depends on the range requirements. Bandwidth also decreases, which causes additional mismatch losses at the band ends. The bandwidth can be increased by resistive loading, but this often introduces even more loss than the mismatch loss. The low bandwidth combined with heavy loading requires a spread analysis to ensure adequate performance with variations in component values and PCB parameters.

As shown by these facts, it is often better not to reduce antenna size too much, if board space allows. Even if range requirements do not require optimum antenna performance, production problems and spread are minimized. It is also best to keep some clearance between the antenna and nearby objects. Although the antenna may be re-tuned to compensate for the loading introduced by the surroundings, tuning becomes more critical, and the radiation pattern can be heavily distorted.

4.4 The Trap-Loaded Antenna

4.4.1 General Antenna Design Guides

A typical symmetric trap-loaded antenna is illustrated in Figure 4-1. The antenna has a total length of 2L, the traps are located a distance "s" from the center, and the diameter of the antenna is "2a". The surface of the antenna is assumed to be perfectly conducting, and both the source and the trap are assumed to be very small. The trap Z_L is either a parallel inductor-capacitor circuit or a short-circuited quarter-wave transmission line. The trap is usually adjusted to be anti-resonant when "s" is a quarter of a wavelength.

When L is approximately 3/4 of a wavelength, and "s" is approximately 1/4 of a wavelength, the antenna is a type of Franklin array, an antenna that has been used since the early days of radio [4-14]. It is frequently used as a radio amateur antenna [4-15]. The input impedance of a Franklin antenna is believed to be about 300Ω [4-15] and the current distribution is assumed to be sinusoidal and of equal amplitude on both the main section (IzI<=s) and the parasitic elements (s <= IzI<= L), [4-14]. Harrington's results [4-16] for one parasitic element indicate that the current distribution is approximately sinusoidal and that the current amplitude on the parasitic element is somewhat less than on the driven element.

The Franklin array is used to produce a radiation pattern similar to a collinear array of half-wave dipoles. The trap is expected to produce an additional 180° phase shift at the nulls in the current distribution so that the current is in phase along the entire length of the antenna [4-15], [4-17].

When L is approximately 1/2 of a wavelength and "s" is approximately 1/4 of a wavelength, the trap-loaded cylindrical antenna is a special case of what is commonly referred to as the trap antenna. Several authors [4-13],[4-15], [4-18], and [4-19] have described how to construct trap antennas that operate as multiband dipoles.

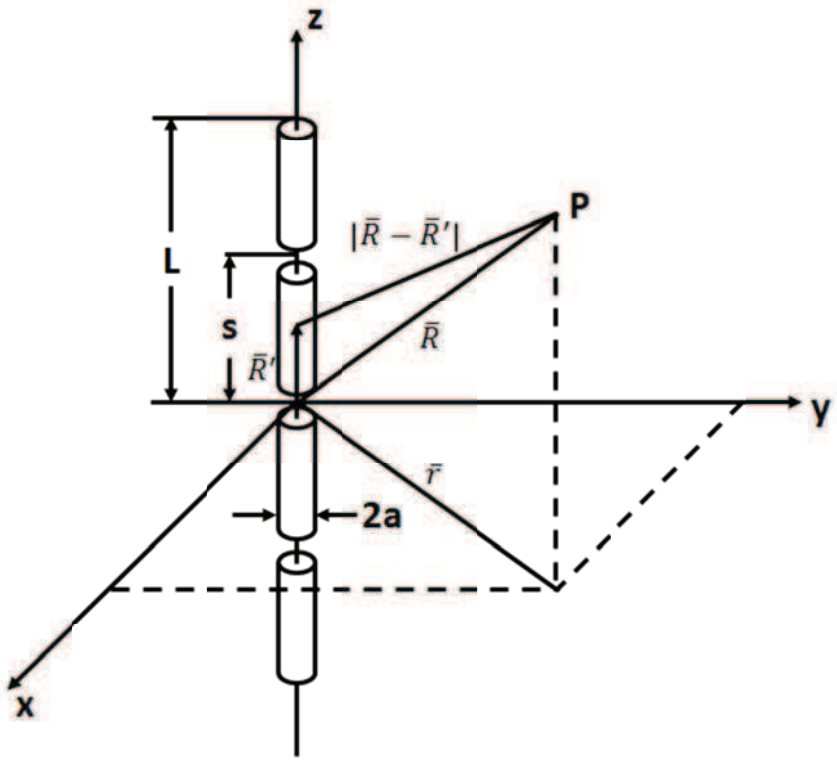

Figure 4-1: Geometry of trap-loaded cylindrical antenna

The trap is adjusted to be anti-resonant (i.e. an open circuit.) at the upper resonant frequency of the antenna. This forces a null in the current distribution a quarter wave length from the end and effectively suppresses the current in the outer section. With the current suppressed, the antenna produces a radiation pattern similar to a half-wave dipole rather than a full-wave dipole [4-13],[4-15], [4-18], and [4-19].

Below the anti-resonant frequency of the trap, the trap acts as an inductance. Above the anti-resonant frequency, the trap acts as a capacitance. Reactance loaded cylindrical antennas

have been studied for L less than 1/10 wavelength [4-20] as well as for L greater than 1/10 wavelength [4-15]. Resistance loaded cylindrical antennas have also been explored [4-21], [4-22].

4.4.2 Current Distribution

The characteristics of thin-wire, center-fed, linear antennas have been studied extensively by King [4-23]. Through the use of an integral equation technique, the current distribution along such an antenna may be determined. It is well known that a conventional cylindrical antenna of this type supports an essentially standing wave distribution of current. Such an antenna is highly frequency sensitive in that its input impedance is a strong function of frequency. A traveling-wave linear antenna supports a distribution of current which is essentially an outward traveling wave.

As compared with a conventional dipole, the traveling-wave antenna has two practical aspects that are desirable for certain purposes: a broadband character where by the input impedance is relatively independent of frequency, and a modified radiation pattern having a wider beam width and a notable absence of minor lobes for a long antenna. In order to realize a traveling-wave antenna, its construction must necessarily be altered from that of a conventional standing wave dipole.

It has been established that a traveling-wave antenna may be realized through the use of a resistance loading technique. Using a transmission line analogy, Altshuler [4-24] proposed an optimum double resistance loading to be located a quarter wavelengths from the ends of the antenna. Such a resistance loaded antenna was found experimentally to support a traveling wave of current along most of its length. Although the loading is properly located only at a single frequency, the antenna impedance was measured to be reasonably constant over a wide frequency range.

More recently, Wu [4-25] and King [4-23] demonstrated that a traveling-wave antenna may be realized by constructing it from a dissipative conductor whose resistance varies with position along the cylinder. Broadband input impedance is obtained, although the traveling wave of current decays rapidly as it advances outward along the dissipative antenna.

These techniques share the common disadvantage of a very low radiating efficiency (of the order of 50 percent or less) due to dissipation in the resistive loadings. It is the objective of the present study to investigate the possibility of realizing a traveling-wave antenna through use of a reactance loading technique. The antenna is assumed to consist of a thin cylinder, doubly loaded with a pair of identical impedances.

The distribution of current along the cylinder is determined approximately in terms of its dimensions and the impedance and position of the loading. From this result, the optimum loading to obtain an outward traveling wave of current is determined. There are two degrees of freedom in choosing such a loading: its impedance and position. Through a proper choice of its location, it is found that a purely reactive loading may be utilized.

4.4.3 Simple Rectangular Dipole Antenna

The following step is to validate the principle of trap antenna by applying the suitable dimensions and conditions to have a radiation at a 1.5 GHz which is the frequency of interest. This latter is the functioning frequency of the Global Positioning System (GPS).

We start by a simple rectangular antenna that should radiate at 1.5 GHz by choosing the length of each arm approximately equals to 0.23 times the wavelength (λ_0). This selection is for the reason of cancelling the imaginary part of the input impedance in order to have the resonance at c/λ_0 [4-15]. A theoretical proof of this selection will appear soon in the results of the simulations.

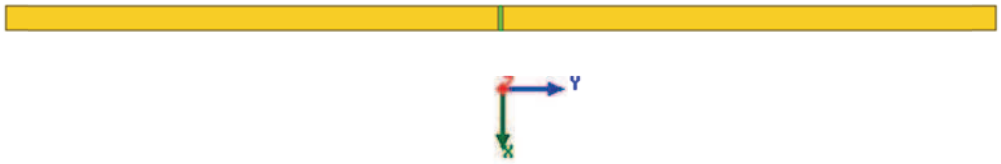

Figure 4-2: Top view of the simple rectangular dipole antenna

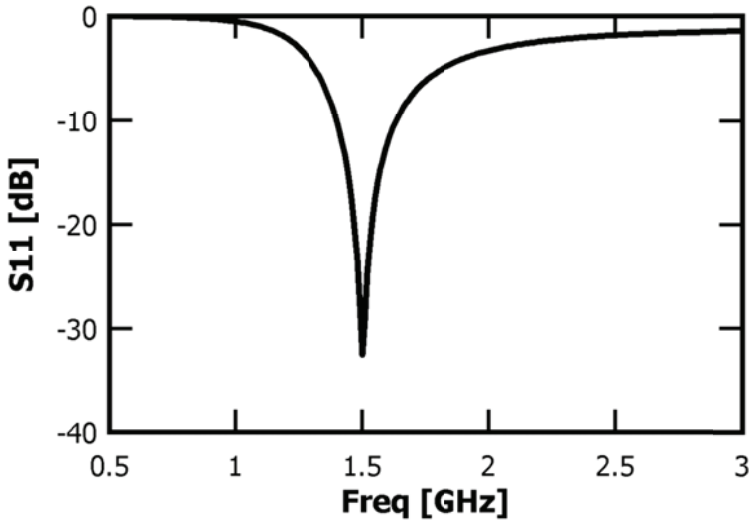

Figure 4-3: Reflection coefficient S_{11}

Figure 4-2 presents a view of the simple $\lambda_0/2$ dipole antenna simulated on HFSS. The length of each arm is set to $0.23\lambda_0$ which is equal to 46 mm whereas its width is set to $\lambda_0/100$; a recommended value to avoid transversal current. The reflection coefficient resulted from the electromagnetic simulation of the structure shown above is depicted on Figure 4-3. One could obviously remark the S_{11} dip at 1.5 GHz; a result that validates the design and its dimensions.

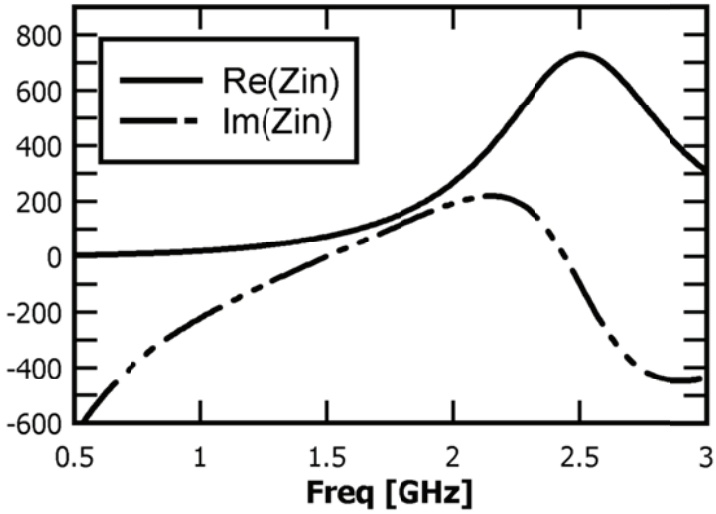

Figure 4-4: Input impedance of the unloaded dipole antenna

The input impedance is also of interest because it evaluates the level of matching resulted at the operating frequencies. For this reason, the real and imaginary of Z_{in} are expressed in Figure 4-4. As mentioned before, $Im(Z_{in})$ should be zero at the operating frequency (1.5 GHz), this is well obtained from the graph whereas the real part Re(Zin) is found to be 76 Ω which is very close the resistance of a matched half wave dipole antenna.

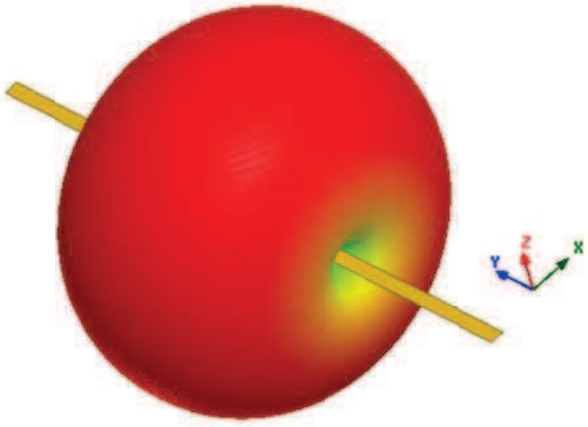

Figure 4-5: 3D Gain pattern of the unloaded antenna

Nevertheless, the 3D gain pattern at the operating frequency is given in Figure 4-5. It is observed that its shape is omni-directional.

4.4.4 Trap-Loaded Rectangular Dipole Antenna

After validating the radiation of the antenna at the frequency of interest, the work now concentrates on creating another radiation frequency by loading the antenna by two traps; one trap on each arm.

We start by applying a lumped RLC trap that is retrieved in HFSS. The resistance is set to zero whereas the values of L & C lumped elements are selected such a way a radiation at 2.4 GHz is obtained. For this purpose, C is chosen to be 1.5 pF whereas the inductance L is set to 3 nH.

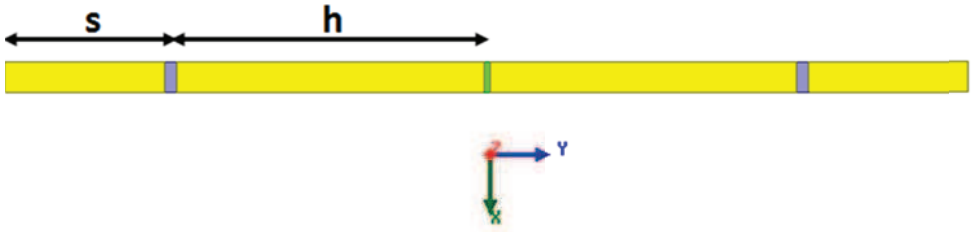

Figure 4-6: Rectangular antenna loaded by two traps

The total length of the arm (h + s) is now 0.2 times the operating wavelength (see Figure 4-6).

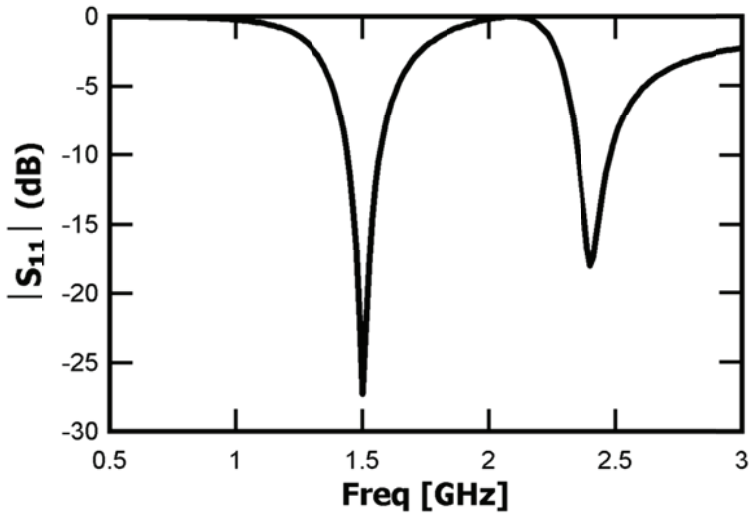

Figure 4-7: Reflection coefficient of the trap-loaded dipole antenna

This is illustrated by the fact that adding an inductive trap increases the original length of the arm; and consequently decreasing its radiating frequency. This is compensated by decreasing

($0.2\lambda_0$ instead of $0.23\lambda_0$) the length of the arm in order to keep the frequency of interest (1.5 GHz).

The simulation of the antenna described above produces the reflection coefficient presented in Figure 4-7. It is well seen that two frequencies are now operating for this antenna, one at 1.5 GHz whereas the 2nd is at 2.4 GHz.

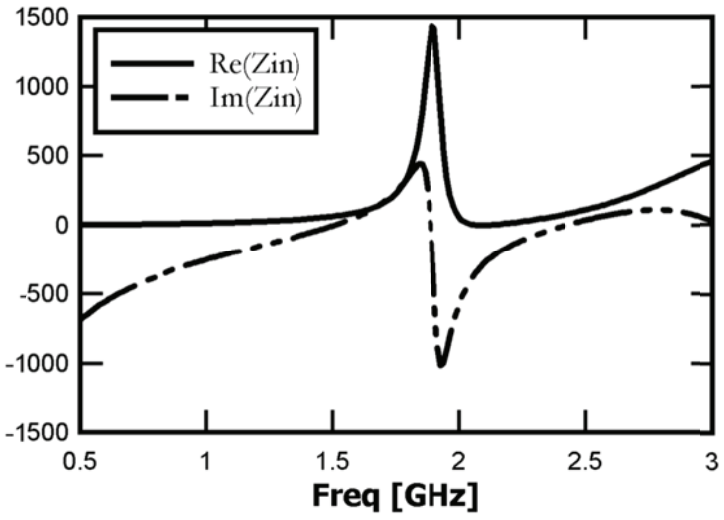

Figure 4-8: Input impedance of the trap-loaded antenna

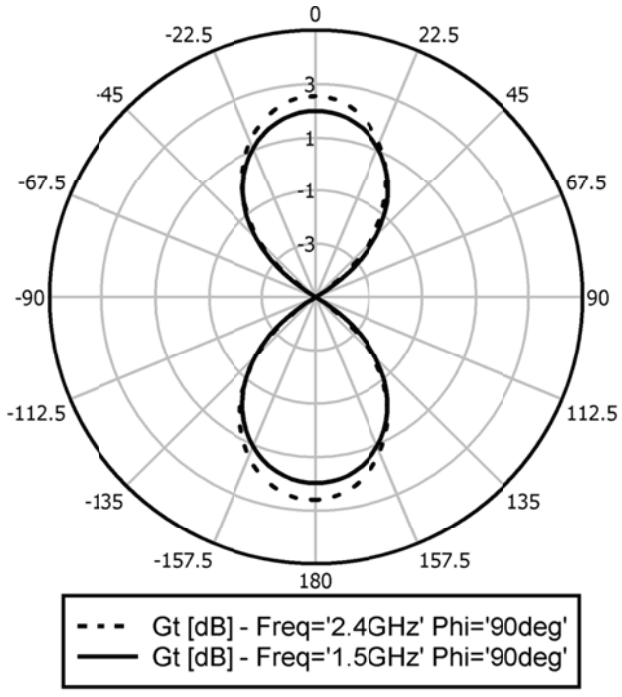

Figure 4-9: Radiation pattern at the operating frequencies of the trap-loaded antenna

Once again, the impedance of the antenna is studied; its real and imaginary parts are shown on Figure 4-8. Im(Z_{in}) is null at the two frequencies 1.5 and 2.4 GHz. On the other hand, Re(Z_{in}) is 65Ω at 1.5 GHz and 74Ωat 2.4 GHz; two perfect values for matching the dipole antenna.

Figure 4-9 shows the radiation pattern of the antenna at the two operating frequencies. The patterns are very close and both have an omni-directional shape. One can conclude that with this configuration, and despite that the antenna operates in a dual-mode function, the radiation pattern is conserved and consequently the gain at both frequencies; a very powerful point registered for such configuration.

4.4.5 SRR-Loaded Rectangular Dipole Antenna

In chapter three, a detailed study about SRR inclusion is presented. It is concluded that SRR has an LC equivalent circuit; its dimensions define the operating frequency. Thus, this inclusion could be implemented in the structure of the dipole antenna in order to replace the LC circuit and consequently obtaining a second operating frequency in addition to the 1st one obtained from the $\lambda_0/4$ length of the arm.

The antenna presented is based on the dipole printed on a Rohacell dielectric substrate of permittivity 1.04 and thickness 1.5 mm. One, two or even four SRRs can be printed on the opposite side of each dipole branch. A top view indicating the geometry of the proposed antenna is shown in Figure 4-10.

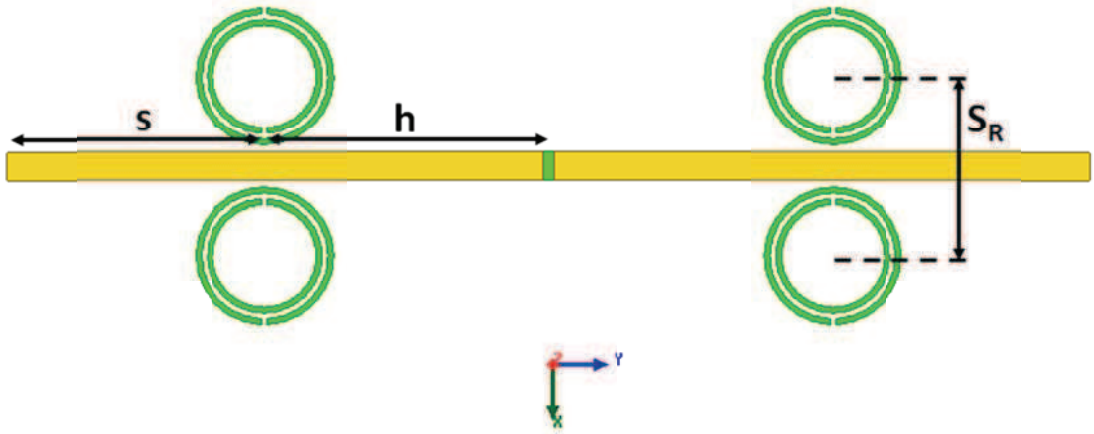

Figure 4-10: Top view of the dipole antenna and the SRR inclusions

The length of the dipole is "h+s" whereas the SRRs are placed at a distance "h" from the dipole center (along y-axis), and the separation (along x-axis) between the centers of the SRRs is

"S_R". Fig shows a close 3D view of the inclusions in order to visualize their orientation and consequently the excitation.

This configuration provides dual-frequency performance. Its first frequency is due to the dipole itself, while the second one is originated in the vicinity of the SRR self-resonant frequency. It should be pointed out that SRRs are not radiating but storing and dissipating a large amount of reactive energy. Therefore, for this second frequency, the radiating element is made up of the linear current distribution on the dipole antenna between the SRRs arrangements.

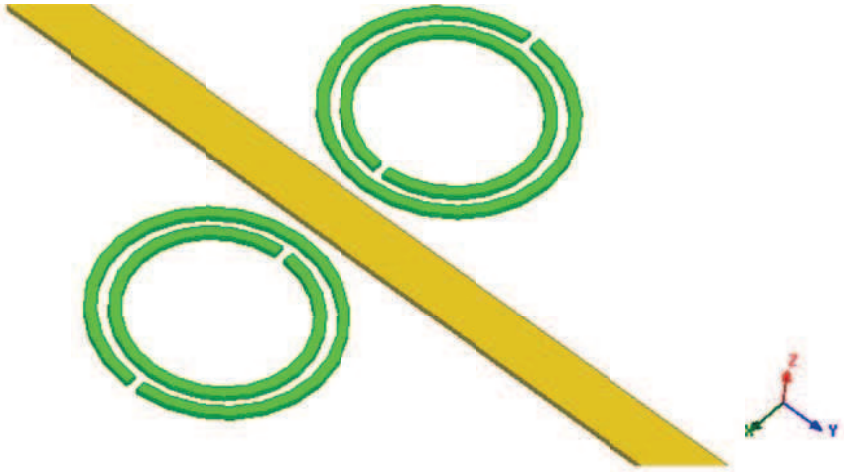

Figure 4-11: Zoomed 3D view of the SRR inclusions beside the antenna

Once again, the simulation of the antenna produces two frequencies operating at 1.5 GHz and 2.4 GHz (see Figure 4-12). The external radius R_{ext} of the SRR is 5.5 mm whereas the distance "h" separating the inclusions and the center of the antenna is 22 mm.

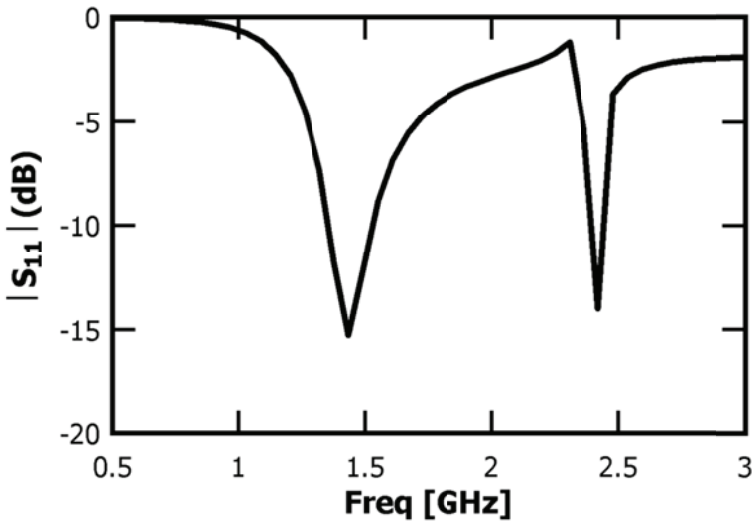

Figure 4-12: Reflection coefficient of the SRR-loaded dipole antenna

The real and imaginary parts of the input impedance are shown Figure 4-13. Im(Z_{in}) is null at the two frequencies 1.5 and 2.4 GHz and Re(Z_{in}) is 81Ω at 1.5 GHz and 134Ω at 2.4 GHz.

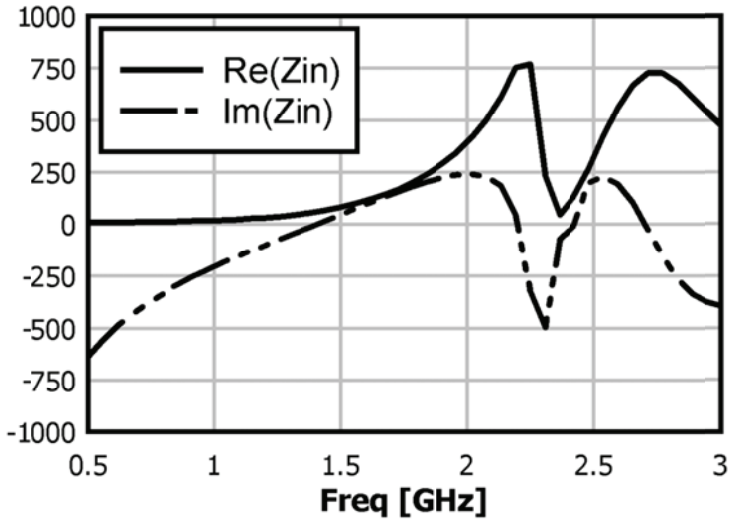

Figure 4-13: Input impedance of the SRR-loaded antenna

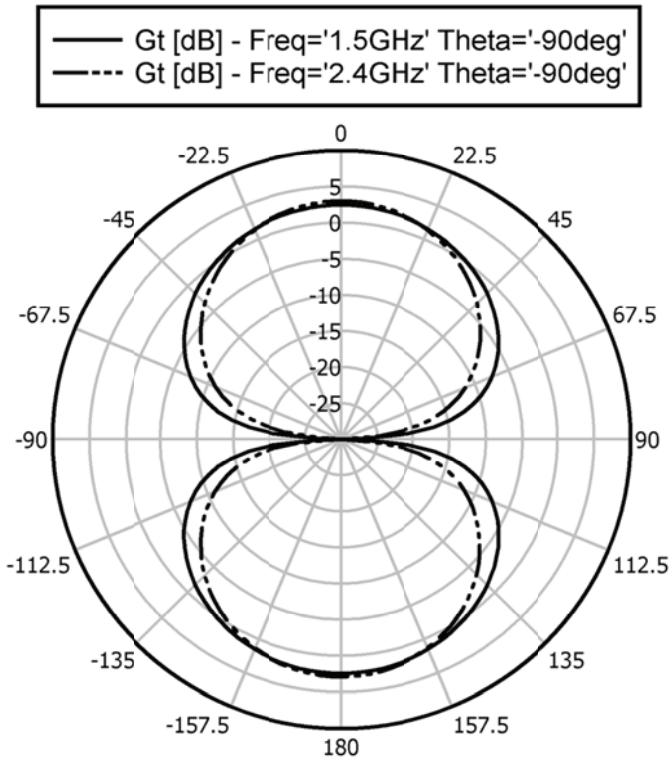

Figure 4-14: Radiation pattern at the operating frequencies of the SRR-loaded antenna (θ=-90°)

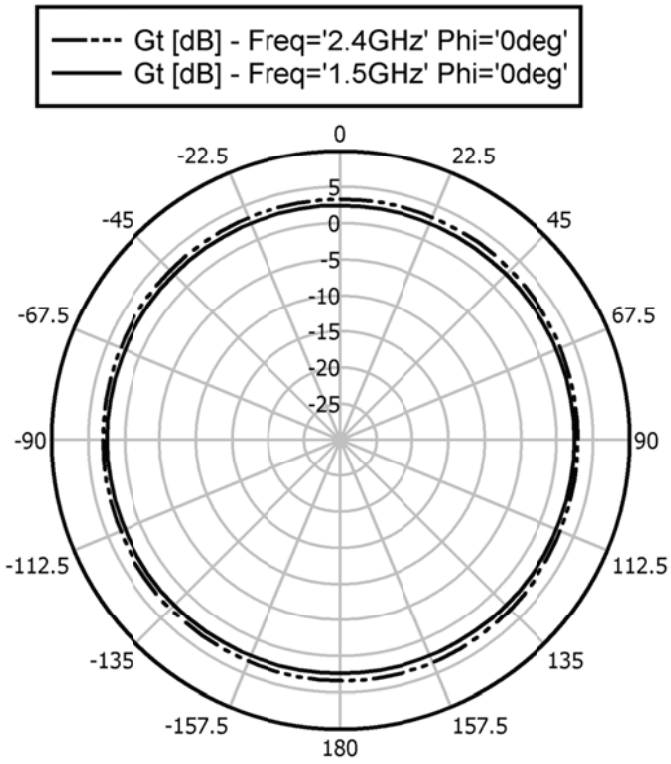

Figure 4-15: Radiation pattern at the operating frequencies of the SRR-loaded antenna (φ=0°)

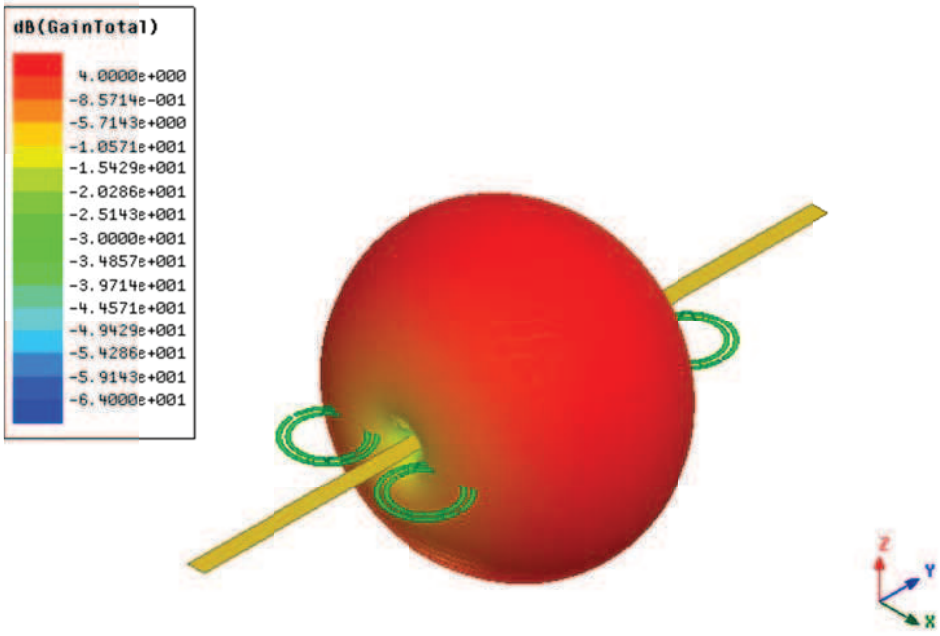

Figure 4-16: 3D Gain pattern of the SRR-loaded antenna

The two-dimensional omni-directional shape radiation patterns of the antenna at the two operating frequencies are shown in Figure 4-14 for θ=-90° and in Figure 4-15 for φ=0°. One can note that the pattern is conserved and consequently the gain at both frequencies.

The omni-directional 3D pattern of the gain at the operating frequencies of the antenna is depicted in Figure 4-16. Note that the shape of the pattern is omni-directional for both frequencies.

4.4.6 MSRR-Loaded Dipole Antenna

The next structure that could be implemented as a resonating circuit in order to create multi-band performance is the Multi Split Ring Resonator (MSRR). A detailed study about the MSRR is presented throughout this thesis; the study includes calculating its physical characteristics on one hand and calculating its resonant frequency on the other hand.

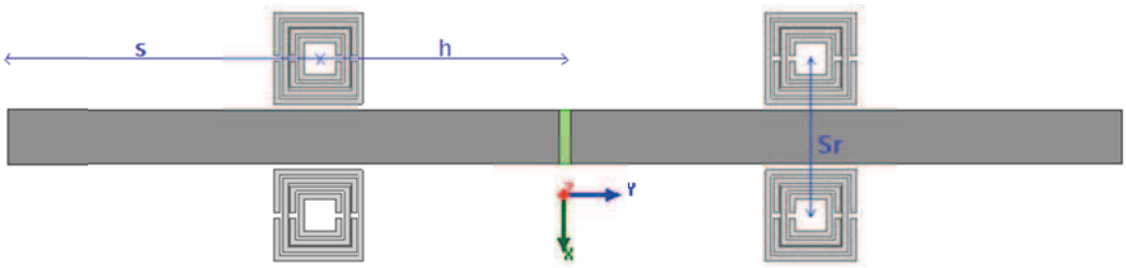

Figure 4-17: Top view of the dipole antenna and the MSRR inclusions

Figure 4-17 demonstrates the implementation of four MSRRs on the two arms of a dipole antenna. A 3D view of the obtained structure is depicted in Figure 4-18.

Just like studying the performance of the SRR-loaded dipole antenna, the reflection coefficient resulting from the simulation of the MSRR-loaded antenna is first calculated. Figure 4-19 shows the results obtained for different values of the horizontal distance "h" that separates between the centers of the MSRRs and the excitation point of the antenna (see Figure 4-17).

One can note that when "h" is equal to 24 mm (see Figure 4-20), a 2nd resonance appears at 2.4 GHz in addition to the 1st one which is obtained at 1.5 GHz, thus giving rise to a dual band performance of the proposed structure.

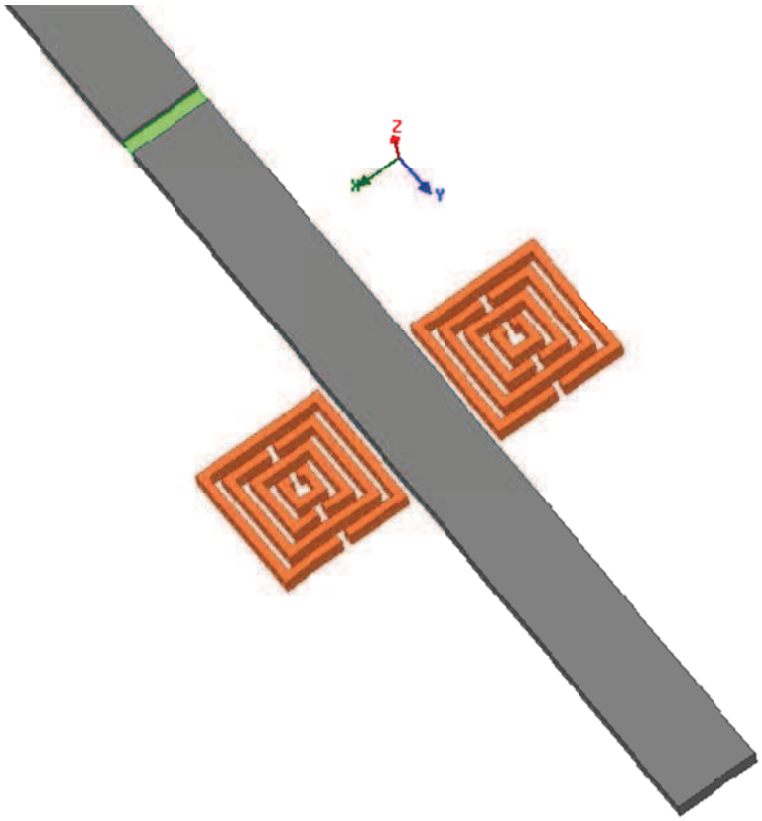

Figure 4-18: Zoomed 3D view of the SRR inclusions beside the antenna

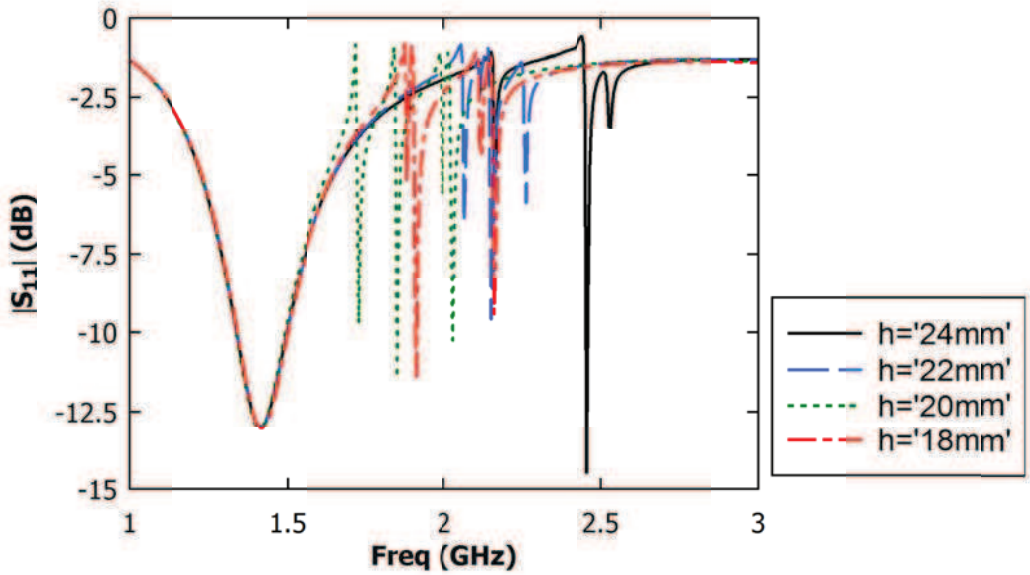

Figure 4-19: Magnitude of the reflection coefficient of MSRR as a function of distance *h*

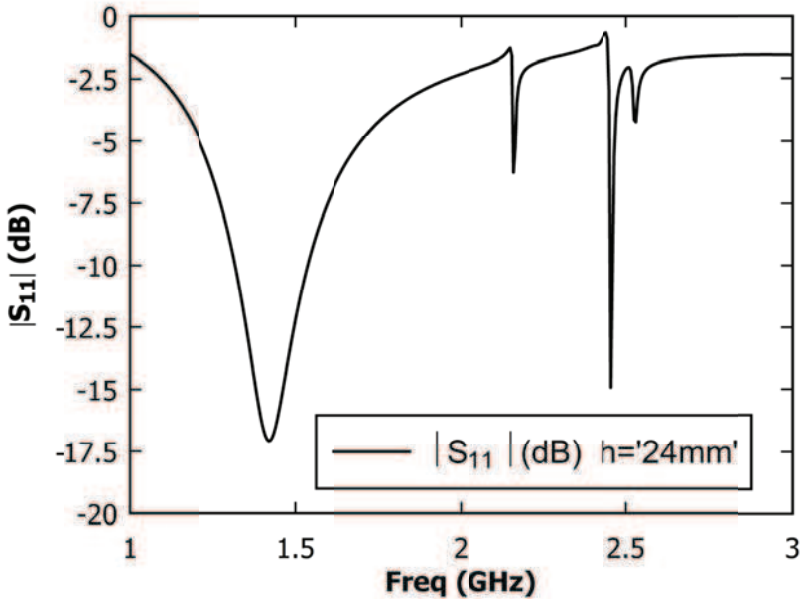

Figure 4-20: Magnitude of the reflection coefficient for h=24mm

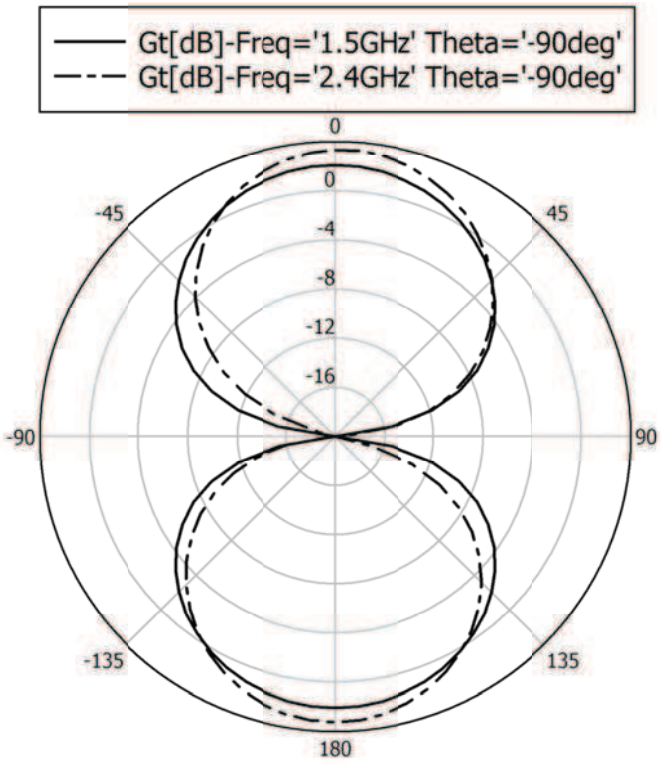

Figure 4-21: Radiation pattern at the operating frequencies of the MSRR-loaded antenna (θ=-90°)

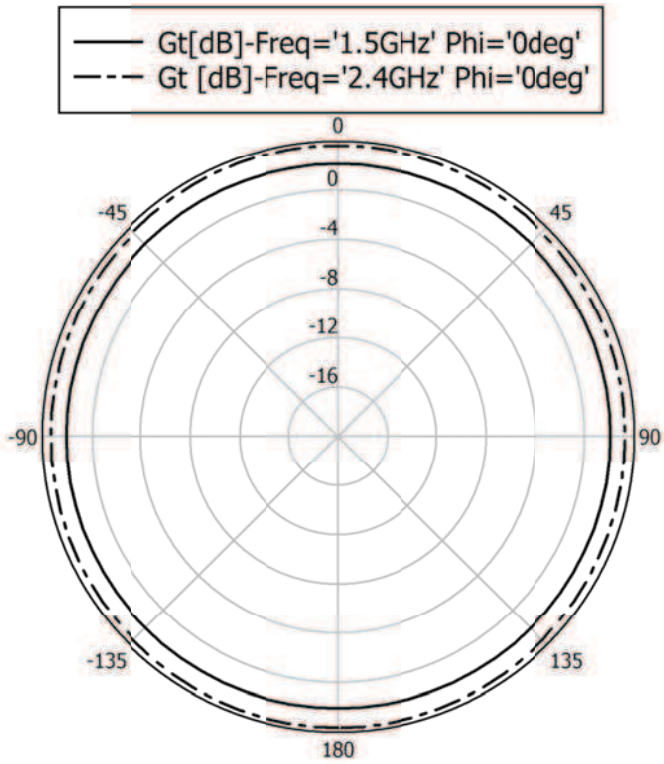

Figure 4-22: Radiation pattern at the operating frequencies of the MSRR-loaded antenna (φ=0°)

The two-dimensional omni-directional shape radiation patterns of the antenna at the two operating frequencies are shown in Figure 4-21 for θ=-90° and in Figure 4-22 for φ=0°. Proving the excellent performance resulted in the SRR-loaded antenna study, the patterns are conserved and therefore the gain at both operating frequencies.

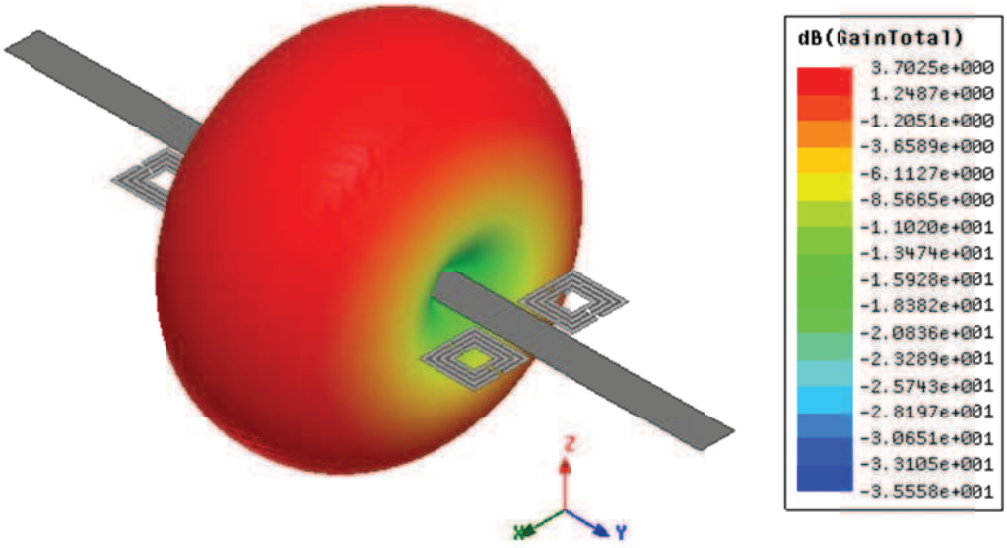

Figure 4-23: 3D Gain pattern of the loaded antenna at 2.4GHz

The omni-directional 3D pattern of the gain at the operating frequencies of the antenna is depicted in Figure 4-23. The omni-directional shape is the same for both operating frequencies.

4.5 Conclusion

In the last chapter of this manuscript, the functioning of radiating antennas having several phases and conditions are presented. As an introductory to the chapter, the characteristics of radiating elements as antenna engineering point of view are demonstrated. Then, in the second paragraph, dipole antennas and their functions are explained as an entrance to discuss the metamaterial loaded dipole antennas. The approach is based on loading the antennas with a small number of Metamaterial particles to achieve devices with enhanced performance for practical purposes.

The trap-loaded antenna is the first form presented in the following paragraph. Its general design is explained beside the demonstration of the current distribution by employing the integral equation technique resulting in a type that supports an essentially standing wave distribution of currents. Then, in order to compare the results with basic antenna structure, a simple rectangular dipole antenna is designed and simulated to have a radiating frequency at 1.5 GHz. The reflection coefficient, the input impedance and the radiation pattern are shown and validate the radiation at the target frequency.

The following step has focused on creating another radiation frequency by loading the antenna by two lumped RLC traps; one trap on each arm of the dipole antenna. The results are again proved when two frequencies at 1.5 and 2.4 GHz are created. The validation of this result is introduced in the next paragraph when a dipole antenna is loaded with two SRRs on each arm. This configuration of dual-frequency performance is approved since two frequencies are created at 1.5 and 2.4 GHz. The first one is due to the dipole itself, while the second is originated in the vicinity of the SRR self-resonant frequency.

The inclusion that replaced the SRR is the Multi Split Ring Resonator (MSRR). Two operating frequencies are obtained at 1.5 and 2.4 GHz giving rise to a dual-band structure similar to that obtained when loading the antenna with four SRRs.

As a perspective in the conclusion of this chapter, the realization of the MSRR-loaded dipole antenna could be accomplished to perform the measurements needed in order to validate the theoretical results experimentally.

4.6 References

[4-1] Caloz, C. &Itoh, T. (2004). Electromagnetic Metamaterials: Transmission Line Theory and Microwave Applications, Wiley-IEEE Press, ISBN: 0-471-669-857, New York

[4-2] Eleftheriades, G. V. &Balmain, K. G. (2005). Negative-Refraction Metamaterials: fundamental principles and applications, Wiley-IEEE Press, ISBN: 0-471-601-462, New York

[4-3] Engheta, N. &Ziolkowski, R. W. (2006).Metamaterials: Physics and Engineering Explorations, Wiley-IEEE Press, ISBN: 0-471-761-028, New York

[4-4] Garg, R.; Bhartia, P.; Bahl, I..&Ittipiboon, A. (2001).Microstrip Antenna Design Handbook, Artech House, ISBN: 0-89006-513-6, Norwood

[4-5] González-Posadas, V.; Segovia-Vargas, D.; Rajo-Iglesias, E.; Vázquez-Roy, J. L. & Martín-Pascual, C. (2006). Approximate Analysis of Short Circuited Ring Patch Antenna Working at TM01 Mode. IEEE Transactions on Antennas and Propagation, Vol. 54, No. 6, (June 2006), pp. 1875-1879, ISSN: 0018-926X

[4-6] Herraiz-Martínez, F. J.; González-Posadas, V.; Iñigo-Villacorta, F. & Segovia-Vargas, D.(2007). Low-cost Approach based on an Eigenfrequency Method to obtain the Dispersion Diagram in CRLH Structures. IEEE Microwave and Wireless Components Letters, Vol. 17, No.1, (January 2007), pp. 13-15, ISSN: 1531-1309

[4-7] Herraiz-Martínez, F. J.; García-Muñoz, L. E.; González-Posadas, V. & Segovia-Vargas, D. (2008). Multi-frequency and dual mode patch antennas partially filled with Left- Handed structures. IEEE Transactions on Antennas and Propagation, Vol. 58, No. 8, Part 2, (August 2008), pp. 2527-2539, ISSN: 0018-926X

[4-8] Herraiz-Martínez, F. J.; García-Muñoz, L. E.; González-Overjero, D.; González-Posadas V. & Segovia-Vargas, D. (2009). Dual-frequency printed dipole loaded with Split Ring Resonators. IEEE Antennas and Wireless Propagation Letters, Vol. 8, (2009), pp. 137-140, ISSN: 1536-1225

[4-9] James, J. R. & Hall, P. S. (1989). Handbook of Microstrip Antennas, Peter Peregrinus, ISBN: 0-86341-150-9, London

[4-10] Marqués, R.; Martín, F. &Sorolla, M. (2007).Metamaterials with Negative Parameters, John Wiley & Sons, ISBN: 978-0-471-74582-2, Hoboken, NJ

[4-11] Sanada, A.; Caloz, C. &Itoh, T. (2004).Planar Distributed Structures with Negative Refractive Index. IEEE Transactions on Microwave Theroy and Techniques, Vol. 52, No. 4, (April 2004), pp. 1252-1263, ISSN: 0018-9480

[4-12] Wadell, B.C. (1991). Transmission Line Design Handbook, Artech House, ISBN: 0-89006-436- 9, Norwood, MA

[4-13] A. Greenberg, "Simple trap construction for t,he multiband antenna," QST, vol. 40, no. 10, pp. 18-19, 120.

[4-14] H. P. Williams Antenna Theory and Design. London: Sir Isaac Pitman and Sons, 1950.

[4-15] The A.R.R.L. Antenna Book, 11th ed. Newington, Conn.: Newington, Conn: The American Radio Relay League, 1968.

[4-16] R. F. Harrington, Field Computation bg Moment Methods New york: Macmilla, 1968, sec. 6.2

[4-17] H. Jasik, Ed., Antenna Engineering Handbook. New York: McGraw-Hill, 1961, p. 22-7.

[4-18] W. M. Bell, "A trap collinear antenna," QST, vol. 47, no. 8 pp. 30-3.

[4-19] D. P. Shafer, "Four-band dipole with traps," QST, vol. 42, no.10, pp. 38-40.

[4-20] C. J. Lin, D. P. Nyquist, and K. M. Chen, "Short Cylindrical antennas with enhanced radiation of high directivity," IEEE Trans. Antennas Propagat. (Commun.), vol. AP-18, pp. 576-580, July 1970.

[4-21] Y. P. Liu and D. L. Sengupta, "Resistively loaded linear antenna: current distribution and far field." Univ. of Michigan Radiation Laboratory Memo 004940-507-M.

[4-22] E. Altshuler, "The traveling-wave linear antenna," IRE Trans.AntennasPropagat., vol. AP-9, pp. 324-329, July 1961.

[4-23] R. W. P. King, The Theory of Linear Antenflus. Cambridge,Mass. : Harvard University Press, 1956.

[4-24] E. E. Altshuler, "The traveling wave linear antenna," IRE Trans. Antennas and Propagation, vol. AP-9, pp. 324-329, July 1961.

[4-25] T. T. Wu and R. W. P. King, "The cylindrical antenna with non-reflecting resistive loading," IEEE Trans. Antennas and Propagation, vol. AP-13, pp. 369-373, May 1965.

General Conclusion

This manuscript that is between your hands, dear reader, contains four chapters that describe the results of the work during three years. This thesis presents an efficient approach to the understanding of Metamaterials structures and their applications. In the frame of this work, a set of simulations and investigations are accomplished, that allows one to predict the functionality of inclusions and resonators made up of Metamaterials.

The basic history and concepts of Metamaterials studies are paragraphed in first chapter to ensure a beneficial prefatory to the following chapters of the manuscript. Starting from the primary attempt to discover the concept of artificial materials in the 19th century up to the great evolution in the field of Metamaterials nowadays, a historical view is introduced.

The concepts of MTMs continue by demonstrating chirality and bianisotropic media. The Lindman's experiments with artificial isotropic chiral medium, made from randomly dispersed electrically small helices in a host were extensively repeated by many research groups leading to several patents granted. The growth of research on photonic crystals, as a new class of artificially structure materials in parallel to the chiral structures, is then presented in addition to composite medium based on periodic array of interspaced SRRs and wires.

Concerning researches in Metamaterials domain, the remarkable properties of MTMs that are not found in other naturals materials are provided. In other words, MTMs are characterized by double negative DNG (negative permittivity and permeability) property that allows the propagation of EM with $\vec{E}$, $\vec{H}$ and $\vec{K}$ building a left-handed triad. Moreover, the phase in a DNG medium propagates backward to the source with the phase velocity opposite to the group velocity.

In the second chapter of this manuscript, we presented classical Maxwell's equations that give two vector equations relating the field vectors of an EM wave by means of four dyadic parameters. All physical phenomena within the medium are hidden behind these four dyadic where the most general linear medium can be described in terms of these parameters. This general medium is also called magnetoelectric or bianisotropic.

Anisotropic, bi-isotropic, chiral and non-reciprocal materials are examples of bi-anisotropic media. On the other hand, embedding metallic resonant particles showing cross

polarization effects in a host dielectric medium is the usual technology for obtaining bi-isotropic and/or bianisotropic artificial media.

The bianisotropic effect for MTMs is then tested to extract the effective material parameters. The test is performed on a split ring resonator (SRR) of two different topologies; the broadside-coupled BC-SRR and the edge-coupled EC-SRR. The theoretical analyses show that depending on the orientation of the EC-SRR to the external EM fields, the structure can exhibit either a bianisotropic or non-bianisotropic behavior. On the other hand, the BC-SRR structure exhibits a non-bianisotropic effect due to the symmetry of the structure. This is an important result and will lead to a conclusion that the symmetrical structure has a lack of magneto-electric coupling.

Another presented method is the extraction of the constitutive parameters of Metamaterial from transmission and reflection characteristics. A Matlab code for the retrieval procedure is written and the constitutive parameters are extracted one by one. The physical behavior of extracted effective permittivity or permeability by S-retrieval method was achieved where it is concluded that such parameters cannot form the effective description of a homogenized material.

Bloch analysis and the Brillouin zone for a primitive cell based on the solid physics background are then discussed. The Metamaterial lattice analyzed as a photonic crystal is formed by the double negative SRR-Wire based unit cells. The results of both approaches show a good agreement between the solution of the periodic boundary eigenvalue problem and the retrieval S-parameters extracted from scattering parameters. For a single wire unit cell, The solution of a periodic boundary eigenvalue problem presents a valuable tool that allows one to identify frequency ranges of forward and backward waves in a lattice, corresponding to double positive and double negative constitutive parameters, respectively.

In the third chapter, performance improvement of a dipole antenna placed on AMC surface is demonstrated. Using Metamaterial structures, the gain and the directivity of such antenna have been widely improved. All the obtained results have proved that the MSRR cells can perfectly replace the conventional ground plane in order to improve the radiation characteristics. Moreover, the impact of the MSRR cells number on the antenna performance has also been investigated.

In the last chapter of this manuscript, the functioning of radiating antennas having several phases and conditions are presented. As an introductory to the chapter, the characteristics of

radiating elements as antenna engineering point of view are demonstrated. Then, in the second paragraph, dipole antennas and their functions are explained as an entrance to discuss the metamaterial loaded dipole antennas. The approach is based on loading the antennas with a small number of Metamaterial particles to achieve devices with enhanced performance for practical purposes.

The trap-loaded antenna is the first form presented in the following paragraph. Its general design is explained beside the demonstration of the current distribution by employing the integral equation technique resulting in a type that supports an essentially standing wave distribution of currents. Then, in order to compare the results with basic antenna structure, a simple rectangular dipole antenna is designed and simulated to have a radiating frequency at 1.5 GHz. The reflection coefficient, the input impedance and the radiation pattern are shown and validate the radiation at the target frequency.

The following step focused on creating another radiation frequency by loading the antenna by two lumped RLC traps; one trap on each arm of the dipole antenna. The results are again proved when two frequencies at 1.5 and 2.4 GHz are created. The validation of this result is introduced in the next paragraph when a dipole antenna is loaded with two SRRs on each arm. This configuration of dual-frequency performance is approved since two frequencies are created at 1.5 and 2.4 GHz. The first one is due to the dipole itself, while the second is originated in the vicinity of the SRR self-resonant frequency.

The inclusion that replaced the SRR is the Multi Split Ring Resonator (MSRR). Two operating frequencies are obtained at 1.5 and 2.4 GHz giving rise to a dual-band structure similar to that obtained when loading the antenna with four SRRs.

As a perspective in the conclusion of this chapter, the realization of the MSRR-loaded dipole antenna could be accomplished to perform the measurements needed in order to validate the theoretical results experimentally.

Appendices

A. Mathcad file: Drude Model

Thin wire effective permittivity

v c is related to wp and it is dependent on the material type and it is also very small :
in aluminium wp= 15e.V and vc= 0.1e.V

n:is the number of electrons in Aluminium

$$\omega_p := \sqrt{\frac{2\cdot\pi\cdot c_o^{\,2}}{a^2\cdot\ln\left(\frac{a}{r}\right)}}$$

$a := 5\cdot10^{-3}$ $\mu_o := 4\cdot\pi\cdot10^{-7}$ $\varepsilon_o := 8.85\cdot10^{-12}$ $n := 5.675\cdot10^{17}$ $\sigma := 3.65\cdot10^{7}$

$r := 1\cdot10^{-6}$ $c_o := 3\cdot10^{8}$ $e := 1.6021765310^{-19}$

$$m_{eff} := \frac{\mu_o\cdot e^2\cdot n}{2\cdot\pi}\cdot\ln\left(\frac{a}{r}\right) \qquad m_{eff} = 2.4815\times10^{-26} \qquad \nu_c := 0.01\cdot\omega_p$$

$$n_{eff} := \frac{n\cdot\pi\cdot r^2}{a^2} \qquad n_{eff} = 7.131\times10^{10}$$

$$\omega_p = 5.153\times10^{10}$$

$$\kappa := \frac{\varepsilon_o\cdot a^2\cdot\omega_p^{\,2}}{\pi\cdot r^2\cdot\nu_c}$$

$$f_p := \frac{\omega_p}{2\cdot\pi} \qquad f_p = 8.202\times10^{9} \qquad \kappa = 3.629\times10^{8}$$

$$\nu_c = 5.153\times10^{8}$$

$$\varepsilon_{eff}(f) := 1 - \frac{\omega_p^{\,2}}{2\cdot\pi\cdot f\cdot\left(2\cdot\pi\cdot f - \nu_c\cdot j\right)}$$

In the case of a resistive wire

$$\varepsilon_{eff\_res}(f) := 1 - \frac{\omega_p^{\,2}}{2\cdot\pi\cdot f\cdot\left(2\cdot\pi\cdot f - \frac{\varepsilon_o\cdot a^2}{\pi\cdot r^2\cdot\sigma}\cdot j\right)}$$

$$y(f) := 0$$

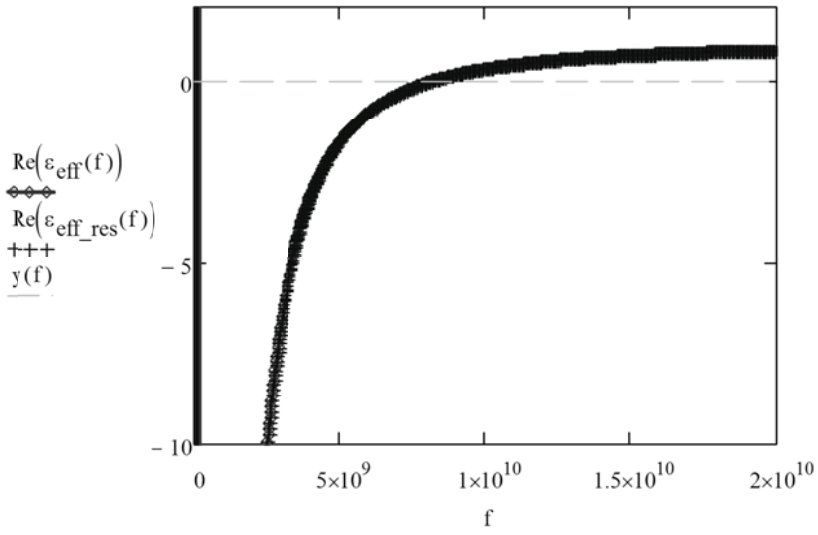

B. Mathcad file: Lorentz Model

$r := 2\cdot$ $\quad a := 1\cdot 1$ $\quad d := 1\cdot 10^{-4}$ $\quad c_o := 3\cdot 10^{8}$ $\quad \sigma := 200$ $\quad \mu_o := 4\cdot\pi\cdot 10^{-7}$

$$\omega_{mp} := \left[\frac{3\cdot d\cdot c_o^{\,2}}{\pi^2\cdot r^3\cdot\left(1-\frac{\pi\cdot r^2}{a^2}\right)}\right]^{\frac{1}{2}} \qquad \omega_{mp} = 1.978\times 10^{10} \qquad f_{mp} := \frac{\omega_{mp}}{2\cdot\pi}$$

$$f_{mp} = 3.148\times 10^{9}$$

$$\omega_o := \left(\frac{3\cdot d\cdot c_o^{\,2}}{\pi^2\cdot r^3}\right) \qquad f_o := \frac{\omega_o}{2\cdot\pi} \qquad f_o = 2.943\times 10^{9}$$

For Cylindrical wire:

$$\mu_{eff}(f) := 1 - \frac{\frac{\pi r^2}{a^2}}{1+\frac{2\cdot\sigma\cdot j}{2\cdot\pi\cdot f\cdot r\cdot\mu_o}-\frac{3\cdot d\cdot c_o^{\,2}}{\pi^2\cdot(2\cdot\pi\cdot f)^2\cdot r}} \qquad y_o(f) := 0 \qquad y_1(f) := 1$$

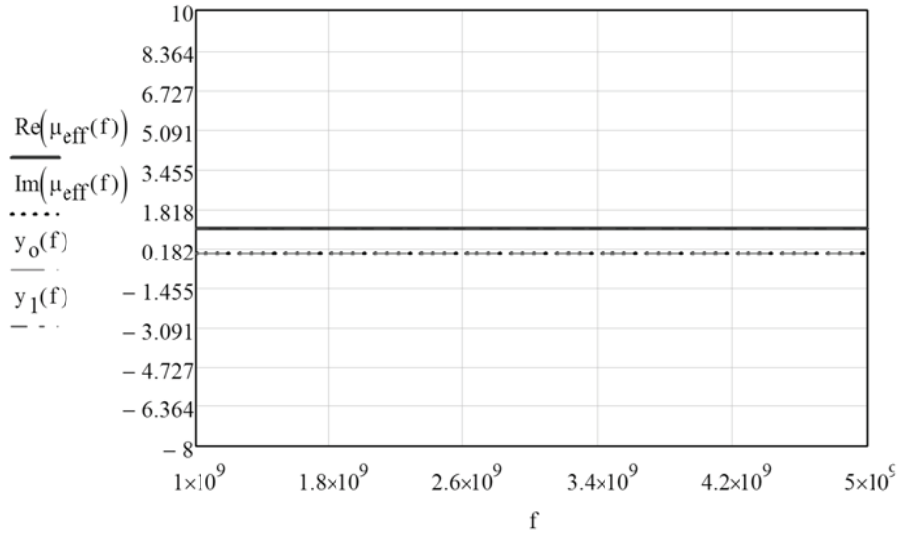

$c := 1 \cdot 10^{-3}$ $l := 2 \cdot 10^{-3}$

For Split Ring resonator:

$$\mu_{eff\_SRR}(f) := 1 - \frac{\frac{\pi r^2}{a^2}}{1 + \frac{2 \cdot l \cdot \sigma \cdot j}{(2 \cdot \pi \cdot f) \cdot r \cdot \mu_o} - \frac{3 \cdot l \cdot c_o^{\,2}}{\pi \cdot (2 \cdot \pi \cdot f)^2 \cdot \ln\left(\frac{2 \cdot c}{d}\right) \cdot r^3}}$$

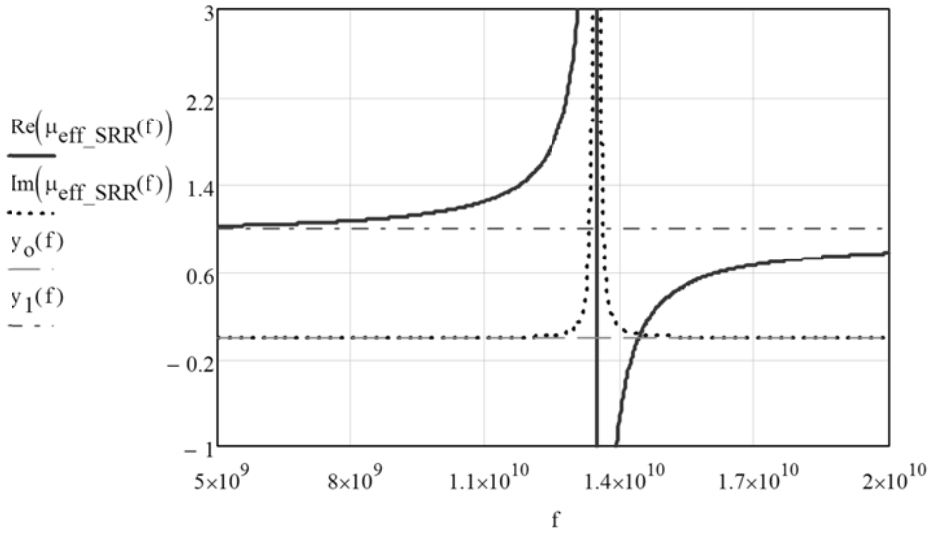

Rem Exponential Scale

$f_{plotstart} := 0.5 \cdot 10^9$ $\quad plotpoints := 55$

$f_{plotstop} := 20 \cdot 10^9$

$ppts := 0, 1 .. plotpoints$

$f_{base} := \frac{f_{plotstop} - f_{plotstart}}{plotpoints}$

$f_{base} = 3.545 \times 10^8$

$pltfreqs_{ppts} := f_{plotstart} \cdot 10^{\left(\frac{ppts}{plotpoints} \cdot \log\left(\frac{f_{plotstop}}{f_{plotstart}}\right)\right)}$

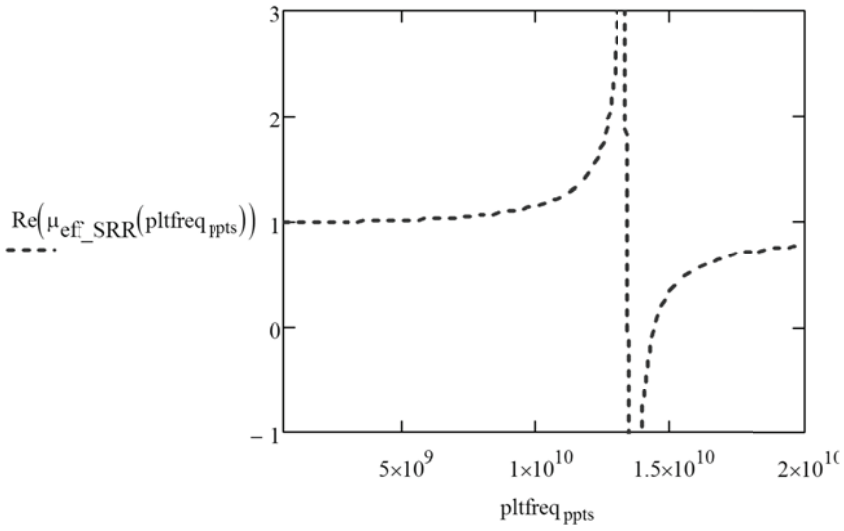

$mu_{ppts} := \mu_{eff\_SRR}(pltfreq_{ppts})$

$m_{ppts,0} := pltfreq_{ppts}$

$m_{ppts,1} := Re(mu_{ppts})$

C. ABCD Retrieval Method

Retrieval Procedure
ABCD Matrix Based

$len := length\left(Z^{\langle 0 \rangle}\right)$ $\quad d := 10 \cdot 10^{-3}$ $\quad Z_o := \left(Z^{\langle 13 \rangle}\right)_3$

$Z_o = 376.73$

$n := 2 .. len - 1$

$ReZ11 := Z^{\langle 1 \rangle}$ $\quad ImZ11 := Z^{\langle 2 \rangle}$ $\quad ReZ12 := Z^{\langle 3 \rangle}$ $\quad ImZ12 := Z^{\langle 4 \rangle}$ $\quad f := Z^{\langle 0 \rangle}$

$ReeZ11_{n-2,0} := ReZ11_{n,0}$

$ImmZ11_{n-2,0} := ImZ11_{n,0}$

$ReeZ12_{n-2,0} := ReZ12_{n,0}$ $\quad total := len - 3$ $\quad total = 200$

$ImmZ12_{n-2,0} := ImZ12_{n,0}$

$freq_{n-2,0} := f_{n,0}$ $\quad length(freq) = 201$

$k_o := \frac{2 \cdot \pi \cdot freq}{3 \cdot 10^8}$ $\quad length\left(k_o\right) = 201$

$Z11 := ReeZ11 + i ImmZ11$

$Z12 := ReeZ12 + i ImmZ12$ $\quad length(ReeZ12) = 201$

$A := \frac{Z11}{Z12}$ $\quad B := \frac{\overrightarrow{(Z11 \cdot Z11)} - Z12^2}{Z12}$ $\quad C := \frac{1}{Z12}$ $\quad D := \frac{Z11}{Z12}$

$$\gamma := \frac{acos\left(\frac{Z11 + Z11}{2 \cdot Z12}\right)}{d}$$

$$Z_{bloch} := \frac{B}{e^{(i \cdot \gamma \cdot d)} - A}$$

$$\mu_{eff} := \frac{\overrightarrow{(\gamma \cdot Z_{bloch})}}{\overrightarrow{(Z_o \cdot k_o)}}$$ $\quad length\left(\mu_{eff}\right) = 201$

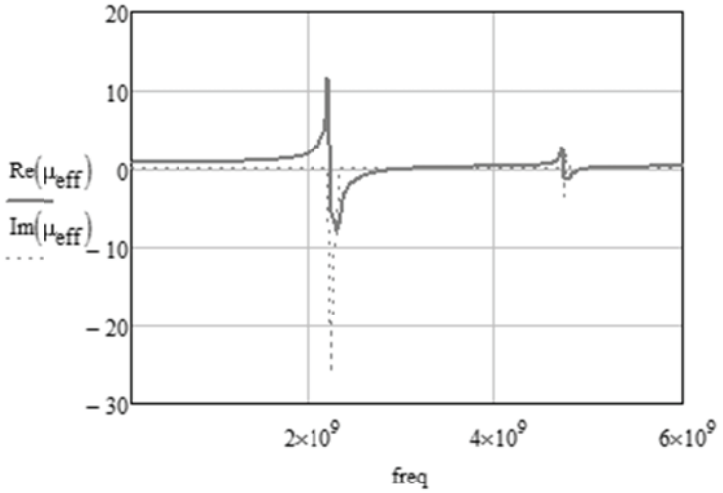
20
10
0
− 10
− 20
− 30
Re(μeff)
Im(μeff)
2×10^9
4×10^9
6×10^9
freq

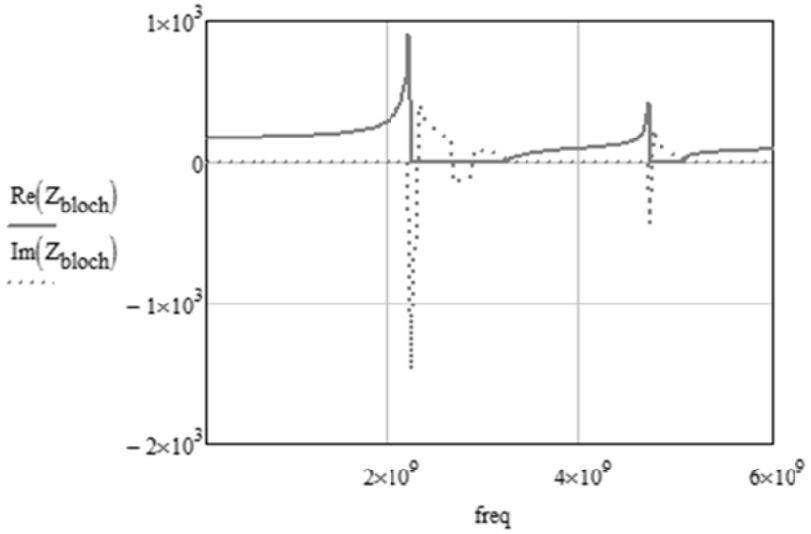
1×10^3
0
− 1×10^3
− 2×10^3
Re(Zbloch)
Im(Zbloch)
2×10^9
4×10^9
6×10^9
freq

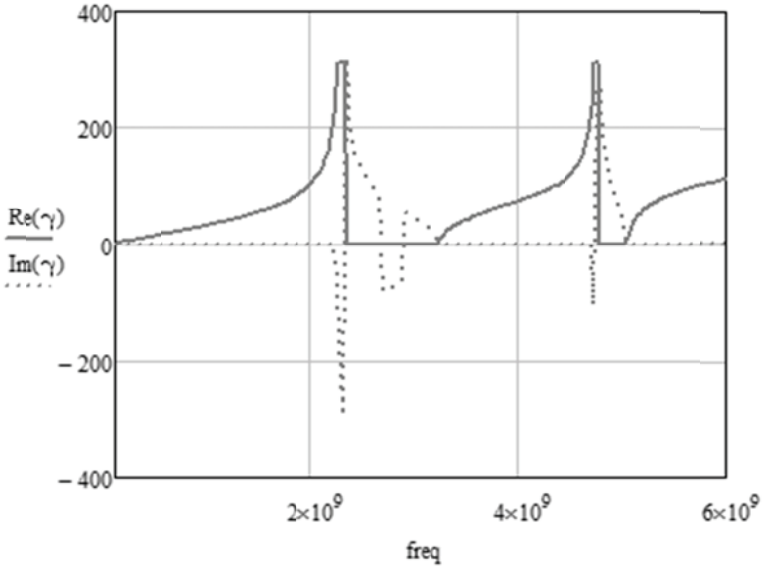
400
200
0
− 200
− 400
Re(γ)
Im(γ)
2×10^9
4×10^9
6×10^9
freq

D. SAHA SRR Analytical Resonance Model

$r_{ext} := 5 \cdot 10^{-3}$ $\varepsilon_o := 8.85 \cdot 10^{-12}$ $f_o := 2.4$

$g := 0.5 \cdot 10^{-3}$ $\mu_o := 4 \cdot \pi \cdot 10^{-7}$

$c_o := 3 \cdot 10^{8}$ $d := 0.5 \cdot 10^{-3}$

$t := 35 \cdot 10^{-6}$ $c := 0.5 \cdot 10^{-3}$ $\lambda := \frac{300}{f_o}$ $\lambda = 125$

$h := 1 \cdot 10^{-3}$ $\varepsilon_r := 4.4$ $r_{ex} := \frac{\lambda}{20}$ $r_{ex} = 6.25$

$a := \frac{d}{2}$ $b := \frac{d}{2} + c$

$r_{avg} := r_{ext} - c - \frac{d}{2}$ $r_{avg} = 4.25 \times 10^{-3}$

$$K(m) := \int_0^{\frac{\pi}{2}} \frac{1}{\sqrt{1 - m^2 \cdot (\sin(\theta))^2}} d\theta$$

$$F(m) := \begin{cases} \left[\frac{1}{\pi} \cdot \left(\ln\left(2 \cdot \frac{1 + \sqrt{1 - m^2}}{1 - \sqrt{1 - m^2}}\right)\right)\right]^{-1} & \text{if } m \le 0.7 \\ \left[\frac{1}{\pi} \cdot \left(\ln\left(2 \cdot \frac{1 + \sqrt{m}}{1 - \sqrt{m}}\right)\right)\right]^{1} & \text{if } m > 0.7 \end{cases}$$

$k := \frac{\frac{d}{2}}{\frac{d}{2} + c}$ $k = 0.333$ $K(k) = 1.617$

$k_{prime} := \sqrt{1 - k^2}$ $k_{prime} = 0.943$ $K(k_{prime}) = 2.529$

$k_1 := \frac{\sinh\left(\pi \frac{a}{2 \cdot h}\right)}{\sinh\left(\pi \frac{b}{2 \cdot h}\right)}$ $k_1 = 0.274$ $K(k_1) = 1.602$

$k_{1prime} := \sqrt{1 - k_1^2}$ $\quad k_{1prime} = 0.962$ $\quad K(k_{1prime}) = 2.714$

$\varepsilon_e := 1 + \frac{\varepsilon_r - 1}{2} \cdot \frac{K(k_{prime})}{K(k)} \cdot \frac{K(k_1)}{K(k_{1prime})}$ $\quad \varepsilon_e = 2.569$

$Z_o := \frac{120 \cdot \pi}{\sqrt{\varepsilon_e}} \cdot \frac{K(k)}{K(k_{prime})}$ $\quad Z_o = 150.456$

$C_{pul} := \frac{\sqrt{\varepsilon_e}}{c_o \cdot Z_o}$ $\quad C_{pul} = 3.551 \times 10^{-11}$

$C_0 := (\pi r_{avg} - g) \cdot C_{pul}$ $\quad C_0 = 4.563 \times 10^{-13}$

$C_g := \varepsilon_o \cdot \frac{c \cdot t}{g}$ $\quad C_g = 0$

$C_{eq} := \frac{(C_0 + C_g)}{2}$ $\quad C_{eq} = 2.283 \times 10^{-13}$

$l := 2 \cdot \pi \cdot r_{ext} - g$ $\quad l = 0.031$

$\gamma := 2.451$

$L_T := 0.0002 \cdot l \cdot \left(2.303 \cdot \log\left(\frac{4 \cdot l}{c}\right) - \gamma\right) \cdot 10^{-3}$ $\quad L_T = 1.892 \times 10^{-8}$

$f_o := \frac{1}{2 \cdot \pi \cdot \sqrt{L_T \cdot C_{eq}}}$ $\quad f_o = 2.421 \times 10^{9}$

Résumé

Le travail de cette thèse est en rapport avec les métamatériaux et ses applications. Tout d'abord, un état de l'art est dressé en présentant leur évolution depuis leur apparition en 19ème siècle jusqu'au nos jours. Les notions sur les milieux chirale, bi-anisotrope, cristaux photoniques et quelques applications dans ces milieux sont données.

Ensuite, nous présentons les équations classiques de Maxwell dans les milieux complexes. L'effet bi-anisotrope dans les métamatériaux est ensuite validé par l'extraction des paramètres caractéristiques du matériau main gauche (LHM). La validation a été faite en utilisant deux types différents du résonateur avec inclusion (SRR). Les métamatériaux sont également étudiés comme des cristaux photoniques quand les dimensions utilisées sont de l'ordre de la longueur d'onde correspondant.

De plus, les résonateurs SRR et multi-SRR sont analysés du point de vue analytique et électromagnétique afin d'extraire leur fréquence de résonance. Par conséquent, ces composants peuvent être introduits dans différents types de conception; La surface conductrice magnétique artificielle (AMC) illustre un cas explicite et efficace de ces derniers.

Une antenne dipôle, placée sur cette surface à la place d'un plan de masse conventionnel, a été étudiée comme une application des métamatériaux. Les résultats relatifs sur la directivité, le gain et le coefficient de réflexion montrent une nette amélioration. Une antenne multi-bandes, comme une autre application des métamatériaux, a également été conçue et simulée. Le résonateur SRR est inséré dans l'antenne de départ afin de créer une autre résonance, et par conséquent une autre bande est ainsi créée.

Mots clés: *Métamatériaux, Matériau main gauche, Matériaux doublement négatifs, Résonateur à inclusion, Multi-Résonateurs à inclusion, Conducteur magnétique artificiel, Antenne Dipôle, Antenne multi-bandes.*

Abstract

The work in this thesis deals with metamaterials, its components and applications. A historical overview about these materials, features and researches in the domain are presented. Chiral media, binaisotropic materials and photonic crystals are also studied in order to visualize physics behind metamaterials.

Electromagnetic properties in complex media are widely investigated. Starting from Maxwell's equations, bi-anisotropic materials and their effect are deeply analyzed whereas two types of Split Ring Resonator (SRR) are treated to determine constitutive parameters of Left Handed Materials (LHM). The metamaterials are also studied as photonic crystals since the effective medium approach is not applicable when the dimensions of the inclusions tend to the operating wavelength.

Moreover, SRRs and Multi SRRs are synthesized analytically and electromagnetically in order to extract their resonant frequencies. Consequently, these components could be introduced in any design; Artificial Magnetic Conductor (AMC) surface is an efficient case. Thus, a low profile antenna positioned over such surface is examined as an application of metamaterials. The results of directivity, gain and reflection coefficient are of great importance and affirm the employing of metamaterials in such applications.

A dual band PCB antenna, as another application of metamaterials, is designed and simulated. The SRR element studied in the previous chapters is used as the trap which inserted in the arm of the antenna in order to create another resonance, and consequently another band is created.

Keywords: *Metamaterials (MTMs), Left Handed Materials (LHM), Double Negative Materials (DNG), Inclusions, Split Ring Resonators (SRRs), Multi Split Ring Resonators (MSRRs), Artificial Magnetic Conductors (AMCs), Dipole antenna, Dual band antenna.*